Magnetic field extrapolation in the solar corona and observations of a flux rope in the solar wind

Dissertation
zur Erlangung des Doktorgrades
der Mathematisch-Naturwissenschaftlichen Fakultäten
der Georg-August-Universität zu Göttingen

vorgelegt von
Peng Ruan
aus Anqing, Anhui, China

Göttingen 2009

Contents

Summary

Since the magnetic field controls most dynamic phenomena in the solar corona, it is important to obtain information about the coronal magnetic field. Because direct measurements of the solar coronal magnetic field and plasma are extremely difficult and inaccurate, we use a modeling approach based on observational quantities, e.g. the measured photospheric magnetic field, to reconstruct the solar coronal magnetic field and plasma in a self-consistent model. We take an analytic magnetohydrostatic model to extrapolate the magnetic field in the corona from photospheric magnetic field measurement. The boundary conditions are given by a synoptic magnetogram on the inner boundary and by a source surface on the outer boundary. In the model, the electric current density can be decomposed into two components: one component is aligned with the magnetic field lines, whereas the other component flows in spherical shells. The second component of the current produces finite Lorentz forces which are balanced by the pressure gradient and the gravity force. We compare the magnetic field distribution of our model with potential and force-free field models for the same boundary conditions and find that the extrapolation result of our model differs noticeably from the result of two others. The density on the source surface in our model is higher in the equatorial plane than in the polar region, which is a reasonable result from the real situation. To summarize, the distribution of not only the magnetic field but also the plasma in the solar corona can be constructed from this MHS model self-consistently.

Occasionally, the solar corona becomes unstable and ejects magnetic fields and plasma, e.g. the coronal mass ejections (CMEs), into the interplanetary space. If directed towards the Earth, these interplanetary coronal mass ejections (ICMEs) can disturb the Earth magnetosphere intensely. A similar type of magnetic structure to the ICMEs is small-scale magnetic flux ropes. Though the flux ropes in the magnetosphere have been widely studied, further observations about the flux ropes in the solar wind are still needed to clarify the basic characteristics, such as the length, the diameter, and the possible generation mechanism. The study of the flux ropes in the solar wind can help us not only to differ the ropes from ICMEs but also to understand the characteristics of the multiple-X-line magnetic reconnection, which is the most probable generation mechanism for the ropes. The multiple-spacecraft observations are particularly demanded to study the space variation of the flux rope in the solar wind. On 15 January 2007, an extended magnetic structure was observed consecutively by five spacecraft (ACE, WIND, STEREO A and B, and CLUSTER) in the solar wind. The similar bipolar magnetic field variations from five spacecraft suggest a two-dimensional magnetic structure. The abrupt disappearance of the beam electrons in the structure core suggests the magnetic isolation of the structure core from the surrounding environment. The analysis shows that this magnetic structure is a magnetic flux rope, which extends over at least 180 R_E in space. The length and ori-

entation of the flux rope was determined by a local Minimum Variance Analysis (MVA) from individual spacecraft observations of the magnetic field and a timing analysis based on the joint observations by all five spacecraft. The result shows that the orientation of the flux rope stays constant in space and time. The flux rope is embedded in a Corotating Interaction Region (CIR), which followed a magnetic cloud. The small scale and the possible reconnection signatures inside the flux rope suggested that the flux rope should be generated locally by magnetic reconnection in the solar wind instead of being generated in the solar corona.

1 Introduction

1.1 Solar corona

The solar corona is a very hot, tenuous part of the solar atmosphere appearing in white light as streamers, plumes and other structures extending out from the solar disk. Early observations of the solar corona date back to ancient eclipse observations, which can be found in ancient Chinese, Indian, and Babylonian sources [*Aschwanden,* 2005]. Nowadays, scientists observe the Sun with ground-based telescopes and spacecraft. The Mauna Loa Solar Observatory (MLSO), located on the island of Hawaii, provides daily white light coronagraph images. The Wilcox Solar Observatory, located in the foothills west of the Stanford University campus, began daily observations of the Sun's global magnetic field in the photosphere in May 1975. The Solar and Heliospheric Observatory (SoHO) is a solar-dedicated space mission, which was launched in December 1995. The Solar TErrestrial RElations Observatory (STEREO), composed of two spacecraft, is another important mission for observing the Sun, which was launched in October 2006. Figure 1.1 shows an ground-based observation of the corona taken during the eclipse on 11 July 1991. Helmet streamers, large cap-like coronal structures with long pointed peaks into the heliospheric space, are formed by a network of magnetic loops above the solar surface. Polar plumes, associated with the open magnetic field lines at the Sun's surface, are long thin streamers that project outward from the Sun's north and south poles at solar minimum activity. Both of these two structures can be found in this picture.

Our understanding of the Sun has significantly improved in the last fifty years. Figure 1.2 summarizes the change of our understanding of the structure of the solar atmosphere during the last decades [*Schrijver,* 2001]. Around 1950s, it was thought that the photosphere, chromosphere and corona might consist of stratified layers, in the presence of gravitation (the left panel). *Edlén* [1943] found FeIX and CaXIV lines in the solar corona, which indicated a much higher temperature (above 1 MK) in the corona than in the photosphere. Though scientists did not understand the exact heating mechanism to generate such a high temperature, intermittent heating ε may exist in the corona based on people's understanding during that time period. During 1980s, the concept of flux tubes of the magnetic field was introduced. These flux tubes could cluster from the photosphere into the corona (the middle panel) [*Gabriel,* 1976]. The tubes can serve as channels for the plasma to transport energy and mass from the solar interior, where the plasma $\beta > 1$, to the solar atmosphere, where the plasma $\beta < 1$. The shock waves from the Sun's interior might dissipate in the solar surface and be a possible source to heat the chromosphere [*Hollweg,* 1985]. After 2000, with observations from SoHO and Skylab, people realized that the solar corona is a very dynamic and inhomogeneous region. The photosphere,
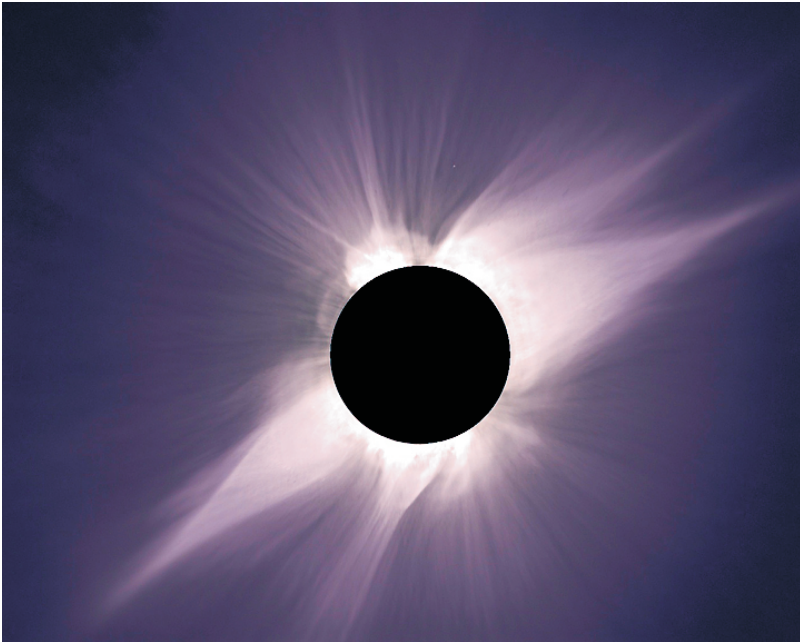
Figure 1.1: Coronal observation during the solar eclipse on 11 July 1991.

chromosphere and corona are coupled by many dynamic processes, such as upward and downward flows ρ, intermittent heating (ϵ_i), field line motions and magnetic reconnection, emission and absorption in the plasma, acoustic waves and shock waves (the right panel) [*Aschwanden,* 2005]. From Figure 1.2, we can see that our understanding of the solar atmosphere evolved from simple spherical geometry towards dynamic and inhomogeneous topology.

1.1.1 Temperature and density

The solar surface and the corona above are often divided into three parts: coronal holes, quiet-Sun regions, and active regions, which show different properties of the magnetic field and plasma. Though the temperature is very high everywhere in the corona, it differs noticeably between these three regions. Since magnetic field lines in the coronal holes are open and plasma transport along field lines is very efficient, the heated plasma can easily escape to heliospheric space. The temperature in coronal holes is around 1 MK, which is the coolest part in the corona. Most magnetic field lines in quiet-Sun regions and active regions are closed. The heated plasma in these regions is trapped in magnetic loops, and the temperature in these two regions is higher than that in the coronal holes. The temperature in the quiet-Sun regions varies from 1 MK to 2 MK. The active regions
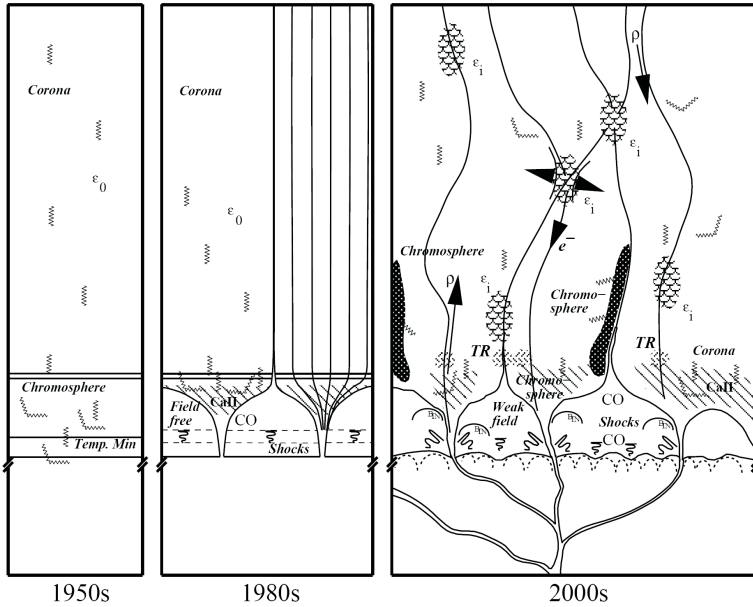
Figure 1.2: Cartoon showing the evolution of the geometric concepts of the solar corona [*Schrijver et al.,* 2001].

have the highest temperature, usually above 2 MK. The difference of the temperature in the quiet-Sun regions and the active regions is due to different heating rates and energy loss rates [*Aschwanden,* 2005]. The correlation between higher magnetic field and a more efficient heating in the corona suggests that the magnetic field may play some role in the heating mechanism.

The temperature distribution in Figure 1.3 shows an average 1D model for a gravitationally stratified solar atmosphere [*Gabriel,* 1976; *Fontenla et al.*, 1990; *Aschwanden,* 2005]. The temperature in the chromosphere is around several thousand Kelvin, but rises rapidly to above 1 Million Kelvin in the corona. If only thermal conduction and radiative cooling are at work, the temperature in the corona should drop off steadily with increasing distance from the chromosphere according to the second law of the thermodynamics. So the question of how the corona is heated is a fundamental issue in solar physics, and is still a matter of debate. Though a certain conclusion is not reached yet, possible mechanisms were proposed to explain corona heating. Nowadays it is a custom to classify these mechanisms into two types of models: DC (Direct Current) models and AC (Alternating Current) models. In DC models, if the time scale of the fluctuation of magnetic field line foot-points is much longer than the local Alfvén transit time, the loops can adjust to the changing boundary condition in a quasi-static way. So the energy from the dissipation of the currents can heat the corona directly. In this model, the currents can be dissipated
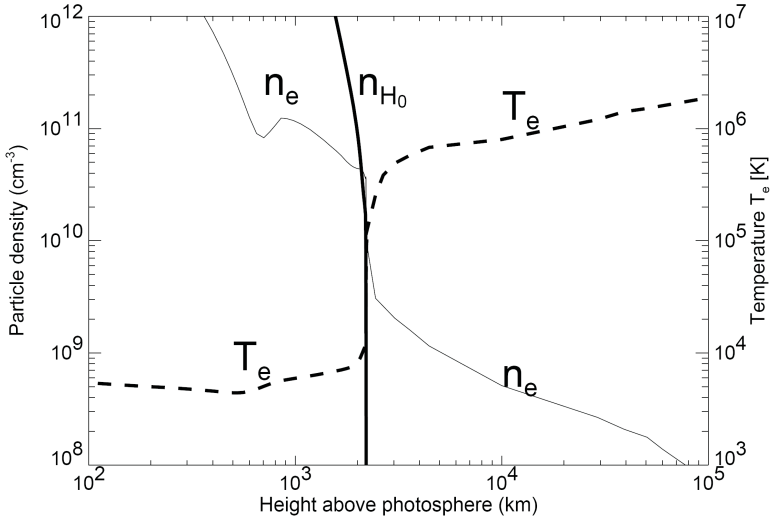
Figure 1.3: Electron density and temperature in the chromosphere and lower corona [*Gabriel,* 1976].

by Ohmic dissipation, magnetic reconnection [*Sturrock and Uchida,* 1981; *Paker,* 1983, 1988; *Berger,* 1991, 1993; *Galsgaard and Nordlund,* 1997;], current cascading [*Van Ballegooijen,* 1986; *Galsgaard and Nordlund,* 1996, 2002], or viscous turbulence [*Heyvaerts and Priest,* 1992; *Aly and Amari,* 1997; *Milano et al.,* 1997, 1999]. In AC models, the time scale during which loops adjust is much shorter than that of the photospheric driver, so the corona will be heated by the damping and dissipation of incident waves. In this case, the currents can be dissipated by Alfvénic resonance [*Hollweg,* 1985, 1991], resonance absorption [*Ionson,* 1978; *Goossens et al.,* 1992, 1995; *Ruderman et al.,* 1997], phase mixing [*Heyvaerts and Priest,* 1983; *De Moortel et al.,* 1999, 2000], acoustic waves [*Kuperus et al.,* 1981] and shocks [*Hollweg,* 1985]. The details of these models and other important papers corresponding to the models are summarized in [*Aschwanden,* 2005].

From Figure 1.3, we can see that the electron density decreases by several orders of magnitudes from the chromosphere to the corona. Although the plasma density in the corona is very low and keeps decreasing with height above the solar surface, it differs noticeably between coronal holes, quiet-Sun regions and active regions. In the coronal holes in the lower corona, since the magnetic field lines are open and the plasma can easily escape into the heliospheric space along the field lines, the electron density is comparatively low, usually below 10^8 cm^{-3}. In quiet-Sun regions and active regions, where the plasma is trapped on the closed lines, the density is higher than in the coronal holes. In active regions, many dynamic processes can heat up the chromospheric plasma and drive them into the corona, generating over-dense structures with densities higher than in the ambient quiet-Sun regions [*Aschwanden,* 2005]. The density is around 10^8 cm^{-3} in quiet-Sun

regions in the lower corona, and is between 10^8 cm^{-3} to 10^9 cm^{-3} in active regions.

The best opportunity for ground-based telescopes to observe the white light corona is during the solar eclipse. The largest component (over 90%) of the total integrated coronal brightness comes from the K-corona. K-corona emission is continuum, resulting from Thomson scattering of photospheric radiation from coronal electrons [*Michael and Edenhofer,* 1990]. The K-corona typically dominates the corona emission out to about two solar radii, and is overtaken at larger solar distances by the F-corona. The F-corona emission contains the Fraunhofer lines and is attributed to scattering from interplanetary dust [*Michael and Edenhofer,* 1990]. The electron density profiles above the solar surface can be approximated by a power law function known as the *Baumbach-Allen formula* [*Aschwanden,* 2005],

$$n_e(R) = 10^8 \times [2.99(R/R_\odot)^{-16} + 1.55(R/R_\odot)^{-6} + 0.036(R/R_\odot)^{-1.5}], \qquad (1.1)$$

here $R_\odot$ is the solar radius and R is the radial distance away from the Sun center. From this equation, we can see that the electron density decreases very rapidly in the low corona, but decreases much more slowly in the outer corona.

1.1.2 Magnetic field observations

Based on the Zeeman effect, the magnetic field in the photosphere can be measured. However, the coronal magnetic field is difficult to measure so far due to the low plasma density, high plasma temperature, and small magnetic field strength. Figure 1.4 is a synoptic magnetograms from 11 May 1998 to 7 June 1998 from the MDI (Michelson Doppler Imager) instrument on board the SOHO spacecraft. The magnetic field on the solar surface is very inhomogeneous. The magnitude of the magnetic field in the coronal holes and quiet-Sun region is in the range of several tens of Gauss. The magnetic field in the active regions is usually above 100 gauss. Inside sunspots the magnetic field can reach several thousand gauss.

In the corona, the magnetic field controls most dynamic phenomena. Open-field regions exist at low activity in the two polar regions during the solar minimum, and can extend to the equator. The magnetic field lines in the open-field regions connect the Sun with the interplanetary space. As the consequence of the magnetic-field-line configuration in open-field regions, the plasma can be transported into the heliospheric space efficiently. The closed-field regions usually exist at low latitudes, and contain mostly closed field lines. These closed field lines can reach a height of about one solar radius, and open up to connect to the heliosphere eventually at higher altitudes. The plasma transport into the heliosphere in the closed-field regions is not as efficient as that in the open-field regions.

1.1.3 Plasma β and magnetic field extrapolation

A key parameter of the coronal plasma is the plasma $\beta = p_p/p_m$, which is the ratio of the particle pressure $p_p = nkT$ (n is the plasma number density, T the temperature, k the Boltzmann constant.) to the magnetic pressure $p_m = B^2/2\mu_0$ (B is the magnetic field strength, μ_0 is the magnetic permeability of vacuum.). Figure 1.5 shows the β parameter in the solar atmosphere [*Gary*, 2001]. From the figure, we can see that β is usually larger than unity in the photosphere. It decreases to less than unity in the chromosphere. In the
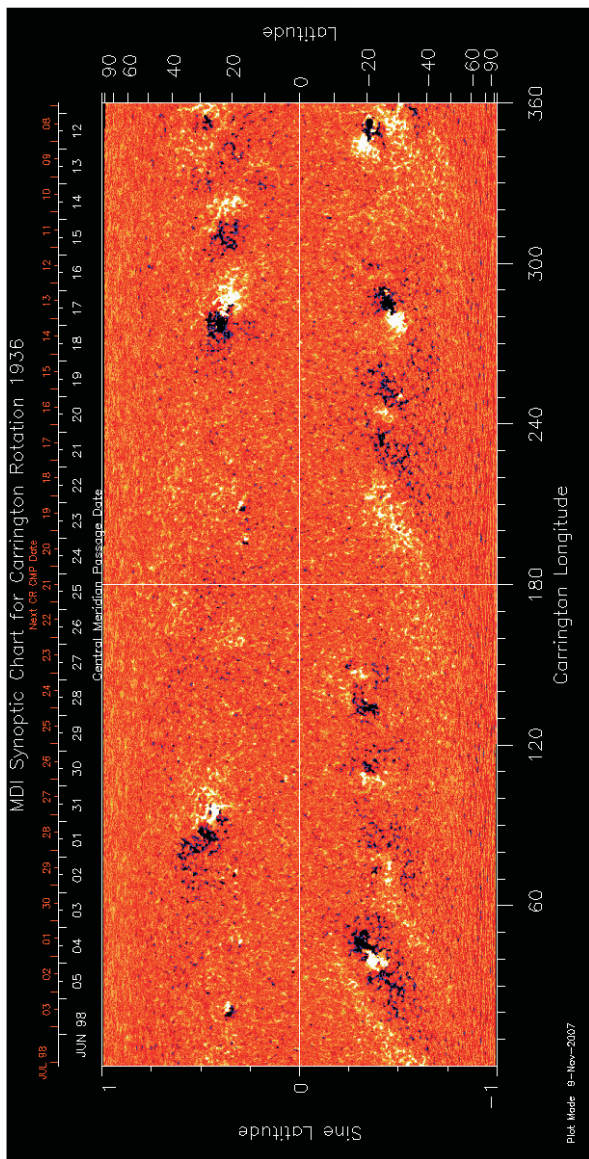
Figure 1.4: Synoptic magnetogram on the photosphere from 11 May to 07 June 1998 from the Michelson Doppler Imager (MDI) instrument onboard the Solar and Heliospheric Observatory (SoHO) spacecraft.
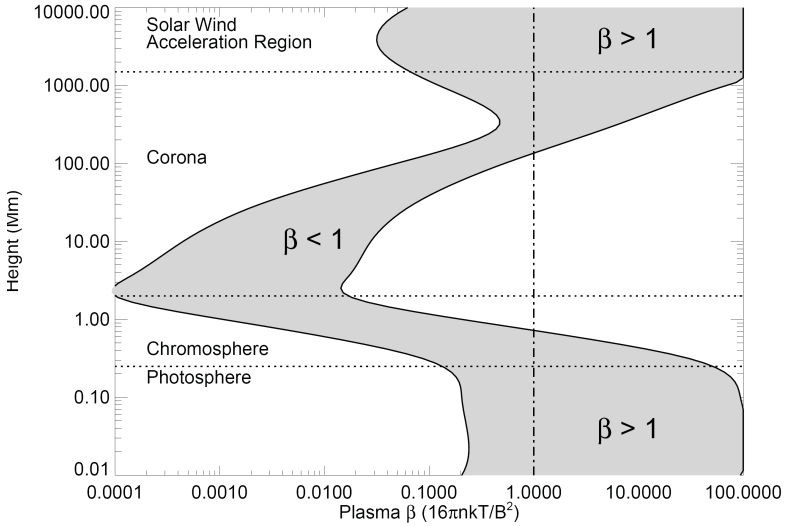
Figure 1.5: Plasma β in the solar atmosphere [*Gary*, 2001].

lower corona, the plasma β is much less than unity. So the lower corona is magnetically confined, and the particles can move only along the magnetic field lines. In the outer corona, the plasma β increases and can become larger again than unity.

When we extrapolate the magnetic field in the corona based on the photospheric magnetogram with different models, in principle we should use the magnetohydrostatic (MHS) equations. The basis of the MHS model consists of the following equations:

$$\mathbf{j} \times \mathbf{B} - \nabla p - \rho \nabla \psi = 0, \qquad (1.2)$$
$$\nabla \times \mathbf{B} = \mu_0 \mathbf{j}, \qquad (1.3)$$
$$\nabla \cdot \mathbf{B} = 0. \qquad (1.4)$$

Here, $\mathbf{j}$ and $\mathbf{B}$ are the electric current density and the magnetic field, respectively, p is the plasma pressure, ρ the plasma density, ψ the gravitational potential, and μ_0 the magnetic permeability of vacuum. (In the thesis, the bold symbols represent vectors, and non-bold symbols for scalars.) If we do a dimensional analysis and divide Eq. 1.2 by typical physical parameters in the corona, we obtain

$$\tilde{\mathbf{j}} \times \tilde{\mathbf{B}} - \tilde{\nabla} \tilde{p} \cdot \beta - \tilde{\rho} \tilde{g} \cdot \beta \cdot \frac{\rho_\circ g_\circ L_\circ}{p_\circ} = 0, \qquad (1.5)$$

where $\rho_\circ, p_\circ, g_\circ, L_\circ$ are typical plasma density, plasma pressure, gravity acceleration, gradient scale in the corona, and $\tilde{\mathbf{j}}, \tilde{\mathbf{B}}, \tilde{\nabla}\tilde{p}, \tilde{\rho}, \tilde{g}$ are dimensionless parameters of order unity. If the plasma beta is very low, like above active regions in the corona, we can ignore the

13

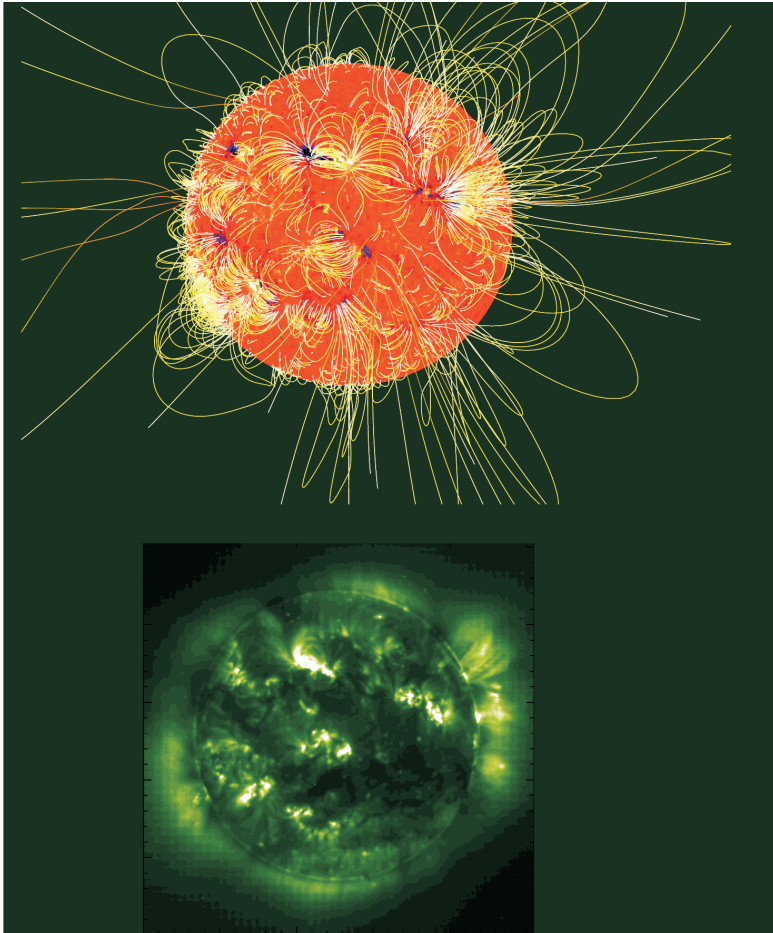Figure 1.6: MDI magnetogram with extrapolated field lines (top) and the Extreme ultra-violet Imaging Telescope (EIT) image (bottom) [*Wiegelmann* and Solanki, 2005].

second term in Eqs. 1.2 and 1.5. If we insert typical values of $\rho_\circ, p_\circ, g_\circ, L_\circ$ in an active region into Eq. 1.5, the ratio of the two length scales $\rho_\circ g_\circ L_\circ / p_\circ = L_\circ / (p_\circ / \rho_\circ g_\circ)$ will be less than 10. Since the plasma β is less than 0.01 in the active region, $\rho_\circ g_\circ L_\circ / p_\circ \cdot \beta$ will be less than 0.1. So the third term in Eqs. 1.2 and 1.5 can be also ignored. Therefore, we reach

$$\mathbf{j} \times \mathbf{B} = 0. \tag{1.6}$$

This is called force-free approximation, which is used to calculate the coronal magnetic field from the surface magnetic field in the photosphere. If $j = 0$, this is called the potential field case. Let us consider the linear force-free case first. In this case, we want to construct a field B, which satisfies

$$\nabla \times \mathbf{B} = \alpha \mathbf{B} \tag{1.7}$$

with a constant α.

If α is not constant in space, then we have the nonlinear force-free case. We can apply numerical methods to solve these equations. Here we introduce the *Wheatland et al.* [2000] method for this case. *Wiegelmann* [2007] defined a function in spherical geometry:

$$L = \int_V [\mathbf{B}^{-2} | (\nabla \times \mathbf{B}) \times \mathbf{B} |^2 + |\nabla \cdot \mathbf{B}|^2] d^3 x, \tag{1.8}$$

If L equals zero, the Eqs. 1.4 and 1.7 are fulfilled. The function can be numerically minimized by iteration. *Wiegelmann* [2008] compared the measurements of the magnetic field in an active region in the corona with the extrapolated results from the potential, linear, nonlinear force-free models, and found that the best agreement is from the nonlinear force-free model.

So far, the extrapolation of the potential field model has been widely applied in constructing the magnetic field in the solar corona. Figure 1.6 is the extrapolation result of the potential field model by *Wiegelmann and Solanki* [2005]. They also compared this result with the EIT (Extreme ultraviolet Imaging Telescope) image. This EIT image shows the line-of-sight integration of the FeXII emission line intensity at 195 Å. In the figure, the foot-points with the strong magnetic field correspond to the bright regions in the EIT image. The bright points correspond to locations at which the plasma density should be comparatively high at a temperature of about 1.5 MK.

Two methods have been applied to obtain the plasma information in the corona. One method is to apply scaling laws in loops. *Schrijver et al.* [2004] used this method to get the plasma distribution in the whole corona. Figure 1.7 shows their result. By comparing the model results with the observational images, they also found that the best assumption of the heat flux F_H is proportional to B/L, where B is the magnetic field strength and L is the half loop length. However, since the magnetic field is extrapolated by the potential field model, in which the plasma pressure is totally ignored, the MHS equilibrium will not be satisfied if we insert the plasma pressure from the scaling laws into Eq. 1.2. It means the scaling laws is not a self-consistent way to obtain the plasma information.

With the consideration concerning self-consistency, we go to the second method, which is extrapolating the magnetic field in the corona with magnetohydrostatic (MHS)

models. In these models, the Lorentz force, the plasma pressure and the gravity force are all considered and Eq. 1.2 will be satisfied. Not only the magnetic field but also the plasma will be extrapolated in the MHS models. Based on the work of *Low* [1985, 1991, 1992, 1993a and 1993b] and *Bogdan and Low* [1986], *Neukirch* [1995] constructed an analytic MHS model. We will apply this MHS model to extrapolate the distribution of the magnetic field and plasma in the solar corona. The boundary conditions of this model are given by a synoptic magnetogram on the inner boundary and by a source surface on the outer boundary. In the model, the electric current density can be decomposed into two components: one component is aligned with the magnetic field lines, whereas the other component flows in spherical shells. The second component of the current produces finite Lorentz forces that are balanced by the pressure gradient and the gravity force. The 3D distribution of not only the magnetic field but also the plasma will be derived self-consistently in this MHS model for the first time. By comparing the magnetic field distribution of our model with potential and force-free field models for the same boundary conditions, we find that the result from our model differs noticeably from both. The plasma density in this MHS model is higher in the equatorial plane than in the polar region, which is a reasonable result from the observations during solar activity minimum. In Chapter 2, the details of the application of this MHS model in the solar corona will be presented and discussed [*Ruan et al.,* 2008].

1.2   Solar wind

Starting around the middle of the nineteenth century, it was assumed that the Sun might eject intermittent particle beams [*Meyer-Vernet,* 2007]. The statement "The Earth was bombarded by intermittent beams of charged particles coming from the Sun and accelerated by an electrostatic field, just as an electrode in a giant vacuum tube" was made by J. J. Thomson around 1892. In 1890s, Kristian Birkleland, a Norwegian physicist, suggested that the Sun emits continuously charged particles, which escape into the interplanetary space. In the early 1950s, Ludwig Biermann, a German physicist, developed a model for the interaction of a comet with particles from the Sun, which could explain the comet's gaseous tails. The important achievement by Eugene Parker in 1958 was his prediction that the solar wind flows away from the Sun supersonically at several hundreds of kilometers per second. Since a hot debate followed Parker's theory, observational evidence was needed to settle the debate. Lunik II, a Russian spacecraft launched in 1959 detected a flux of positive ions with unknown velocity in the interplanetary space. The ultimate proof came in 1962 from an American spacecraft, Mariner 2, which provided clear evidence of the existence of and general properties of the solar wind.

The current sheet in the center of helmet streamers in the solar corona can extend into the heliospheric space by the solar wind and forms the heliospheric current sheet (HCS). This wavy current sheet serves as a magnetic separator between two regions of inward and outward Archimedean spiral fields, and organizes the large scale structure of the solar wind. Figure 1.8 shows an artist rendition of the heliospheric current sheet (HCS).
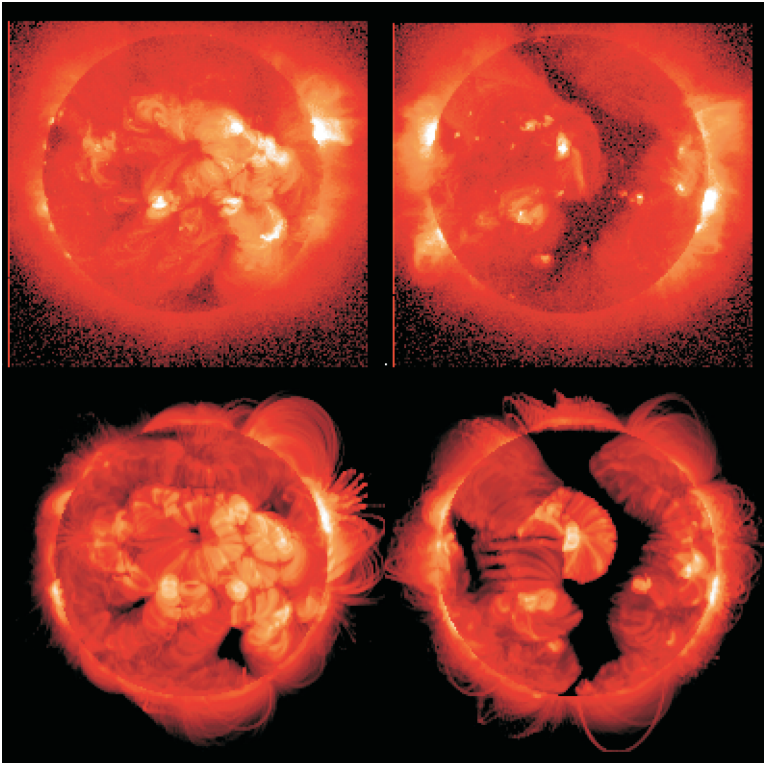
Figure 1.7: Comparison of Soft X-Ray Telescope (SXT) images (top row) on 1 December and 8 December 2000 with artificial images (bottom row) generated based on the potential field extrapolation and scaling laws [*Schrijver et al.,*, 2004].
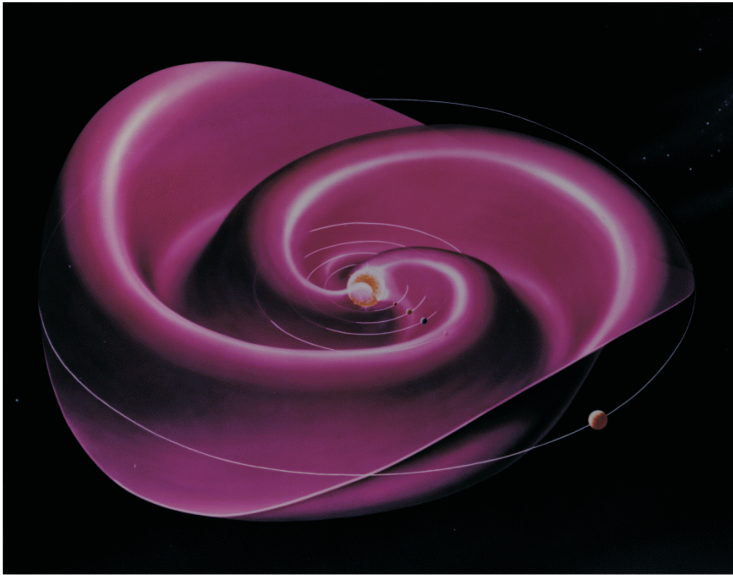
Figure 1.8: Artist's rendition of the Heliospheric Current Sheet (HCS).

1.2.1 Corotating interaction regions

The properties of the fast and slow solar wind in interplanetary space are established well based on in situ observations [reviewed in *Schwenn*, 1990 and *Meyer-Vernet,* 2007], but the nature of the their source regions are still not understood well. The fast solar wind might come from a large part of the solar surface near activity minimum, and not solely from the the coronal holes, whereas the slow solar wind might only come from the vicinity of active regions [*Woo and Habbal*, 2000; *Meyer-Vernet,* 2007]. When the fast solar wind runs into the slower plasma ahead in the interplanetary space, a Corotating Interaction Region (CIR) can be generated (Figure 1.9) [*Pizzo*, 1978]. So the CIRs are the consequence of the solar rotation and interaction between the fast solar wind and the slow solar wind. The forward and backward shocks related to the CIRs can be observed beyond of 1 AU [*Pizzo*, 1978].

1.2.2 Coronal mass ejections

A CME is "an observable change in coronal structure that occurs on a time scale of a few minutes to several hours and involves the appearance and outward motion of a new, discrete, bright, white-light feature in the coronagraph field of view" [*Schwenn*, 1996]. The current view of CMEs has improved considerably as the result of observations. Figure
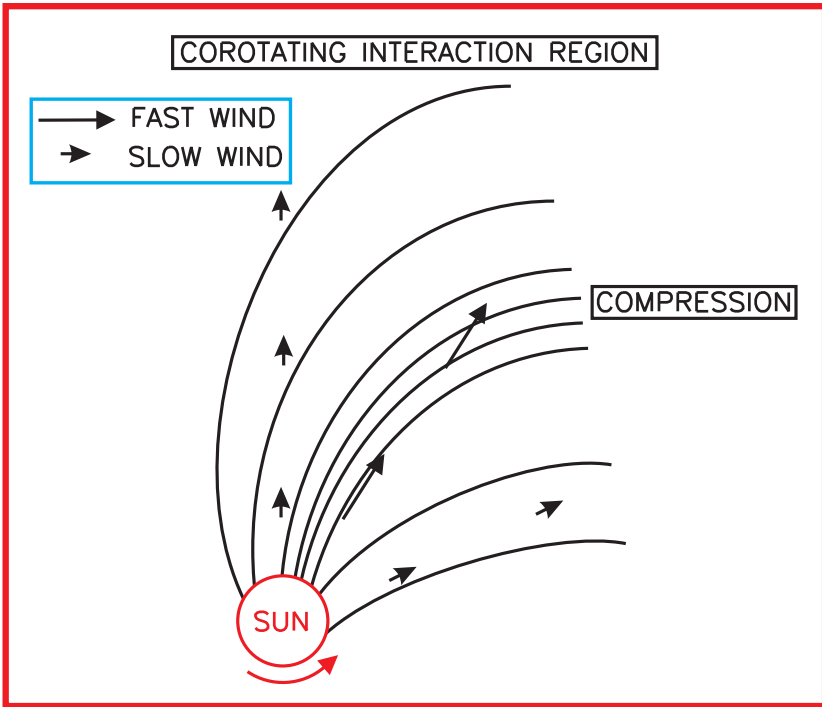
Figure 1.9: Schematic illustration of a Corotating Interaction Region (CIR) in the solar equatorial plane, adopted from [*Pizzo*, 1978].

1.10 shows observation of the evolution of a CME with white light coronagraph from High Altitude Observatory located on Hawaii. The trigger mechanism of the CMEs has been studied widely by theories and models, and the magnetic reconnection and/or kink instability may be responsible for triggering the CMEs [summarized in *Aschwanden*, 2005].

When a CME is transported into the heliospheric space by the solar wind, an ICME (Interplanetary coronal mass ejection) is generated, which can be identified by in situ observations, including magnetic field, plasma, compositional and energetic particle signatures [*Zurbuchen and Richardson*, 2006].

The signatures of the magnetic field are widely analyzed because the three-dimensional topology of the magnetic structure may be inferred from a single pass through an ICME when a particular model is assumed. A subset of ICMEs has enhanced magnetic fields which rotate slowly through a large angle. These ICMEs are named "magnetic clouds" (MC). A common feature within ICMEs is the reduction in the magnitude of the magnetic
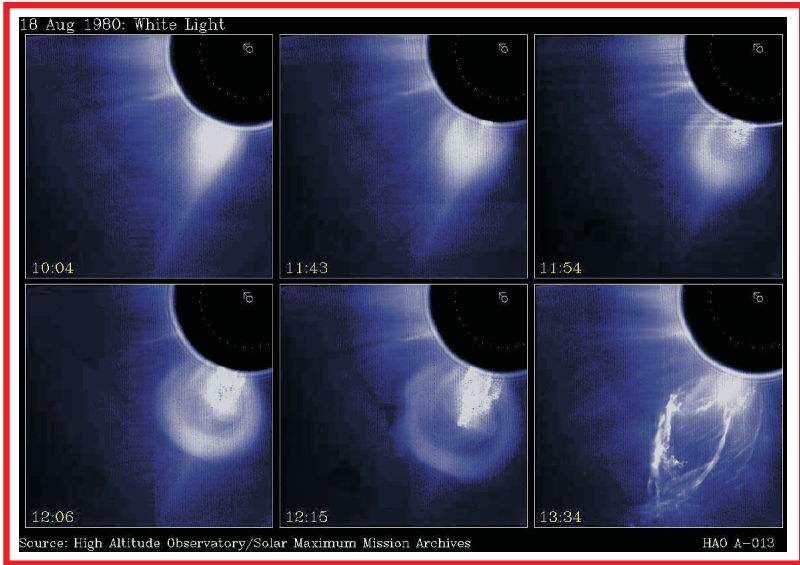
Figure 1.10: White-light coronagraph observations of a Coronal Mass Ejection (CME) on 18 August 1980 from High Altitude Observatory on the top panel.

field in their center. The magnetic field observations can help to identify the boundaries of the ICME. In principle, the boundary between the ICME and the ambient solar wind should be a tangential discontinuity. In the regular solar wind, we usually observe unidirectional beam electrons flowing away from the Sun. But inside ICMEs, bidirectional beams of suprathermal electrons (BDEs) can be usually observed [*Zwickl et al.*,1983]. The physical interpretation of the BDEs is that these electrons are flowing within ICMEs along magnetic field lines with two foot-points rooted at the Sun (Figure 1.11). Though BDEs are one of the most widely-used signatures for identifying ICMEs, BDEs may occur intermittently, or may even be absent, within an ICME [*Shodhan et al.*, 2000]. Their absence may indicate ICME field lines that result from the reconnection of open interplanetary magnetic field lines [*Gosling et al.* ,1995].

1.2.3 Flux ropes

Another type of similar magnetic structures in the solar wind are flux ropes. To avoid confusion, the flux ropes mentioned in this thesis do not include magnetic clouds, which can be large helix-type structures.

Flux ropes are widely observed in the Earth's magnetosphere [*Russell and Elphic*, 1978; *Elphic*, 1995; *Slavin et al.*, 2003], the Jovian Magnetosphere [*Walker and Russell*, 1985], the Mercury's magnetosphere [*Russell and Walker*, 1985], and in the solar wind [*Moldwin et al.*, 2000] by in situ observations. The comprehensive study of the flux ropes
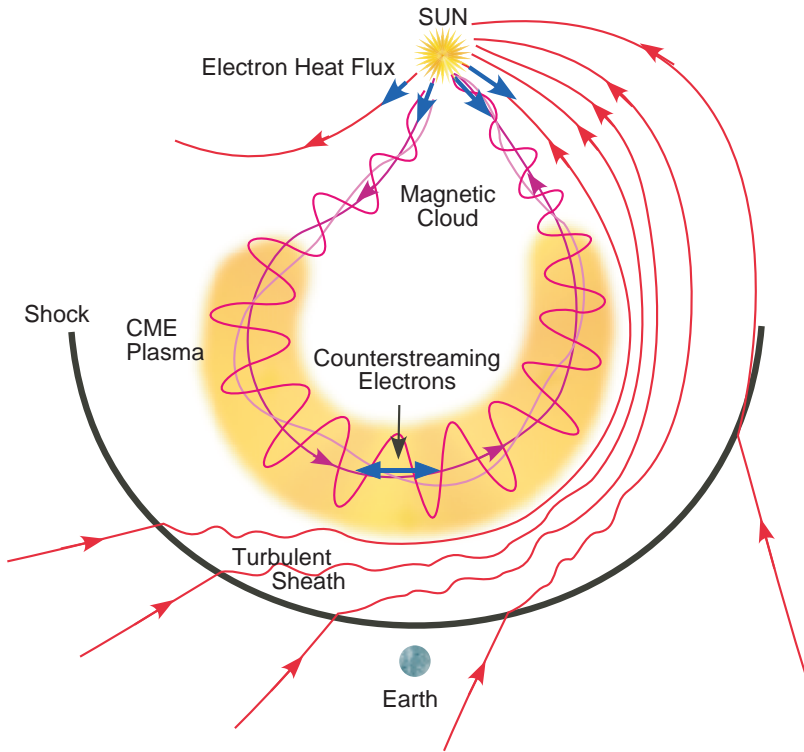
Figure 1.11: Artist rendition of a CME in the heliospheric space [*Zurbuchen and Richardson*, 2006].

has been taken in the Earth magnetotail by [*Slavin et al.*, 2003]. They compared the observations with a force-free model, and the comparison shows that these flux ropes are in the force-free state in the magnetotail. Figure 1.12 shows their result. The left panel is the schematic depiction of the flux rope. Long-dash, short-dash and dotted lines indicate magnetic field lines emanating from increasing distances from the central axis of the flux rope. The right panel contains the in situ magnetic field observations, and the solid line is the model result. They also suggested that multiple-X-line reconnection is responsible for these flux ropes. Figure 1.13 shows their suggestion of the multiple-X-line reconnection generating flux ropes in the magnetotail. The detailed topology of this dynamic process will be explained by Figure 3.7.

Though the flux ropes and magnetic clouds show observational signatures of a helical magnetic structure, *Moldwin et al.* [2000] identified several differences between these small-scale flux ropes and magnetic clouds in the solar wind. The average estimated diameter of magnetic clouds is around 6350 R_E [*Lepping et al.*, 1999], but the size of

these flux ropes is 20 times smaller than the averaged diameter of magnetic clouds. The plasma temperature inside the flux ropes shows little change compared to the surrounding environment, while the temperature in magnetic clouds is usually lower than the ambient solar wind, indicating cooler plasma. There is no expansion for flux ropes, but magnetic clouds usually show expansion at 1 AU. Based on these differences, *Moldwin et al.* [2000] suggested that the flux ropes might be generated by local magnetic reconnection in the solar wind, instead of being convected from the solar corona like magnetic clouds. *Feng et al.* [2007] carried out a statistical study about flux ropes and magnetic clouds. In contrast to the findings of *Moldwin et al.* [2000], *Feng et al.* [2007] found that the time scales of the flux ropes vary continuously from tens of minutes to tens of hours, and that the physical properties of the ropes, like energies, change slowly with the scales. Based on these results, they suggested that, like magnetic clouds, these interplanetary magnetic flux ropes are also manifestations of small coronal mass ejection (CME) events, which are too weak to appear in coronagraph observations. However, the statistical study of *Cartwright and Moldwin* [2008] on the flux ropes in the solar wind found that the size of the flux ropes appears to be bimodal, with the most events having less than four hours duration. This result suggests different source mechanisms for small-scale flux ropes and magnetic cloud.

Compared with the study on the flux ropes in the magnetosphere, further observations about the flux ropes in the solar wind are still needed to clarify their basic characteristics, such as the length, the diameter, and the possible generation mechanism. Regular in situ observations in the solar wind by the two STEREO A and B spacecraft now provide a perfect opportunity to study the scale of flux ropes. On 15 January 2007, an extended magnetic structure was observed consecutively by five spacecraft (ACE, WIND, STEREO A and B, and CLUSTER) in the solar wind. The similar bipolar magnetic field variations from five spacecraft suggest a two-dimensional magnetic structure. The abrupt disappearance of the beam electrons in the structure core suggests the magnetic isolation of the structure core from the surrounding environment. The analysis shows that this magnetic structure is a magnetic flux rope, which extends over at least 180 R_E in space. The length and orientation of the flux rope was determined by a local Minimum Variance Analysis (MVA) from individual spacecraft observations of the magnetic field and a timing analysis based on the joint observations by all five spacecraft. The result shows that the orientation of the flux rope stays constant in space and time. Though models suggested the flux rope could be an extending two-dimensional structure, our work proved this conclusion by multiple-spacecraft observations for the first time. The flux rope is embedded in a Corotating Interaction Region (CIR), which followed a magnetic cloud. The possible reconnection signatures have been found inside the flux rope. In Chapter 3, we will present the details of the observations of the flux rope [*Ruan et al.,* 2009] (accepted), which might contribute to the study and understanding of the flux ropes in the solar wind.
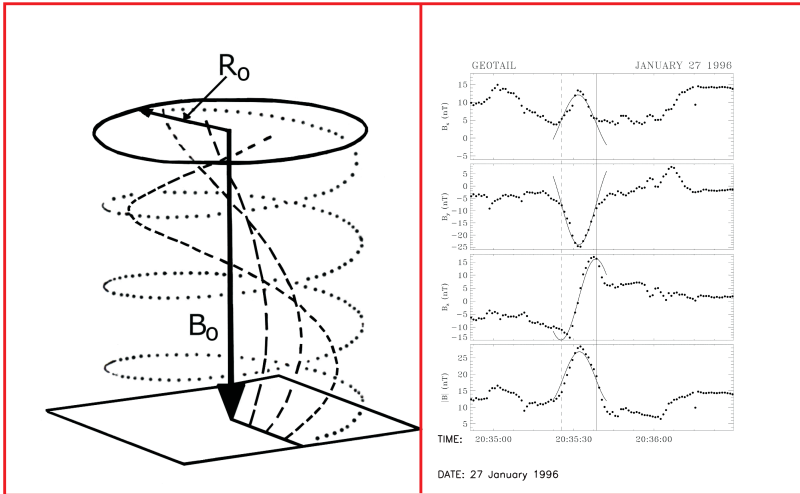
Figure 1.12: Schematic depiction of a helical flux rope (left panel) and in situ observations of a flux rope in the magnetotail (right panel) [*Slavin et al.*, 2001].
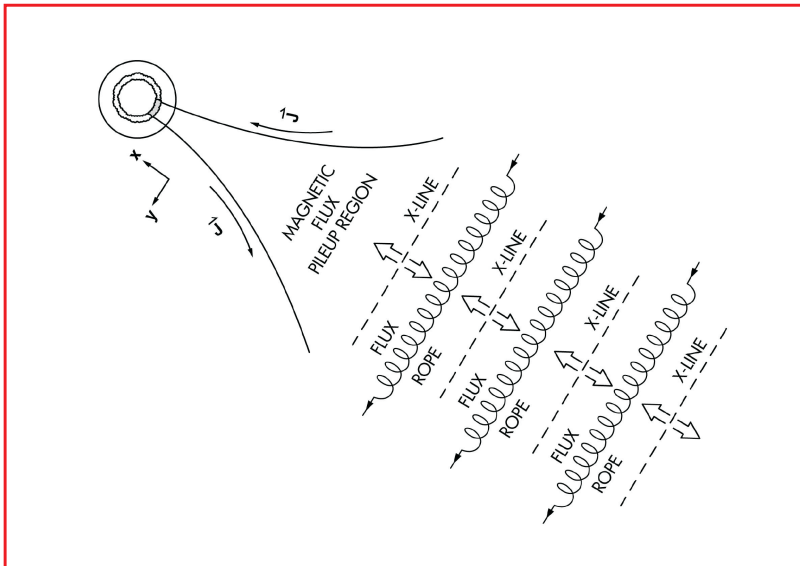

Figure 1.13: Sketch of multiple-X-line reconnection generating flux ropes in the magnetotail [*Slavin et al.*, 2001].

23

2 Magnetic field extrapolations in the solar corona

In this chapter we introduce the magnetic field extrapolation of the linear force-free model in the solar corona first [*Inhester,* 2006]. Next we describe the mathematics of an analytic magnetohydrostatic (MHS) model [*Neukirch,* 1995]. The application of this MHS model to the coronal magnetic field will be presented in the end of the thesis [*Ruan et al,* 2008].

To understand physical processes in the solar corona (e.g. flares and coronal mass ejections), it is important to obtain information about the magnetic field that couples the solar interior with the atmosphere. The Zeeman effect in magnetically sensitive spectral lines has been widely used to measure the line-of-sight component of the magnetic field typically ranging from one hundred gauss to several thousand gauss in the Sun's surface [*Lagg,* 2005]. The Hanle effect in selected spectral lines provides another useful diagnostic tool to measure magnetic fields in the plane normal to the line-of-sight direction. The magnetic field magnitude, which can be measured accurately from the Hanle effect, ranges typically from a milli-gauss to about one hundred gauss [*Lagg,* 2005]. Maps of the line-of-sight magnetic field (magnetogram) have been regularly recorded since many years, and more recently vector magnetograms have been measured. In the corona, however, it is more difficult to measure the magnetic field through the Zeeman effect due to the low plasma density and the weak emissions in the corona. Polarization of gyroresonance emission is a useful tool for measuring the coronal magnetic field strength [*White, et al.,* 2002], but not the full magnetic field vector.

An alternative way of estimating the magnetic field in the coronal is to extrapolate from photospheric measurements. The extrapolation result depends on not only the photospheric magnetogram, which serves as the boundary condition for the extrapolation, but also on the assumptions made regarding the coronal plasma and, in particular, the electric current density. The simplest approach for an extrapolation is to assume a current-free potential field, which has been widely used to extrapolate the coronal magnetic field into the corona in the past [*Hoeksema,* 1991]. In these potential models, the current-free condition is assumed between the photosphere and artificial source surface. Although these models are easy to construct and have demonstrated some success in reproducing large long-lived structures, details of magnetic structure are often not approximated well by these models, particularly in active regions [*Wiegelmann, et al.,* 2005]. A probable reason is that the current systems in active regions in the corona are substantial enough to cause the magnetic field to be distorted significantly from the potential field configuration [*Schrijver et al.,* 2005]. [*Wheatland,* 2000] suggested that the major nonpotentiality of the magnetic field in the active regions is not built up by persistent stressing of the surface field, but

instead emerges with the magnetic field from below the photosphere.

A more advanced approach is to construct force-free models, which contain field-aligned electric currents. The extrapolation with such LFFF models from a photospheric magnetogram has been shown to explain many of the observed features of filaments [*Aulanier, et al.,* 1998]. The force-free parameter α in LFFF models has been computed by comparing extrapolated magnetic field lines with coronal EUV-images [*Carcedo, et al.,* 2003] and three dimensional loops reconstructed by stereoscopy [*Wiegelmann, et al.,* 2002]. The LFFF models have also been used in combination with images from different viewpoints to stabilize the stereoscopic reconstruction of 3D coronal loop structures by [*Wiegelmann and Inhester, et al.,* 2006]. An advantage of LFFF models is that they only require photospheric line-of-sight magnetic field observations as input, but they have a free parameter and are not as accurate as the more sophisticated approaches like non-linear force-free field (NLFFF) models, which is the generic case for force-free fields. These NLFFF models are mathematically more challenging and require measurements of the photospheric magnetic field vector as input [*Aly,* 1989] [*Wiegelmann,* 2004]. Direct measurements of the magnetic field in an active region by [*Solanki, et al.,* 2003] have been compared with extrapolations under different model assumptions by [*Wiegelmann, et al.,* 2005]. The study revealed that the LFFF model is better than the potential field model, but is not as accurate as the NLFFF model.

The main reason for the success of force-free field model extrapolation is the low plasma β in the low corona, which means the magnetic field is the dominating quantity and plasma carried by the magnetic field has little influence on the field. However, from force-free models, we cannot derive the plasma density and pressure directly because all the plasma information is totally ignored in these models. Consequently, FFF models cannot by themselves predict coronal emission, which is important for the comparison with EUV and X-ray measurements. To circumvent this deficiency, scaling laws have been used to model the coronal plasma along magnetic loops [*Aschwanden, et al.,* 2000]. These methods –modelling first the coronal magnetic field and thereafter the plasma along the field lines– have been successfully applied to global potential fields by [*Schrijver, et al.,* 2004] and obtained reasonable agreement with observed plasma images. However, we cannot consider these models as completely satisfactory because they are not self-consistent. Complementary to these reconstructions based on observational data, self-consistent modelling approaches using magnetohydrostatics and magnetohydrodynamics have been developed [*Wu, et al.,* 1995] [*Wiegelmann, et al.,* 2000]. Theses models aim to describe coronal structures like helmet streamers and their association with coronal mass ejections and the solar wind.

2.1   Linear force-free model extrapolation

Here we summarize the mathematics of the linear force-free model [*Inhester,* 2006]. For the magnetic field $\mathbf{B}$ with $\nabla \cdot \mathbf{B} = 0$, we can decompose the field as

$$\mathbf{B} = \mathbf{P}(\phi) + \mathbf{T}(\psi), \qquad (2.1)$$

ϕ and ψ are two different arbitrary scalars, which are functions of space. (In the thesis, the bold symbols represent vectors, and non-bold symbols for scalars.)

We discuss the relations between the toroidal field and poloidal field. The toroidal field and the poloidal field can be expressed as

$$\mathbf{T}(\tau) = \nabla \times (\mathbf{r}\tau), \tag{2.2}$$
$$\mathbf{P}(\tau) = \nabla \times \nabla \times (\mathbf{r}\tau). \tag{2.3}$$

Here $\mathbf{r}$ is the radial vector and τ is an arbitrary scalar.

The toroidal field

$$\mathbf{T}(\tau) = \nabla \times (\mathbf{r}\tau) = -\mathbf{r} \times \nabla\tau \tag{2.4}$$

has no radial component. $\nabla \times \mathbf{r} = 0$ has been used. The poloidal field is the curl of the toroidal field (see the appendix)

$$\mathbf{P}(\tau) = \nabla \times \mathbf{T}(\tau) = \nabla\frac{\partial}{\partial r}(r\tau) - \mathbf{r}\triangle\tau \tag{2.5}$$

The curl of the poloidal field,

$$\nabla \times \mathbf{P}(\tau) = \nabla \times (\nabla\frac{\partial}{\partial r}(r\tau) - \mathbf{r}\triangle\tau) = -\nabla \times (\mathbf{r}\triangle\tau) = -\mathbf{T}(\triangle\tau), \tag{2.6}$$

is a toroidal field. So we can get

$$\mathbf{P}(\tau) = \nabla \times \mathbf{T}(\tau), \tag{2.7}$$
$$\nabla \times \mathbf{P}(\tau) = -\mathbf{T}(\triangle\tau), \tag{2.8}$$
$$\nabla \times (\nabla \times \mathbf{P}(\tau)) = -\nabla \times \mathbf{T}(\triangle\tau) = -\mathbf{P}(\triangle\tau) \tag{2.9}$$

In the linear force-free case, we want to construct a field $\mathbf{B}$ which satisfies

$$\nabla \times \mathbf{B} = \alpha\mathbf{B}, \tag{2.10}$$
$$\nabla \cdot \mathbf{B} = 0, \tag{2.11}$$

where α is constant in space. Taking the curl of the first equation, we get

$$\triangle\mathbf{B} = -\alpha^2\mathbf{B}. \tag{2.12}$$

Let's go back to Eq. 2.1. Since the curl of $\mathbf{B}$

$$\nabla \times \mathbf{B} = \nabla \times \mathbf{P}(\phi) + \nabla \times \mathbf{T}(\psi) = -\mathbf{T}(\triangle\phi) + \mathbf{P}(\psi) \tag{2.13}$$

(Eqs. 2.7 and 2.8 have been used for the above derivation.) must be equal to

$$\alpha\mathbf{B} = \alpha\mathbf{P}(\phi) + \alpha\mathbf{T}(\psi) = \mathbf{P}(\alpha\phi) + \mathbf{T}(\alpha\psi). \tag{2.14}$$

From the comparison of Eqs. 2.13 and 2.14, we get

$$\psi = \alpha\phi, \tag{2.15}$$
$$\alpha\psi = -\triangle\phi. \tag{2.16}$$

So we reach

$$\triangle\phi = -\alpha^2\phi. \tag{2.17}$$

Therefore we need find a solution for $\mathbf{B} = \mathbf{P}(\phi) + \alpha\mathbf{T}(\phi)$ with the Helmholtz equation $\triangle\phi = -\alpha^2\phi$. Given boundary conditions for the radial component of $\mathbf{B}$ on the sphere $r = 1$, the scalar ϕ is uniquely determined. We write the three components of $\mathbf{B}$ in terms of ϕ in spherical coordinate system,

$$B_r = |\alpha|(\frac{\partial^2}{\partial\rho^2} + 1)\rho\phi, \tag{2.18}$$

$$B_t = \frac{1}{r\cos\theta}(1 - t^2)\frac{\partial}{\partial t}\frac{\partial}{\partial\rho}\rho\phi - \frac{\alpha}{\cos\theta}\frac{\partial}{\partial p}\phi, \tag{2.19}$$

$$B_p = \frac{1}{r\cos\theta}\frac{\partial}{\partial p}\frac{\partial}{\partial\rho}\rho\phi + \frac{\alpha}{\cos\theta}(1 - t^2)\frac{\partial}{\partial t}\phi, \tag{2.20}$$

where $\rho = |\alpha|r$, $t = \sin\theta$, and θ and p are the polar angle and the azimuth angle, respectively.

For $\triangle\phi = -\alpha^2\phi$, we have

$$\phi = \sum_{n,m} F_n(r)P_n^m(t)C_n^m(p), \tag{2.21}$$

where $F_n(r)$ is the radial function, $P_n^m(t)$ the elevational function, $C_n^m(p)$ the azimuth function. The sum extends over $n = 0, ...N_{max}$ and for each n we have $m = 0, ...n$.

The radial function $F_n(r)$ obeys

$$\frac{1}{r^2}\frac{d}{dr}(r^2\frac{d}{dr}F_n) - \frac{n(n + 1)}{r^2}F_n = -\alpha^2 F_n. \tag{2.22}$$

The solutions are linear combinations of spherical Bessel functions of the first and second kind,

$$j_n(|\alpha|r) = \sqrt{\frac{\pi}{2|\alpha|r}}J_{n+1/2}(|\alpha|r), \tag{2.23}$$

$$y_n(|\alpha|r) = \sqrt{\frac{\pi}{2|\alpha|r}}Y_{n+1/2}(|\alpha|r), \tag{2.24}$$

which for small arguments approach

$$j_n(|\alpha|r) \rightarrow \frac{(|\alpha|r)^n}{1\times 3\times 5...(2n + 1)} = \frac{(|\alpha|r)^n}{(2n + 1)!!}, \tag{2.25}$$

$$y_n(|\alpha|r) \rightarrow \frac{-1\times 1\times 3...(2n - 1)}{(|\alpha|r)^{n+1}} = \frac{(2n - 1)!!}{(|\alpha|r)^{n+1}}. \tag{2.26}$$

So we got $F_n(\rho) = a_n y_n(\rho) + b_n j_n(\rho)$. We will discuss how to determine a_n and b_n from the boundary conditions, after we show the explicit expressions of the magnetic field components.

The elevational functions P_n^m are the associated Legendre functions [*Abramowitz and Stegun,* 1964], which obey

$$\frac{d}{dt}((1-t^2)\frac{d}{dt}P_n^m) + (n(n+1) - \frac{m^2}{1-t^2}P_n^m) = 0, \qquad (2.27)$$

and can be calculated from Rodriguez' formula as

$$P_n(t) = \frac{(-1)^n}{n!2^n}(\frac{d}{dt})^n(1-t^2)^n, \qquad (2.28)$$

$$P_n^m = (-1)^m \sqrt{1-t^2}(\frac{d}{dt})^m P_n. \qquad (2.29)$$

The azimuth functions C_n^m are linear combinations

$$C_n^m(p) = g_n^m \cos(mp) + h_n^m \sin(mp), \qquad (2.30)$$

where the constant g_n^m and h_n^m are the spherical harmonic coefficients to be determined by a least-square fit to the surface data.

Now by replacing ϕ in the equations (2.18) (2.19) (2.20), we get

$$B_r = \sum_{n,m} n(n+1)F_n P_n^m C_m^n, \qquad (2.31)$$

$$B_t = \frac{1}{r\cos\theta}\sum_{n,m}\overline{F_n}(1-t^2)\frac{dP_n^m}{dt}C_m^n - \frac{\alpha}{\cos\theta}\sum_{n,m}F_n P_n^m \frac{dC_m^n}{dp}, \qquad (2.32)$$

$$B_p = \frac{1}{r\cos\theta}\sum_{n,m}\overline{F_n}\frac{dC_m^n}{dp}P_m^n + \frac{\alpha}{\cos\theta}\sum_{n,m}F_n(1-t^2)C_n^m\frac{dP_m^n}{dt}. \qquad (2.33)$$

These three expressions are the spherical field components in terms of the spherical harmonic functions. Here $\overline{F_n(\rho)} = \frac{\partial}{\partial\rho}\rho F_n(\rho)$.

We have two boundaries for the model. One is photospheric magnetogram as the inner boundary, and the other one is the source surface as the outer boundary. We use these two boundary conditions to determine a_n and b_n in the expression of F_n. On the inner boundary at $r = 1$, we can choose $F_n = 1/n(n+1)$. So in that way, we can leave B_r as the function of only P_n^m and C_m^n, which are functions of θ and ϕ respectively. B_r will not depend on n on the inner boundary. On the source surface, we try to set the first two terms on the right hand side of Eqs. 2.32 and 2.33 as zero. This leads to another boundary condition of $\overline{F_n(\rho)} = 0$ at the source surface. With these two boundary conditions, the coefficients a_n and b_n can be determined. Crossing the source surface, we try to set the two second terms on the right hand side of Eqs. 2.32 and 2.33 as zero. What we did is just multiplying these two terms with $f(r)$, which decrease to zero exponentially crossing the source surface. From the white light coronagraph observations, it appears that the magnetic field lines become radially outside about three solar radii.

The next step is fitting the model result to the surface data, the photospheric magnetogram. The surface field from the model is $(B \cdot \mathbf{e}_{LOS})(t, p)$ at $r = 1$, which should be fitted to the observed line-of-sight magnetic field $D(t, p)$ at the solar surface. Here the $\mathbf{e}_{LOS}$ is the line-of-sight direction and we take $(\mathbf{e}_r \cos\theta - \mathbf{e}_t \sin\theta)$ as the form of $\mathbf{e}_{LOS}(t, p)$ for the synoptic view on the central meridian. So we should minimize

$$\sum_{t,p}(\mathbf{B}(r=1, t, p) \cdot \mathbf{e}_{LOS}(t, p) - D(t, p))^2 \rightarrow 0. \qquad (2.34)$$

Next we discuss how to deal with $(B(r = 1, t, p) \cdot \mathbf{e}_{LOS}(t, p)$. The explicit expressions of the magnetic field components have been shown in Eqs. 2.31, 2.32 and 2.33. The uncertain coefficients are located only in the term $C_m^n = g_n^m \cos(mp) + h_n^m \sin(mp)$. So we try to organize $\mathbf{B}(r = 1, t, p) \cdot \mathbf{e}_{LOS}(t, p)$ as the expression

$$\sum_{n,m}(H_n^m h_n^m + G_n^m g_n^m),$$

in which the uncertain coefficients h_n^m and g_n^m have been separated from H_n^m and G_n^m, respectively, and they are also separated from each other. If we insert Eqs. 2.31, 2.32 and 2.33 into $\mathbf{B}(r = 1, t, p) \cdot \mathbf{e}_{LOS}(t, p)$, we can obtain the expressions of H_n^m and G_n^m as the following,

$$H_n^m = (\mathbf{e}_{LOS} \cdot \mathbf{e}_r)n(n + 1)F_n P_n^m \cos(mp)$$

$$+(\mathbf{e}_{LOS} \cdot \mathbf{e}_t)\left(\frac{1}{r \cos \theta}\sum_{n,m}\overline{F_n}(1 - t^2)\frac{dP_n^m}{dt}\cos(mp) + \frac{\alpha}{\cos \theta}\sum_{n,m}F_n P_n^m \sin(mp)\right)$$

$$-(\mathbf{e}_{LOS} \cdot \mathbf{e}_p)\left(\frac{1}{r \cos \theta}\sum_{n,m}\overline{F_n}P_m^n \sin(mp) - \frac{\alpha}{\cos \theta}\sum_{n,m}F_n(1 - t^2)\frac{dP_m^n}{dt}\cos(mp)\right)$$

$$G_n^m = (\mathbf{e}_{LOS} \cdot \mathbf{e}_r)n(n + 1)F_n P_n^m \sin(mp)$$

$$+(\mathbf{e}_{LOS} \cdot \mathbf{e}_t)\left(\frac{1}{r \cos \theta}\sum_{n,m}\overline{F_n}(1 - t^2)\frac{dP_n^m}{dt}\sin(mp) - \frac{\alpha}{\cos \theta}\sum_{n,m}F_n P_n^m \cos(mp)\right)$$

$$+(\mathbf{e}_{LOS} \cdot \mathbf{e}_p)\left(\frac{1}{r \cos \theta}\sum_{n,m}\overline{F_n}P_m^n \cos(mp) + \frac{\alpha}{\cos \theta}\sum_{n,m}F_n(1 - t^2)\frac{dP_m^n}{dt}\sin(mp)\right)$$

From Eq. 2.34, we get

$$(\sum_{t,p}\sum_{n,m}(H_n^m h_n^m + G_n^m g_n^m) - D(t, p))^2 \to 0$$

We try to find the minimum value of $(\sum_{t,p}\sum_{n,m}(H_n^m h_n^m + G_n^m g_n^m) - D(t, p))^2$, therefore we reach

$$\frac{d}{dh_{n'}^{m'}}\sum_{t,p}(\sum_{n,m}(H_n^m h_n^m + G_n^m g_n^m) - D(t, p))^2$$

$$= 2\sum_{t,p}H_{n'}^{m'}(H_n^m h_n^m + G_n^m g_n^m) - D(t, p))$$

$$= 2\sum_{t,p}\sum_{n,m}\left((H_{n'}^{m'}H_n^m)h_n^m + (H_{n'}^{m'}G_n^m)g_n^m - (H_{n'}^{m'})D(t, p)\right) = 0,$$

and

$$\frac{d}{dg_{n'}^{m'}}\sum_{t,p}(\sum_{n,m}(H_n^m h_n^m + G_n^m g_n^m) - D(t, p))^2$$

$$= 2\sum_{t,p}G_{n'}^{m'}(H_n^m h_n^m + G_n^m g_n^m) - D(t, p))$$

$$= 2\sum_{t,p}\sum_{n,m}\left((G_{n'}^{m'}H_n^m)h_n^m + (G_{n'}^{m'}G_n^m)g_n^m - (G_{n'}^{m'})D(t, p)\right) = 0.$$

Then we write these two equations as a matrix equation

$$\begin{pmatrix} HH & HG \\ GH & GG \end{pmatrix} \begin{pmatrix} h \\ g \end{pmatrix} = \begin{pmatrix} HD \\ GD \end{pmatrix}$$

We ignored the indexes n and m in the matrix for the simplicity. Every element in the matrix is a sum over the grid points (t, p) on the boundary. By resolving this matrix equation with the method of singular value decomposition (SVD), we can obtain the coefficients h_n^m and g_n^m. The dimension of this matrix is $n_{max} \times n_{max}$. If we take 30 spherical harmonics for our calculation, the computer can finish this calculation in a reasonable time, like several or several tens minutes.

Figure 2.1 shows the synoptic photospheric chart (the color part) for Carrington rotation 1913 (from Aug. 22, 1996 to Sep. 18, 1996) obtained from the Wilcox Solar Observatory, and the fitted model result (the contour lines). The space resolution of the synoptic chart is 73 grid points in the longitude 30 grid points in the latitude. We take 10 spherical harmonics ($n = 10$) in the model. From this comparison, we see that the coefficients determined from the boundary condition are reliable. Figure 2.2 shows the global field lines from the force-free model extrapolation. In the top panel, the free parameter α is zero, which means potential field model. In the bottom panel, the α is 0.5. From this figure, we see that different α with the same boundary condition can bring significantly different extrapolation result. When we increase α in the model, the current density will increase, which leads to more twisted magnetic field lines. This can be seen from the figure.

2.2 Magnetohydrostatic (MHS) model

As mentioned above, the LFFF models cannot provide the plasma information directly, but MHS models can in principle. In this section we aim to use three-dimensional, self-consistent analytical MHS solutions as a basis for a model of the global corona, which has been proposed by [*Neukirch,* 1995]. In spite of the general difficulties associated with finding three-dimensional analytical solutions of the MHS equations, some useful solutions are available [*Low,* 1985, 1986, 1991, 1992] [*Neukirch,* 1995, 1997]. This class of solutions has a toroidal current density in additional to field-aligned current density. The solutions of [*Neukirch,* 1995] are based on the previous work by [*Bogdan and Low,* 1986] and differ from them only by the additional field-aligned current density component. The fundamental equation in this MHS model is a Schrödinger-type equation for the radial field component. The [*Bogdan and Low,* 1986] solutions have been discussed or used as a basis for global coronal magnetic field models, for example, by [*Zhao and Hoeksema,* 1993, 1994], and [*Gibson, et al.,* 1996], whereas so far the [*Neukirch,* 1995] solutions have been discussed but not used yet to extrapolate the coronal magnetic field from the photospheric magnetogram [*Rudenko,* 2001].

Here we use the [*Neukirch,* 1995] (subsequently referred to as N95) MHS solutions to develop a global coronal model using photospheric magnetograms as input for the magnetic field. We are aiming for a model that describes the coronal magnetic field and plasma self-consistently. We summarize Neukirch (1995)'s MHS model and their results, and introduce a modification to the model for its application to extrapolate the measured

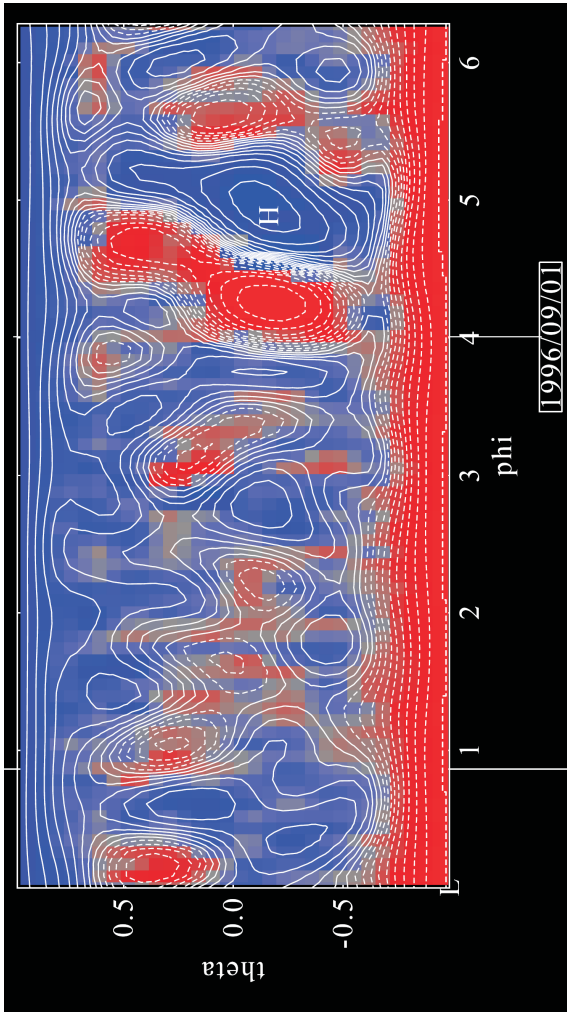Figure 2.1: Synoptic photospheric chart (the color part) for Carrington rotation 1913 (from Aug. 22, 1996 to Sep. 18, 1996) obtained from the Wilcox Solar Observatory and the linear force-free model result (the contour lines), adjusted from [*Inhester,* 2006].
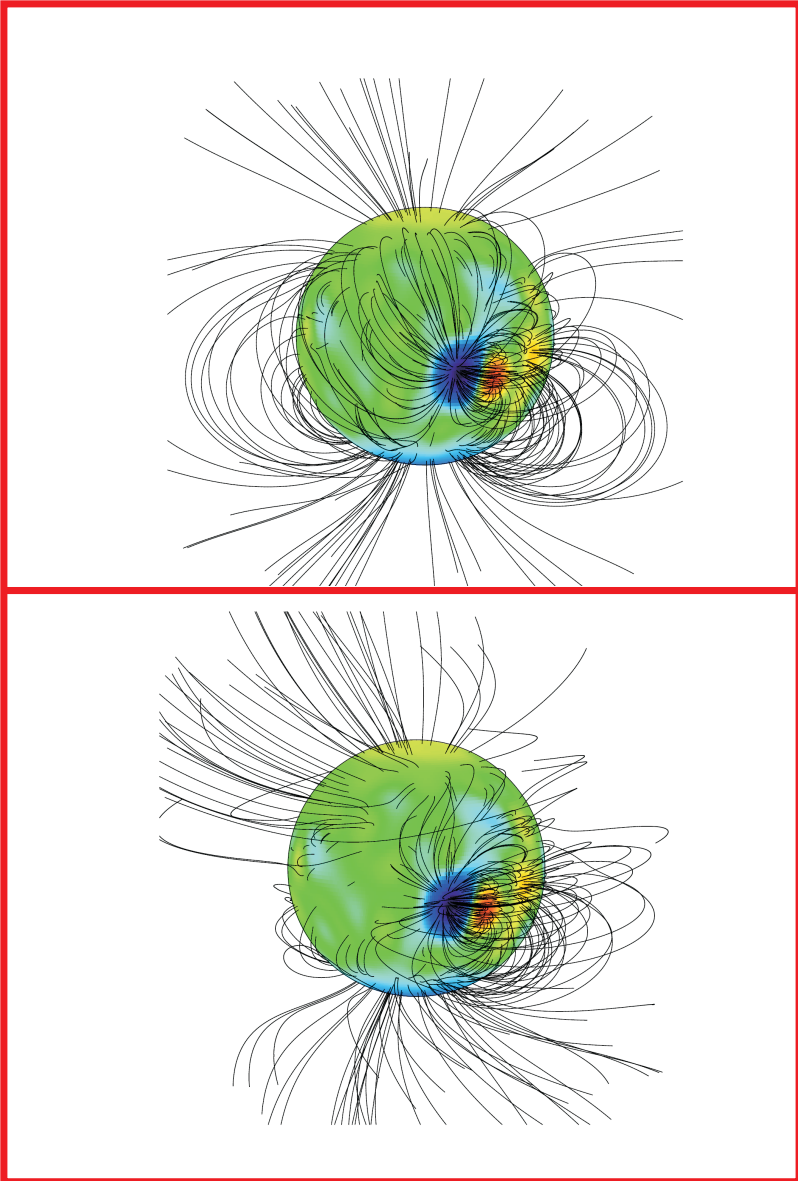
Figure 2.2: Magnetic field lines from potential field (the top panel) and linear force-free field with $\alpha = 0.5$ (the bottom panel), adjusted from [*Inhester*, 2006].

photospheric magnetogram into the solar corona. Some lengthy and necessary mathematical details in deriving equations are included in the appendix.

2.2.1   Mathematics of the MHS model

The basis for the MHS model consists of the MHS equations:

$$
\begin{align}
\mathbf{j} \times \mathbf{B} - \nabla p - \rho \nabla \Phi &= 0, \tag{2.35}\\
\nabla \times \mathbf{B} &= \mu_0 \mathbf{j}, \tag{2.36}\\
\nabla \cdot \mathbf{B} &= 0. \tag{2.37}
\end{align}
$$

Here, $\mathbf{j}$ and $\mathbf{B}$ are the electric current density and the magnetic field, respectively, p is the plasma pressure, ρ the plasma density, Φ the gravitational potential, and μ_0 the permeability of vacuum.

In N95 the electric current was decomposed into two components:

$$\mu_0 \mathbf{j} = \alpha \mathbf{B} + \varepsilon(r)[\nabla(\mathbf{r} \cdot \mathbf{B})] \times \mathbf{r}, \tag{2.38}$$

where $\varepsilon(r) = 1/r^2 - 1/(r + a)^2$ is a special choice in our model. We will discuss how to choose this term later. Both α and a are two free parameters in this model that are globally constant. The first term describes the field-aligned current density, the second a toroidal current density that produces the Lorentz force to compensate for pressure gradient and gravity.

Inserting Eq. 2.38 into Eq. 2.36, taking the curl of Eq. 2.36 and dotting the resulting equation with $\mathbf{r}$, they obtained

$$\Delta(\mathbf{r} \cdot \mathbf{B}) + \varepsilon(r)\mathbf{L}^2(\mathbf{r} \cdot \mathbf{B}) + (\alpha)^2(\mathbf{r} \cdot \mathbf{B}) = 0, \tag{2.39}$$

where $\mathbf{L}$ is the angular momentum operator,

$$\mathbf{L} = \frac{1}{i}\mathbf{r} \times \nabla, \tag{2.40}$$

and i is the imaginary unit. $\mathbf{L}$ has the property

$$\mathbf{L} \cdot \mathbf{B} = \frac{1}{i}\alpha \mathbf{r} \cdot \mathbf{B}. \tag{2.41}$$

By expanding $\mathbf{r} \cdot \mathbf{B}$ into a series of spherical harmonics [*Jackson,* 1975] ,

$$\mathbf{r} \cdot \mathbf{B} = \sum_{l=1}^{\infty} \sum_{m=-l}^{l} l(l+1) \left(\sum_{j=1}^{2} A_{lm}^{(j)} u_l^{(j)}(r) \right) Y_l^m(\theta, \phi). \tag{2.42}$$

and inserting this expression to Eq. 2.39, they obtained

$$\frac{d^2 g_l^{(j)}}{dr^2} - l(l+1)(\frac{1}{r^2} - \varepsilon(r))g_l^{(j)} + \alpha^2 g_l^{(j)} = 0. \tag{2.43}$$

Here $g_l^{(j)}(r) = ru_l^{(j)}(r)$. Now we discuss how to specify $\varepsilon(r)$. First we write the radial Schrödinger equation for the hydrogen atom for comparison:

$$\frac{d^2 g_l^{(j)}}{dr^2} - \left(l(l+1)\frac{1}{r^2} - \frac{2}{r} \right) g_l^{(j)} + 2E g_l^{(j)} = 0. \tag{2.44}$$

Here E is independent of r like α. The term $2/r$ is the potential part. The term $\varepsilon(r)$ in Eq. 2.43 corresponds the potential part $2/r$ in Eq. 2.43. However, there is a difference that in Eq. 2.43 the operator $l(l+1)$ does not appear as the numerator of the $1/r^2$, but also as a factor of the potential $\varepsilon(r)$. Eq. 2.44 has been well studied in quantum mechanics, and the analytic solution has been found for this equation. With this help N95 try to find an analytic solution for Eq. 2.43. They specified $\varepsilon(r) = 1/r^2 - 1/(r+a)^2$, and found the solution for Eq. 2.43 as $g_l^{(j)} = \sqrt{r+a}J_{l+1/2}(\alpha(r+a))$ or $\sqrt{r+a}N_{l+1/2}(\alpha(r+a))$, where J and N are first and second kinds of the Bessel function. They made this choice for $\varepsilon(r)$ in order to find an analytic solution. In principle we can make other choices for $\varepsilon(r)$ by giving up the analytic solutions. In those cases, we have to solve Eq. 2.43 numerically.

By inserting Eq. 2.42 into Eq. 2.41, they obtained

$$\mathbf{L} \cdot \mathbf{B} = \frac{1}{i}\alpha \sum_{l=1}^{\infty} \sum_{m=-l}^{l} \left(l(l+1) \sum_{j=1}^{2} A_{lm}^{(j)} u_l^{(j)}(r) \right) Y_l^m(\theta, \phi). \tag{2.45}$$

[*Jackson,* 1975] provided a solution for this equation without giving the B_r component as the following (see the appendix for the details),

$$\mathbf{B_t} = \sum_{l=1}^{\infty} \sum_{m=-l}^{l} v_{lm}(r)\mathbf{L}Y_l^m(\theta, \phi) + w_{lm}(r)\nabla Y_l^m(\theta, \phi), \tag{2.46}$$

$$v_{lm}(r) = \frac{1}{i}\alpha \sum_{j=1}^{2} A_{lm}^{(j)} u_l^{(j)}(r), \tag{2.47}$$

$$w_{lm}(r) = \sum_{j=1}^{2} A_{lm}^{(j)} \frac{d}{dr}\left(ru_l^{(j)}(r) \right). \tag{2.48}$$

By combining Eqs. 2.42, 2.46, 2.47 and 2.48, N95 obtained an explicit expression for the magnetic field:

$$\mathbf{B} = \sum_{l=1}^{\infty} \sum_{m=-l}^{l} \sum_{j=1}^{2} A_{lm}^{(j)}\{l(l+1)u_l^{(j)}(r)\frac{\mathbf{r}}{r^2}Y_l^m(\theta, \phi) \; +$$
$$\frac{\alpha}{i}u_l^{(j)}(r)\mathbf{L}Y_l^m(\theta, \phi) \; +$$
$$\frac{d(ru_l^{(j)})}{dr}\nabla Y_l^m(\theta, \phi)\} \tag{2.49}$$

$$\begin{pmatrix} u_l^{(1)}(r) \\ u_l^{(2)}(r) \end{pmatrix}, = \frac{\sqrt{r+a}}{r}\begin{pmatrix} J_{l+1/2}(\alpha(r+a)) \\ N_{l+1/2}(\alpha(r+a)) \end{pmatrix}, \tag{2.50}$$

In Eq. 2.50 l starts from 1 not 0 in order to rule out a magnetic monopole term. The variable $A_{lm}^{(j)}$ are a priori unknown coefficients to be determined from the boundary condition supplied by the photospheric magnetogram.

Next we discuss how they obtained the expression of the plasma pressure and density with the help of the MHS equilibrium equation 2.35. Before that, we rewrite $\varepsilon(r)[\nabla(\mathbf{r} \cdot \mathbf{B})] \times \mathbf{r}$ in Eq. 2.38 as another expression $\nabla F \times \nabla\Phi$. As mentioned above, Φ is the gravitational potential, so

$$\Phi = -\frac{GM}{r}, \tag{2.51}$$

$$\nabla\Phi = \frac{GM}{r^3}\mathbf{r}. \tag{2.52}$$

If the expression of F is

$$F = \frac{\varepsilon(r)r}{|\nabla\Phi|}\mathbf{r} \cdot \mathbf{B} = \frac{\varepsilon(r)r^2}{(\nabla\Phi)^2}(\mathbf{B} \cdot \nabla\Phi), \tag{2.53}$$

the following equation can be reached

$$\nabla F \times \nabla\Phi = \varepsilon(r)\nabla(\mathbf{r} \cdot \mathbf{B}) \times \mathbf{r}. \tag{2.54}$$

This is not complicate if we notice that the vector $\nabla[\varepsilon(r)r/(\nabla\Phi)]$ is parallel along $\mathbf{r}$, and the result is zero if we multiply this vector with $\nabla\Phi$. So Eq. 2.38 reaches

$$\mu_0\mathbf{j} = \alpha\mathbf{B} + \nabla F \times \nabla\Phi, \tag{2.55}$$

The term $\nabla F \times \nabla\Phi$ represents the current is generated by two independent sets of level surfaces F and Φ [Low, 1985].

Inserting Eq. 2.55 to Eq. 2.35 and rearranging the cross-products, they got

$$\nabla p + \rho\nabla\Phi + (\mathbf{B} \cdot \nabla\Phi)\nabla F - (\mathbf{B} \cdot \nabla F)\nabla\Phi = 0. \tag{2.56}$$

Since$\nabla\Phi$ and ∇F are independent, by considering the component of ∇p in direction of ∇F projected to the plane $\Phi = constant$, one obtains

$$\left(\frac{\partial p}{\partial F}\right)_\Phi = -\mathbf{B} \cdot \nabla\Phi = -\frac{F}{k(\Phi)}. \tag{2.57}$$

Here Eq. 2.53 is used, and $k(\Phi) = \varepsilon(r)r^2/(\nabla\Phi)^2$. This equation can be directly integrated to give

$$p = p_0(\Phi) - \frac{F^2}{2k(\Phi)}. \tag{2.58}$$

Here p_0 is a free function and represents a background pressure, which depends only on r. Inserting the explicit expressions of F and $k(\Phi)$, the following equation can be reached

$$p = p_0(r) - \frac{1}{2}\varepsilon(r)(\mathbf{r} \cdot \mathbf{B})^2. \tag{2.59}$$

In a similar way, by considering the component of ∇p in direction of $\nabla\Phi$ projected to the plane $F = constant$ in Eq. 2.56, one can obtain

$$\rho = -\left(\frac{\partial p}{\partial\Phi}\right)_F + \mathbf{B} \cdot \nabla F. \tag{2.60}$$

By inserting Eq. 2.59 for p, changing the derivation from Φ to r, and inserting the expression of F, one can obtain

$$\rho = \frac{r^2}{GM}\left(0.5\frac{d\varepsilon}{dr}(\mathbf{r}\cdot\mathbf{B})^2 + r\varepsilon\mathbf{B}\cdot\nabla(\mathbf{r}\cdot\mathbf{B}) - \frac{dp_0}{dr}\right), \tag{2.61}$$

where $\rho_0 = -(r^2/GM)dp_0/dr$ is a background plasma density. The plasma temperature can be calculated by

$$T = \frac{\mu p}{\rho R}, \tag{2.62}$$

where R is the universal gas constant and μ is the mean molecular weight.

Two components of the current density are present in Eq. 2.38. The first term of the current $\alpha\mathbf{B}$ is the force-free part, and it does not produce a Lorenz force on the plasma because it is parallel to the field lines. The second term $\varepsilon(r)\nabla(\mathbf{r}\cdot\mathbf{B})\times\mathbf{r}$ is perpendicular to the radial direction, i.e. It flows on spherical surfaces. In general this current density component produces a Lorenz force which balances the pressure gradient ∇p and the gravity force $\rho\nabla\Phi$ in Eq. 2.35.

Though N95 did not apply the model to extrapolate the magnetic field with photospheric magnetogram, they provided a simple example of the model result. This example includes only the spherical harmonics for $l = 1$, $m = 0$ and $l = 2$, $m = \pm 1$. The magnetic field components are

$$B_r = A_{10}\frac{r_0^2}{r^2}\frac{r_0 + a}{r + a}f_1(r)Y_1^0 -$$
$$\frac{1}{2}A_{21}\frac{r_0^2}{r^2}\frac{(r_0 + a)^2}{(r + a)^2}f_2(r)(Y_2^1 - Y_2^{-1}),$$

$$B_\theta = \frac{1}{2}A_{10}\frac{r_0^2}{r}\frac{r_0 + a}{r + a}\left(\frac{df_1}{dr} - \frac{f_1}{r + a}\right)\frac{\partial}{\partial\theta}Y_1^0 -$$
$$\frac{\alpha}{12}A_{21}\frac{r_0^2}{r}\frac{(r_0 + a)^2}{(r + a)^2}f_2(r)\frac{1}{\sin\theta}\frac{\partial}{\partial\phi}(Y_2^1 - Y_2^{-1}) +$$
$$\frac{1}{12}A_{21}\frac{r_0^2}{r}\frac{(r_0 + a)^2}{(r + a)^2}\left(\frac{df_2}{dr} - \frac{2f_2}{r + a}\right)\frac{\partial}{\partial\theta}(Y_2^1 - Y_2^{-1}),$$

$$B_\phi = -\frac{\alpha}{2}A_{10}\frac{r_0^2}{r}\frac{r_0 + a}{r + a}f_1(r)\frac{\partial}{\partial\theta}Y_1^0 +$$
$$\frac{1}{12}A_{21}\frac{r_0^2}{r}\frac{(r_0 + a)^2}{(r + a)^2}f_2(r)\frac{\partial}{\partial\theta}(Y_2^1 - Y_2^{-1}) +$$
$$\frac{1}{12}A_{21}\frac{r_0^2}{r}\frac{(r_0 + a)^2}{(r + a)^2}\left(\frac{df_2}{dr} - \frac{2f_2}{r + a}\right)\frac{1}{\sin\theta}\frac{\partial}{\partial\phi}(Y_2^1 - Y_2^{-1}),$$

where

$$f_1(r) = \frac{\cos q + q \sin q}{\cos q_0 + q_0 \sin q_0},$$
$$f_2(r) = \frac{(3 - q^2)\cos q + 3q \sin q}{(3 - q_0^2)\cos q_0 + 3q_0 \sin q_0},$$
$$q = \alpha(r + a),$$
$$q_0 = \alpha(r_0 + a).$$

N95 took $r_0 = 1.5 R_\odot$ ($R_\odot$ is the solar radius.), $a = 0.01 r_0$. They took the same plasma background model as [*Bogdan and Low*, 1986],

$$\rho_0(r) = 2.87 \times 10^{-15} \times \left(c_1(r/r_0)^{-d_1} + c_2(r/r_0)^{-d_2}\right),$$
$$p_0(r) = 7.9 \times 10^{-5} \times \left(C_1(r/r_0)^{-d_1-1} + C_2(r/r_0)^{-d_2-1}\right),$$
$$c_1 = 0.804, C_1 = 0.866, d_1 = 3.3,$$
$$c_2 = 0.196, C_2 = 0.134, d_2 = 5.8.$$

By varying α from 0 to 0.1 in the extrapolation, N95 found that the differences in the magnetic field are obvious, but the plasma quantities are almost the same (see Figures. 1, 2, 3 and 4 of N95). N95 suggested that the magnitude change of the radial magnetic field component is only about 1% between $\alpha = 0$ and $\alpha = 0.1$, and that this small change of the magnetic field strength hardly alter the plasma.

2.2.2 Application of the MHS model to the corona

In our application to the solar corona, we take both the first and second kinds of Bessel function as given in Eq 2.50. Figure 2.3 shows a schematic illustration of our model. We place the source surface at 2.5 solar radii. Between the photosphere and the source surface, the magnetic field is given by the MHS model of N95. Outside of this boundary the magnetic field lines are purely radial.

In panel (a) of Figure 2.4, we plot the synoptic photospheric chart (for Carrington rotation 1919 from Feb. 1, 1997 to Mar. 1, 1997 in the solar minimum) of the radial magnetic field obtained from the Wilcox Solar Observatory, which is the inner boundary condition. Note that, because of the reduced spatial resolution at higher latitude introduced by foreshortening, magnetic flux is underestimated there, in particular in regions of mixed magnetic polarity [*Krivova, et al.*, 2004]. There are 72 grid points in longitude direction and 30 grid points in latitude direction for this observation in the whole photosphere. The following panels display the radial field resulting from the MHS model with different numbers of spherical harmonics at 1 solar radius. When we take only five spherical harmonics ($N_{max} = 5$), the model can give the general distribution of the magnetic field (the panel (b)). If we increase N_{max} to 10 and 20, increasingly smaller structures become visible; see panel (c) and (d). For $N_{max} = 30$, the model output is very similar to the observation (panel (e)). If we take 40 spherical harmonics, the numerical noise in the model starts having a visible impact and produces structure especially in the polar regions (panel (f)), so we specify $N_{max} = 30$ for the following calculation.

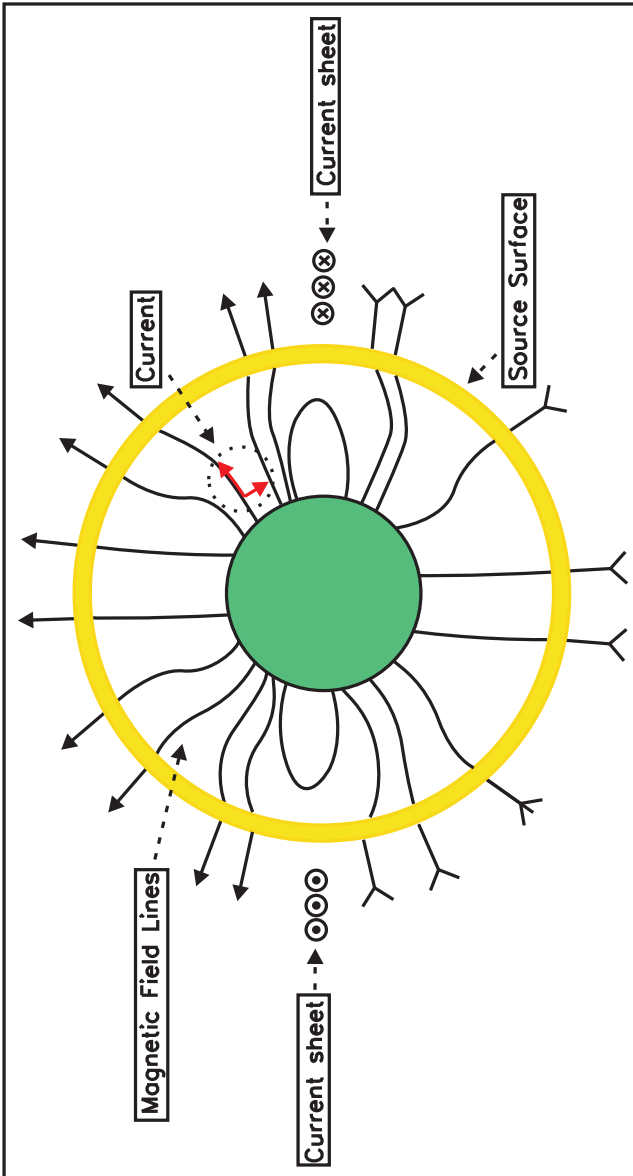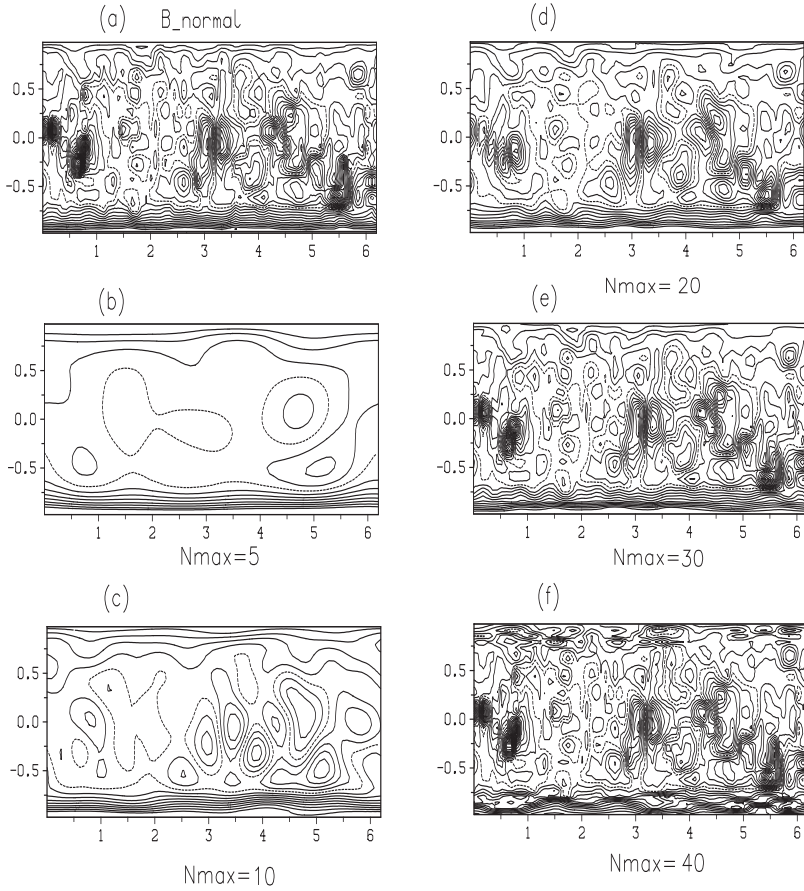Figure 2.3: Schematic illustration of the MHS model [*Ruan, et al.,* 2008].

Figure 2.4: Radial component of the synoptic photospheric magnetic field for Carrington rotation 1919 (the panel (a)) and the radial component of the magnetic field from the MHS model with different numbers of spherical harmonics (N_{max}). The x-axis contains the longitude from 0 to 2π and the y-axis the sin of the latitude. [*Ruan, et al., 2008*]

In the following we compute the plasma structure self-consistently. Eq. 2.35 can be decomposed into the following two equations:

$$\mathbf{j} \times \mathbf{B} - \nabla p_{pb} - \rho_{pb} \nabla \psi \;=\; 0, \tag{2.63}$$

$$-\nabla p_{bg} - \rho_{bg} \nabla \psi \;=\; 0. \tag{2.64}$$

Here p_{bg} and ρ_{bg} are the background plasma pressure and density, respectively. They are homogenous in the corona and only functions of r. The p_{pb} and ρ_{pb} are perturbations of pressure and density produced by the magnetic field. They are functions of r, θ, ϕ. The Lorentz force $\mathbf{j} \times \mathbf{B}$ will cause the perturbation in the plasma and is balanced by the pressure gradient and the gravity. The background plasma balances itself without the magnetic field.

The total pressure and density functions are the sum of the perturbation part pb and the background part bg:

$$p(r, \theta, \phi) \;=\; p_{bg}(r) + p_{pb}(r, \theta, \phi), \tag{2.65}$$

$$\rho(r, \theta, \phi) \;=\; \rho_{bg}(r) + \rho_{pb}(r, \theta, \phi). \tag{2.66}$$

Eq. 2.59 implies that the perturbation pressure can be calculated analytically, whereas the perturbation density must be calculated numerically from Eq. 2.61. With setting $N_{max} = 30$, we compute the ρ_{pb} independently from Eqs. 2.61 and 2.63. For Eq. 2.63 we calculate the perturbation pressure by Eq. 2.59 first. By comparing the densities from these two different methods, we check the accuracy of our calculation. We define the error I as

$$I = \left(\frac{1}{N} \sum_{k=1}^{n} \frac{|\rho_{pb(k)}^{(2.61)} - \rho_{pb(k)}^{(2.63)}|}{\rho_{pb(k)}^{(2.61)}} \right), \tag{2.67}$$

where $\rho_{pb(k)}^{(2.61)}$ and $\rho_{pb(k)}^{(2.63)}$ denote the perturbation densities at grid points derived from Eqs. 2.61 and 2.63, respectively. There, N is the total number of the grid points in the entire computational domain. We find that I decreases to less than 4% when we put 80 grid points in the radial direction, 180 grid points in the θ direction, and 360 grid points in the ϕ direction for 30 spherical harmonics. This means the result of our calculations is consistent except for a small discretization error.

From Eqs. 2.59 and 2.61, we find that the perturbation pressure is always negative and the perturbation density could be negative in some places. Our model shows the strongest perturbation is always located in the lower coronal layers of active regions. This imposes a requirement to insert a background plasma to compensate for the negative perturbation plasma density.

We use Eq. 2.64 to compute the background plasma as a stratified atmosphere. We also need the equation of state:

$$p_{bg} = 2n_{bg}kT_{bg}, \tag{2.68}$$

where T_{bg} and n_{bg} are the background temperature and electron number density. Consequently, for the background, we have two equations (Eqs. 2.64 and 2.68) and three variables: temperature, pressure and density. We can make assumptions for one variable (like the density) and calculate the other two variables from the equations.

On the one hand, as mentioned above, the perturbation density could be negative so that we need to apply a large enough background density in order to make the total density, which is the sum of the perturbation part and the background part, positive. On the other hand, we cannot make the background density too high. If the background is too large compared with the perturbation part, the mean plasma density will be much larger than values expected from coronagraph observations.

The Baumbach-Allen formula [*Cox, 2000*] gives an average density for the background plasma density distribution in the corona:

$$n(r) = 10^8[2.99(\frac{r}{r_\odot})^{-16} + 1.55(\frac{r}{r_\odot})^{-6} + 0.036(\frac{r}{r_\odot})^{-1.5}], \qquad (2.69)$$

where $r_\odot$ is the solar radius. This expression should be a good approximation in the quiet region. For active regions, the observed density could be ten times larger [*Aschwanden, 2005*]. We make some modifications to this formula for our background plasma. Our modified background plasma is given by the expression

$$n_{bg}(r) = 10^8[10^5(\frac{r}{r_\odot})^{-50} + 97.0(\frac{r}{r_\odot})^{-16} + \qquad (2.70)$$
$$28.0(\frac{r}{r_\odot})^{-6} + 0.2(\frac{r}{r_\odot})^{-1.5}].$$

As mentioned above, the strongest perturbation of the plasma density appears in the low corona, so we have to increase our background in the low corona. To take this into account, we add a term to the right hand side, which decreases very rapidly with r, so that it does not affect the outer corona. We also change the coefficients for the three other terms to keep the plasma density positive in the outer corona. Through Eqs. 2.64, 2.68, and 2.70, we calculate the background plasma temperature. The stratification of the background temperature and density is given in Figure 2.5. From the right panel of the figure, we find the background temperature is in a reasonable range when $r \geq 1.4$. But in the low corona ($r < 1.4$), the background temperature is unreasonably low due to the first term in Eq. 2.70.

Finally, through Eqs. 2.62, 2.65, and 2.66, we obtain the total plasma pressure, density, and temperature, respectively.

Field Lines. Figure 2.6 shows the magnetic field lines in the whole corona. Panel (a) displays the potential field extrapolation, which has no free parameters. Panel (b) exhibits the result of the LFFF model extrapolation. This model contains the force-free parameter α and we use $\alpha = 0.4$. In panel (c) we show the MHS model field lines. Here we use $\alpha = 0.4$ and $a = 0.2$. Since $\mu_0\mathbf{j} = \alpha\mathbf{B} + \varepsilon(r)[\nabla(\mathbf{r} \cdot \mathbf{B})] \times \mathbf{r}$ and $\varepsilon(r) = 1/r^2 - 1/(r + a)^2$, the current density will increase in average if we increase the parameters α and a. From this figure it is clear that– though the measured photospheric boundary conditions are the same – the different models generated different distributions of the magnetic field in the corona.

Current sheet and plasma density in the source surface. Figure 2.7 shows the radial component of the magnetic field and the current sheet on the source surface, as obtained from the potential field model (panel (a) with $\alpha = 0$ and $a = 0$), LFFF model (panel (b) with $\alpha = 0.4$ and $a = 0$), and MHS model (panel (c) with $\alpha = 0.4$ and $a = 0.2$ and panel(d) with $\alpha = 0.6$ and $a = 0.2$), respectively. The grey shading gives the
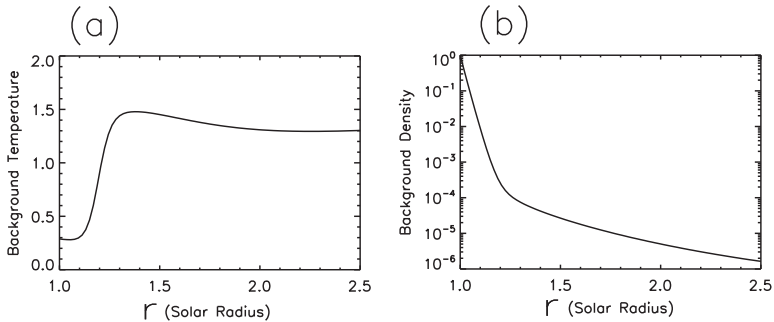
Figure 2.5: Background temperature (a) and density (b) as a function of radial coordinate in units of the solar radius. [*Ruan, et al.,* 2008]

reversal of the radial component of the magnetic field and the current sheet in the source surface. It is reasonable that the shape of the current sheet is smooth and located near the equatorial plane because it is expected in the solar minimum. But the thickness of the sheet is different between the models. Figure 2.8 shows the plasma density distribution (normalized by the density in the polar region) at the source surface. It is clear that the density is higher in the current sheet than in the two polar regions. From panel (a) of Figure 2.8, we can see the plasma density in the equatorial plane is twice as high as in the polar region. But in panel (b), the density in the equatorial plane is only 1.12 times as high as in the polar region. This difference is due to the different free parameter a in the model.

In Figure 2.7, the total current density increases with increasing α and a. This causes the pinching of the structure. It is important to remember that increasing a also enhances the field-aligned current density and therefore contributes to the narrowing of the structure. Because the plasma magnetic field structure is calculated self-consistently, stronger Lorentz force has to be balanced by a larger pressure gradient and a higher density. These effects can be seen clearly in the figures.

Comparison with the Bogdan-Low-model. [*Gibson and Bagenal,* 1995] applied the Bogdan-Low-model to a study of the plasma distribution in a dipole field case in the corona. They are successful in constructing the plasma distribution in the corona, especially in the streamer belts, when the corona is approximately longitudinally symmetric. The authors also point out the difficulty applying the Bogdan-Low model directly to data, i.e., using measured photospheric magnetic field directly as boundary conditions (by a spherical harmonic decomposition) is not compatible with a realistic density structure. The problem existed already for solar minimum configurations, but became more severe in the solar activity maximum. The authors find a way around this problem by allowing deviations in the measured and modeled photospheric magnetic field. The resulting configuration describes the large-scale structure reasonable well, but was not able represent structures below a resolution of one tenth of a solar radius.

The Bogdan-Low-model has been extended by [*Zhao and Hoeksema,* 1994] towards
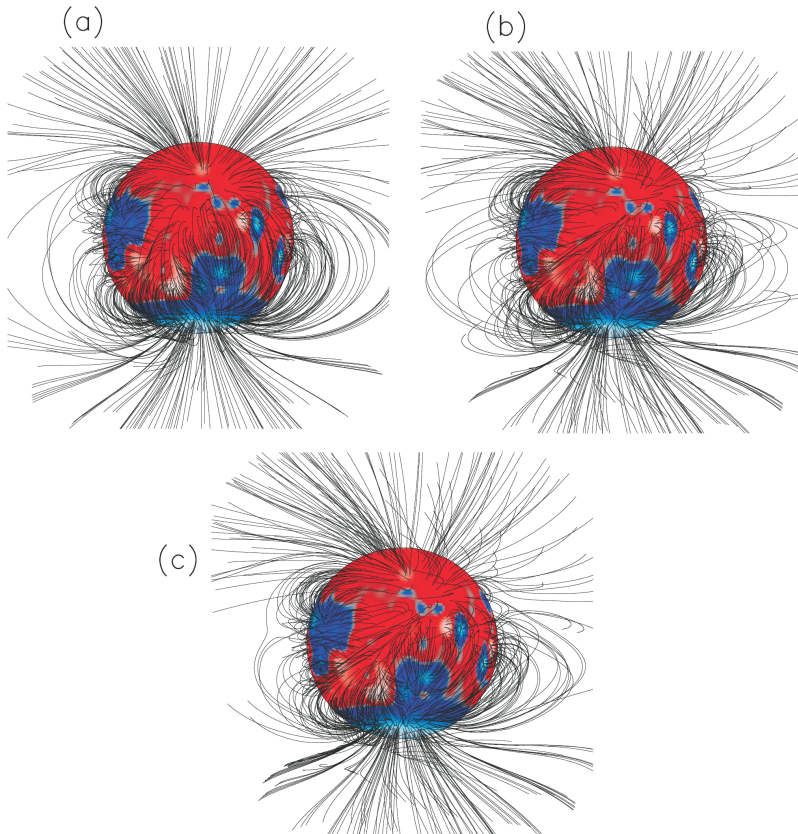
Figure 2.6: Magnetic field lines in the corona for Carrington rotation 1919 from different models: (a): potential field model, (b): LFFF model with $\alpha = 0.4$, (c): MHS model with $\alpha = 0.4$ and $a = 0.2$. [*Ruan, et al.,* 2008]
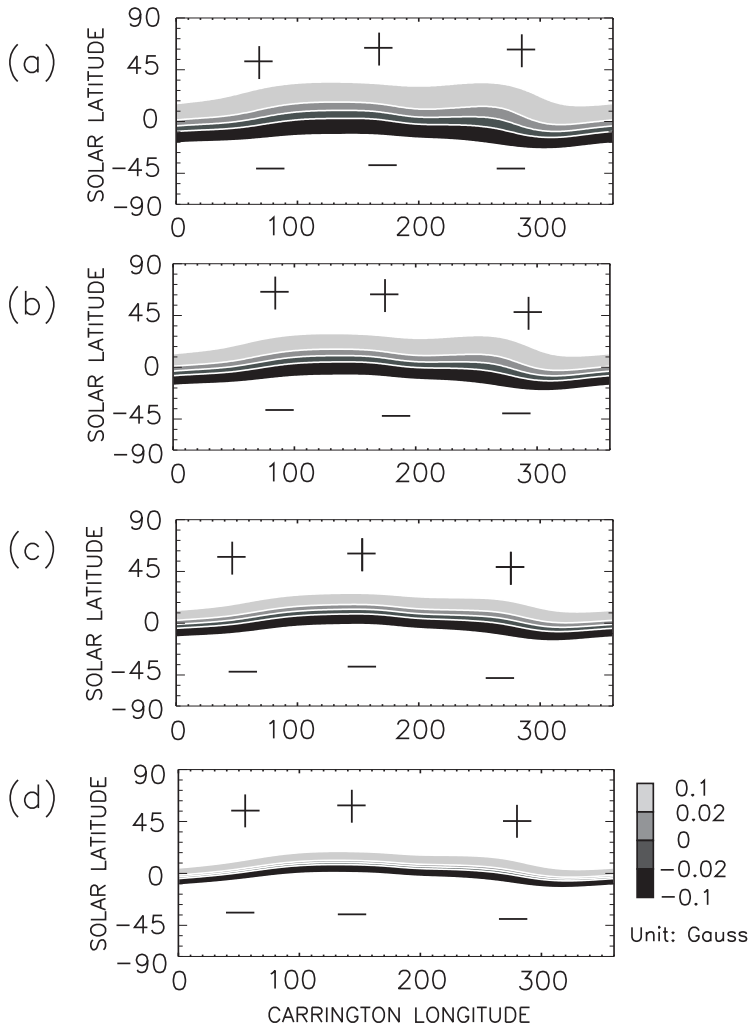
Figure 2.7: Current sheet in the source surface from different models: (a) the potential field model with $\alpha = 0$ and $a = 0$, (b) the LFFF model with $\alpha = 0.4$ and $a = 0$, (c) the MHS model with $\alpha = 0.4$ and $a = 0.2$, (d) the MHS model with $\alpha = 0.6$ and $a = 0.2$. [*Ruan, et al.,* 2008]
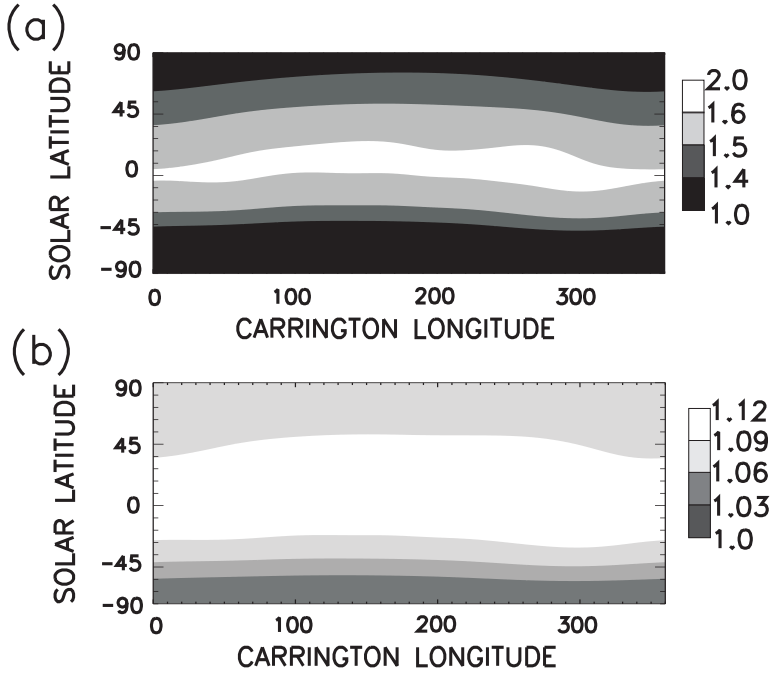
Figure 2.8: The density distribution at the source surface (the panel (a) with $\alpha = 0.4$ and $a = 0.2$ and the panel (b) with $\alpha = 0.4$ and $a = 0.05$). [*Ruan, et al.,* 2008]

the inclusion of helmet streamer currents. It was demonstrated that this extension allows better modeling of polar plumes and the axes of coronal streamers. *Gibson, et al.,* [1996] then applied this extended model to photospheric magnetograms. Compared to their earlier work, the extended model contains an equatorial current sheet, as well as current sheets between open and closed field regions, as boundary conditions. This allows the modeling of the observed sharp gradients across the boundaries of helmet streamers.

The N95 model is the generalization of the Bogdan-Low model to the regime $\alpha \neq 0$. This model has been applied by [*Zhao, et al.,* 2000] to model the magnetic field structure for polar crown SXR arcades by fitting the free parameters in the N95 model. The authors concentrated mainly on the local configuration over the southern polarity reversal line. Within this paper we applied this more advanced model to constructing the global magnetic field and the plasma in the corona. Our method is also different from that of [*Gibson and Bagenal,* 1995]. We start from the magnetogram in the photosphere, whereas [*Gibson and Bagenal,* 1995] use white-light data as primary input for their model.

In the linear force-free case, the current density has the form $\mu_0 \mathbf{j} = \alpha \mathbf{B}$. This is only applicable in the low β case, such as in the low solar corona where the plasma pressure is

much lower than the magnetic pressure. In that case we cannot derive any information of the plasma from the model. In this MHS model, there are two components of the current: the pure field-aligned part and the spherical shell part (Figure 2.3). They are represented by the first and the second terms in the right side of Eq. 2.41, respectively. Please note that the spherical shell part of the current density also contains a varying component parallel to the field lines, dependent on the local direction of the magnetic field. The main difference between the linear force-free model and the MHS model is the term $\varepsilon(r)\nabla(\mathbf{r} \cdot \mathbf{B}) \times \mathbf{r}$. This component of the current will produce a Lorentz force that will balance the pressure gradient and the gravity force. Consequently, not only the magnetic field but also the plasma will be constructed from this MHS model self-consistently. These α and a are two free parameters in the model (Eq. 2.38). Different free parameters will generate different distributions of the magnetic field and the plasma in the corona. The parameter α is the ratio of the parallel current component to the magnetic field. If α is too large, the magnetic field lines in the corona will become very twisted, which is unreasonable. We vary α from 0 to 0.6. The parameter a represents the perturbation by finite Lorentz force. If a is zero, it is the force-free case and there is no perturbation. When a increases, the perturbation increases. In Figure 2.8, the difference in the density between the polar region and the equatorial plane is greater with a higher value of a. It shows that a larger a generates a stronger perturbation in the model. But we cannot specify a a too large value, because in that case the perturbation is too large and it is impossible to put a reasonable background density to compensate for the perturbation.

Influence of free model parameters. The comparison between the different models (Figure 2.6) reveals that the field lines in the polar cap are similar. This is reasonable because the magnetic field in the polar cap at solar activity minimum should be close to potential. In the low-latitude part in the corona, different models give different results. From Figure 2.7, we find that the current sheet in the source surface from different models is very smooth and located close to the equatorial plane. But the thickness of the sheet is different between different models. The current sheet from the MHS model is thinner than the other two models. This should be due to the second component of the current: $\varepsilon(r)\nabla(\mathbf{r} \cdot \mathbf{B}) \times \mathbf{r}$. This term will change the magnetic field distribution in the source surface from the LFFF model, and it reduces the scale of the current sheet. If we keep a constant and increase α from 0.4 to 0.6, it is clear that the thickness of the current sheet also decreases (panel (c) and (d) in Figure 2.7). It means that field-aligned current can also reduce the scale of the current sheet on the source surface. Since the MHS model can construct not only the magnetic field but also the plasma in the corona self-consistently, we show the density distribution on the source surface in Figure 2.8. From the figure, it is obvious that the density is higher in the equatorial plane than in the two polar regions. This is consistent with the field-line distribution in panel (c) in Figure 2.6. In the equatorial plane, there are many closed field lines that confine the plasma. But in the polar regions, the plasma can escape into the solar wind along the open field lines, so it is reasonable that our MHS model with a current sheet has a higher density in the equatorial plane. It is not obvious from the N95 model equations that the density is reduced in the polar regions and enhanced at the equator.

We also applied our model to the solar activity maximum. The result is not as successful as in the solar minimum. There may be several reasons for this:

- The boundary condition is the photospheric magnetogram synoptic chart. This

means we assume that there are no intense changes in the photospheric field during the rotation of the sun, but active regions may evolve significantly over one solar rotation.

- Another even more important reason may be that, during solar maximum, the solar corona shows a lot more small-scale structures, which are difficult to model with a global linear solution such as ours.

Another issue is the first term in Eq. 2.70. Because the strongest density perturbation always appears in the active regions in the low corona, we have to apply a very high background density to compensate for the perturbation in the low corona. This will bring us an unreasonable density distribution in the low corona. But this does not mean the magnetic field distribution in the low corona is not correct. In our MHS model, we cannot totally avoid the noise. Because the plasma β in the low corona is very low, a small angle between the magnetic field line and the current line will produce a very large Lorentz force, which is very hard to be balanced by the plasma.

To summarize, we applied the Neukirch 95 magnetohydrostatic model to reconstructing the magnetic field and the plasma in the solar corona self-consistently with the synoptic photospheric magnetic field observation as the boundary condition. While the overall large-scale magnetic field structure is described reasonably well, we encountered some problems regarding the fine structure of the observed photospheric magnetic field being inconsistent with the density distribution under the limitations of the Neukirch 95 model. This problem has already been encountered by [*Gibson and Bagenal,* 1995] who used the simpler Bogdan-Low-model. The additional free parameter α in the Neukirch-model allows a greater variability of possible configurations, but varying α does not resolve this problem. In general this is to be expected since the models are linear and derive their structure from line-of-sight photospheric magnetic field measurements alone. Since the small-scale coronal structures are likely to be caused by nonlinear effects, further improvements, such as the use of vector magnetograph data, may be necessary to model these structures appropriately. Though there are some insufficiencies in this MHS model, the distribution of not only the magnetic field but also the plasma in the solar corona can be constructed from this MHS model in a self-consistent way.

3 Observations of the HCS, CIRs, ICMEs and a flux rope in the solar wind

The Minimum Variance Analysis (MVA) has been widely used to study magnetic structures in space, like a current sheet or a flux rope. The mathematical details of the MVA are introduced first in this chapter [*Sonnerup and Scheible,* 1998]. Next we show in situ observations of the Heliospheric Current Sheet (HCS), Corotating Interaction Regions (CIRs), Coronal Mass Ejections (CMEs), which have not been presented before. The detailed observations of a flux rope in the solar wind are described and discussed in the end of this chapter [*Ruan et al,* 2009].

3.1 Minimum Variance Analysis (MVA)

The Minimum Variance Analysis (MVA) is a useful tool to study in situ data in space physics [*Sonnerup and Scheible,* 1998]. The main purpose of the MVA is to find the normal direction of one dimensional current layer or other magnetic structures. Some mathematic details can be found in the appendix. The method is based on an idealized one dimensional model,

$$\partial/\partial x = 0, \tag{3.1}$$

$$\partial/\partial y = 0. \tag{3.2}$$

From this, we can get

$$\nabla \cdot \mathbf{B} = \partial B_z/\partial z = 0. \tag{3.3}$$

It means B_z is independent of z. Here (x, y, z) is a local cartesian coordinate system, and $\mathbf{B}$ is the magnetic field. Let's say $\hat{n}$ is the normal direction of a layer. $\mathbf{B}^{(1)}$, $\mathbf{B}^{(2)}$, and $\mathbf{B}^{(3)}$ are the measurements of the magnetic field. $\mathbf{B}^{(1)}$ and $\mathbf{B}^{(3)}$ would be measured on opposite sides of the layer, and $\mathbf{B}^{(2)}$ would be measured near the middle of the layer. So we have

$$\mathbf{B}^{(1)} \cdot \hat{n} = \mathbf{B}^{(2)} \cdot \hat{n} = \mathbf{B}^{(3)} \cdot \hat{n}. \tag{3.4}$$

Therefore the vectors $(\mathbf{B}^{(1)} - \mathbf{B}^{(2)})$ and $(\mathbf{B}^{(2)} - \mathbf{B}^{(3)})$ are tangential to the layer. The normal direction can be determined like this

$$\hat{n} = \pm \frac{(\mathbf{B}^{(1)} - \mathbf{B}^{(2)}) \times (\mathbf{B}^{(2)} - \mathbf{B}^{(3)})}{|(\mathbf{B}^{(1)} - \mathbf{B}^{(2)}) \times (\mathbf{B}^{(2)} - \mathbf{B}^{(3)})|}. \tag{3.5}$$

We have assumed that the magnetic field is time independent during the crossing of the structure by the spacecraft.

In real situation, magnetometer experiments can obtain many vector measurements, $\mathbf{B}^{(m)}$ (m=1, 2, 3,...M), during a traversal. As the estimate of $\hat{n}$, the MVA identifies in space the direction along which the magnetic field component set $\{\mathbf{B}^{(m)} \cdot \hat{n}\}$ (m=1, 2, 3,...M) has the minimum variance. So $\hat{n}$ can be determined by minimizing

$$\sigma^2 = \frac{1}{M} \sum_{m=1}^{M} |\, (\mathbf{B}^{(m)} - \langle \mathbf{B} \rangle) \cdot \hat{n} \,|^2 \tag{3.6}$$

where the average $\langle \mathbf{B} \rangle$ is defined by

$$\langle \mathbf{B} \rangle = \frac{1}{M} \sum_{m=1}^{M} \mathbf{B}^{(m)}.$$

Therefore σ^2 is a function of $\hat{n}$ or (n_X, n_Y, n_Z), where (n_X, n_Y, n_Z) is the three components of $\hat{n}$. The constraint is $\hat{n}^2 = 1$. So the question is to find the extremum of σ^2 with the condition of $\hat{n}^2 = 1$. By using a Lagrange multiplier λ, we can seek the solution of the following three linear equations

$$\frac{\partial}{\partial n_X} \left(\sigma^2 - \lambda(\hat{n}^2 - 1) \right) = 0, \tag{3.7}$$

$$\frac{\partial}{\partial n_Y} \left(\sigma^2 - \lambda(\hat{n}^2 - 1) \right) = 0, \tag{3.8}$$

$$\frac{\partial}{\partial n_Z} \left(\sigma^2 - \lambda(\hat{n}^2 - 1) \right) = 0, \tag{3.9}$$

These three equations can result in a matrix form as

$$\begin{pmatrix} \langle B_1 B_1 \rangle - \langle B_1 \rangle \langle B_1 \rangle & \langle B_1 B_2 \rangle - \langle B_1 \rangle \langle B_2 \rangle & \langle B_1 B_3 \rangle - \langle B_1 \rangle \langle B_3 \rangle \\ \langle B_2 B_1 \rangle - \langle B_2 \rangle \langle B_1 \rangle & \langle B_2 B_2 \rangle - \langle B_2 \rangle \langle B_2 \rangle & \langle B_2 B_3 \rangle - \langle B_2 \rangle \langle B_3 \rangle \\ \langle B_3 B_1 \rangle - \langle B_3 \rangle \langle B_1 \rangle & \langle B_3 B_2 \rangle - \langle B_3 \rangle \langle B_2 \rangle & \langle B_3 B_3 \rangle - \langle B_3 \rangle \langle B_3 \rangle \end{pmatrix} \begin{pmatrix} n_X \\ n_Y \\ n_Z \end{pmatrix} = \lambda \begin{pmatrix} n_X \\ n_Y \\ n_Z \end{pmatrix} \tag{3.10}$$

The subscripts $1, 2, 3$ denote three cartesian components, like in Geocentric Solar Ecliptic (GSE) or Geocentric Solar Magnetospheric (GSM) coordinate system, along which the magnetic field is measured. We should not confuse these three cartesian components denoted by 1, 2, 3 with (n_X, n_Y, n_Z), which is not yet known so far. By solving this matrix equation, we can get three eigenvalues $\lambda_1, \lambda_2, \lambda_3$ in order of decreasing magnitude and corresponding eigenvectors $\mathbf{x}_1, \mathbf{x}_2, \mathbf{x}_3$. Since the matrix is symmetric, the eigenvalues are all real and the corresponding eigenvectors are orthogonal. For the simplicity, we define $M_{\mu\nu}$ ($\mu\nu = 1, 2, 3$) as the matrix above.

If we multiply both sides of Eq. 3.10 with (n_X, n_Y, n_Z) from the left direction and reverse two sides of the equation, we can obtain

$$\lambda = \sum_{\mu\nu} n_\mu M_{\mu\nu} n_\nu. \tag{3.11}$$

Following Eq. 3.6, we can write

$$\sigma^2 = \sum_{\mu\nu} n_\mu M_{\mu\nu} n_\nu. \tag{3.12}$$

By comparing Eqs. 3.11 and 3.12, σ^2 will reach maximum, intermediate and minimum respectively if λ reaches the same stage. The corresponding three orthogonal eigenvectors represent the directions of maximum, intermediate and minimum variance of the magnetic field component.

Specifically, from Eq. 3.6, $\mathbf{x}_1$ means that the $\mathbf{x}_1$ component of the magnetic field will change maximum along the trajectory of the spacecraft, and the $\mathbf{x}_2$ and $\mathbf{x}_3$ components of the magnetic field will change intermediate and minimum respectively along the trajectory. We should not lead to a similar but wrong understanding that $\mathbf{x}_1$ means that the magnetic field magnitude changes maximum along the decomposed $\mathbf{x}_1$ direction of the spacecraft trajectory, and changes intermediate along the decomposed $\mathbf{x}_2$ direction of the spacecraft trajectory, and finally changes minimum along the decomposed $\mathbf{x}_3$ direction of the spacecraft trajectory.

In the latter part of this chapter, we will apply the MVA to analyze a flux rope in the solar wind to obtain three directions for this magnetic structure.

3.2 Parker Spiral and Heliospheric Current Sheet (HCS)

3.2.1 Formation of the Parker spiral

The current sheet in the center of helmet streamers in the solar corona extends by the deformation of the solar wind into the heliospheric current sheet (HCS). The bottom panel of Figure 3.1 provides the geometry of a radially expanding solar wind with a radial magnetic field [*Meyer-Vernet*, 2007]. Since the magnetic Reynolds number is very large, the plasma is frozen in with the magnetic field in the heliospheric space. The magnetic field lines will be dragged into the space radially by the outflowing plasma, the solar wind, if the Sun is not rotating.

However, there is a complication to this picture that the Sun is rotating. The top panel of Figure 3.1 provides the geometry of the real situation, which considered the solar angular velocity Ω. A fixed source on the rotating Sun is initially at point A. This source A will eject plasma radially out to space with the radial velocity V_w. In the same time, as the ejected plasma travels along the arrow starting from A, the Sun rotates, so the Sun ejects the other following plasma from different locations. The arrows indicate the ejection of these following plasma parcels. When the plasma ejected at A reaches A′, the plasma ejected later have less time to travel, and are therefore closer to the Sun and along different arrows. However the magnetic field lines show different situation. Since the magnetic field lines are not broken in space, these field lines will connect the Sun to the space. It means with the rotation of the Sun, a field line will connect the point A′ in space and C on the Sun's surface.

Let's assume $\triangle t$ is the traveling time for the plasma that started at A to reach A′. So in $\triangle t$, the Sun has rotated by an angle $\triangle \phi$. From this we get

$$\triangle \phi = \Omega \triangle t, \tag{3.13}$$

$$\triangle r = -V_w \triangle t \tag{3.14}$$

where Ω is the solar angular velocity as defined above, $\triangle r$ the distance between A and A′, V_w the radial velocity of the solar wind. Dividing Eq. 3.14 by Eq. 3.13, the following equation is obtained

$$d\phi/dr = -\Omega/V_w \tag{3.15}$$

Since by definition **B** is along the field lines, its radial and azimuthal components satisfy $B_\phi/B_r = rd\phi/dr$ in the equatorial plane, so with replacing $d\phi/dr$ from Eq. 3.15 we reach

$$B_\phi/B_r = -\Omega r/V_w. \tag{3.16}$$

We plot the magnetic field lines in the equatorial plane in Figure 3.2, which follow Parker's spiral [*Meyer-Vernet*, 2007]. With the increasing distance r, the ratio of B_ϕ/B_r is becoming increasing. The magnetic field inclination to the radial direction is about 25-45° at 1 AU, but increases to nearly 90° beyond 10 AU, so that at large distances the field lines almost follow circles around the Sun. Outside the equatorial plane at a heliospheric latitude θ, the field lines satisfy $B_\phi/B_r = r\cos\theta d\phi/dr$. From this and Eq. 3.15, we get

$$B_\phi/B_r = -\Omega r \cos\theta/V_w. \tag{3.17}$$

In this ideal case, there is no B_θ component both in the equatorial plane and outside the equatorial plane.

However, the solar rotation axis Ω is not aligned with the magnetic axis M. Let us assume a small angle α in between. Without losing the generality, we can assume that the projection of the M in the XY plane is along the negative Y direction. (See Figure 3.3 which is adjusted from [*Meyer-Vernet*, 2007]. For the simplicity, we did not plot this projection.) Let us assume the coordinate of a fixed point on the magnetic equator, which is also the current sheet, is $(\theta_\circ, \phi_\circ)$ in the Sun's surface in the coordinate system of $XY\Omega$. As a result, the latitude $\theta_\circ$ of a certain point on the solar magnetic equator varies with the azimuthal angle $\phi_\circ$ as $\sin\theta_\circ = \sin\alpha\sin\phi_\circ$ from this geometry (Figure 3.3). (Though this equation is not straightforward, it can be easily checked by setting $\phi_\circ = 0°, 90°, 180°, 270°$.) As the Sun rotates, this yields

$$\sin\theta_\circ = \sin\alpha\sin(\phi_\circ - \Omega t) \tag{3.18}$$

so that the fixed point on the magnetic equator is alternately above and below the rotational equator with time. The magnetic equator gives the position of the current sheet close to the Sun, before being drawn outwards by the solar wind flow.

The plasma flow transforms the initial angular coordinates (θ_1, ϕ_1) on the Sun's surface into the value (θ_2, ϕ_2) at a large r given by

$$\theta_2 = \theta_1, \tag{3.19}$$
$$\phi_2 = \phi_1 - \Omega r/V_w \tag{3.20}$$

The magnetic equator in the Sun's surface will be transformed into the heliospheric space by flows. By considering Eqs. 3.18, 3.19 and 3.20, the heliospheric current sheet is a surface

$$\sin\theta = \sin\alpha\sin(\phi - \Omega r/V_w - \Omega t). \tag{3.21}$$

We ignored the footnotes for the simplicity. If the inclination angle α between $\mathbf{M}$ and $\mathbf{\Omega}$ is very small, θ should be also very small. So we got $\sin\alpha \approx \alpha$ and $\sin\theta \approx \theta$. So Eq. 3.21 becomes

$$\theta = \alpha \sin(\phi - \Omega r / V_w - \Omega t). \tag{3.22}$$

This equation represents a surface whose intersection with the rotational equatorial plane $(\theta = 0)$ is an Archimedean spiral rotating at angular speed Ω. The intersection with a meridian plane $(\phi = constant)$ is a warped shape, varying in time at the frequency Ω and in distance at the wavelength $2\pi V_w / \Omega$. The artist plotting of the HCS has been shown in Figure 1.8.

3.2.2   In situ observations of the HCS

As we know, the Sun finishes one self rotation in 27 days. It means that the spacecraft STEREO should cross the HCS twice in 27 days. The HCS is a large structure in the solar wind, which is a typical character differ the HCS from the local current sheet in the solar wind. Figure 3.4 shows the in situ observations of two crossings of the HCS. The B_x, B_y and B_z components of the magnetic field in GSE are shown in the top three panels. The polar angle Θ and the azimuth angle Φ are shown in the bottom two panels. The two black lines through all panels mark two crossings of the HCS. The azimuth angle Φ_B is around 180° before the first crossing, which means the magnetic field direction is away from the Sun, and changes to around 0° or 360° after the first crossing, which means the magnetic field direction is towards the Sun. (0° and 360° are in the same direction.) The magnetic field direction changes back during the second crossing. These two reversals of the magnetic field cannot be explained by a local current sheet, which is a much smaller structure compared to the HCS. The fluctuations of the magnetic field during the crossing is intense. [*Behanonn et al.,* 1983] found the fine structures in the HCS, which ripple and superimpose on the large-scale warped HCS.

   Since Figure 3.4 gives the observations for 30 days, the details of the crossings and the exact center of the HCS cannot be studied here. *Gosling et al.* [2006A, 2006B] have found clear evidence of magnetic reconnection inside the HCS. So if the multiple-X-line magnetic reconnection can happen inside the HCS, the HCS will provide an appropriate environment to generate a flux rope. The later part of this thesis will show another HCS crossing with detailed observations, and discuss how magnetic reconnection generates the flux rope.

3.3   Corotating Interaction Regions (CIRs) and Interplanetary Coronal Mass Ejections (ICMEs)

Figure 3.5 shows typical observations of a CIR at 1 AU by STEREO A. The top two panels are the fluxes of the energetic protons and helium, respectively. The lines with different colors represent different energies. The third, forth, and fifth panels show the proton number density, the fluid velocity and the temperature of the solar wind. The bottom panel shows the magnitude of the magnetic field in the solar wind. The time period for
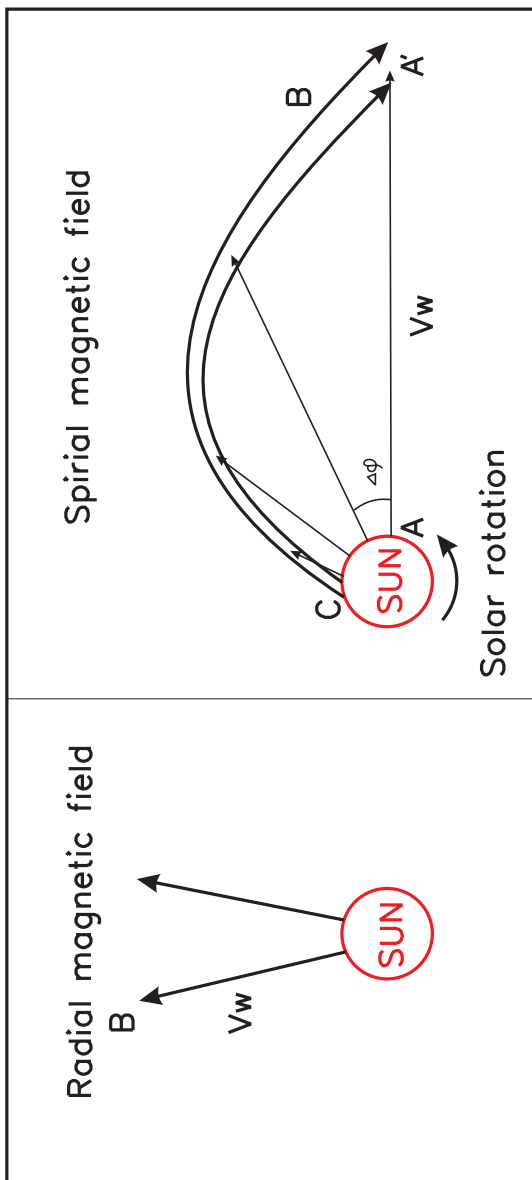
Figure 3.1: Magnetic field lines dragged by the radially expanding solar wind into the heliospheric space, adjusted from [*Meyer-Vernet*, 2007]
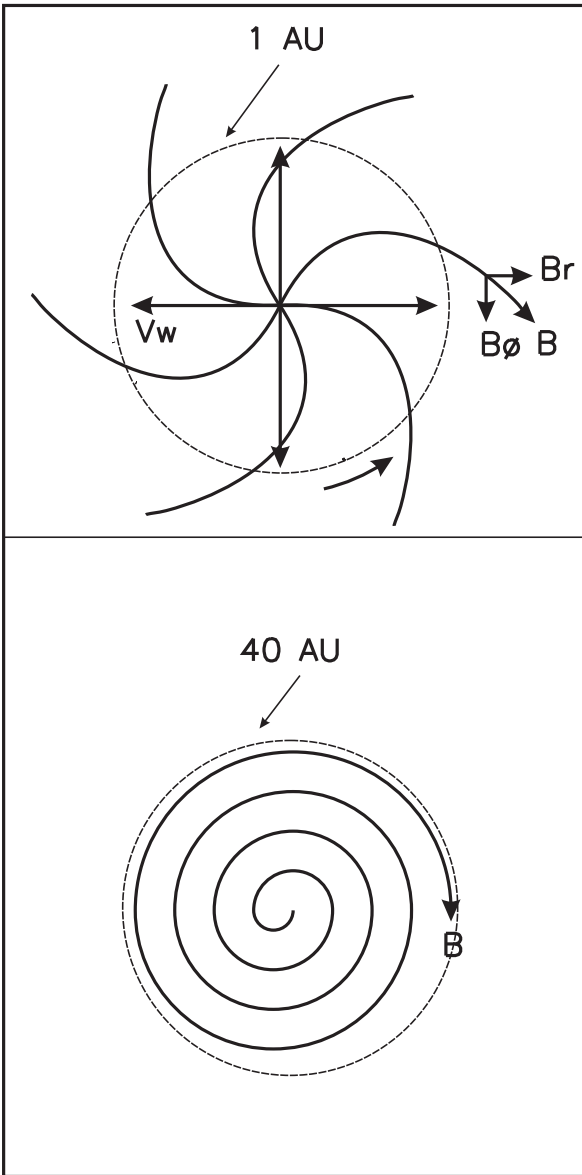
Figure 3.2: Spiral magnetic field lines in the solar wind in the equatorial plane, adjusted from [*Meyer-Vernet*, 2007]
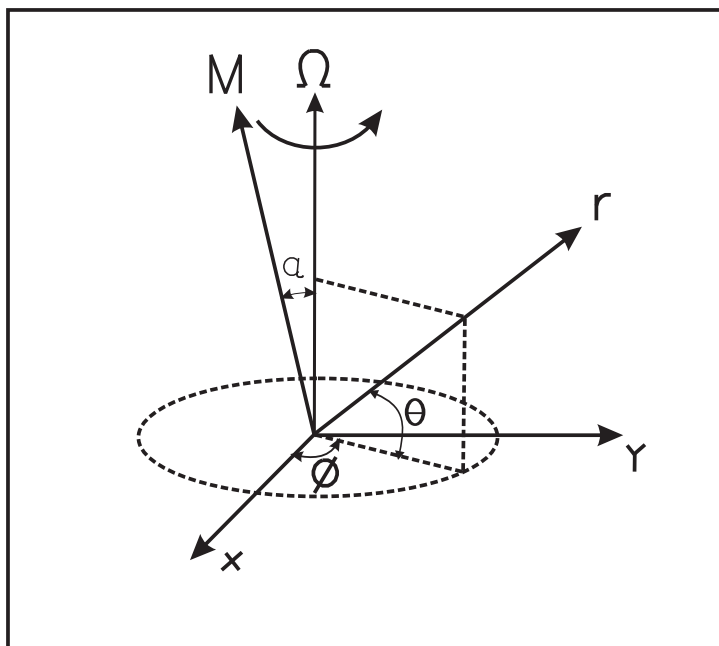
Figure 3.3: Tilted magnetic axis *M* of the Sun to the rotation axis Ω, adjusted from [*Meyer-Vernet*, 2007]

these observations is from 11 to 26 in November 2007. The spacecraft observed two CIRs during this time period, which are highlighted by two red boxes. For the first CIR, the velocity of the solar wind is about 400 km/s on 13 November before the CIR. But it increased to 600 km/s on 14 November in the CIR. A compression region was generated between the fast and slow solar wind. Inside this compression region, the spacecraft observed a clear increase of the plasma density and temperature. The magnitude of the magnetic field also shows a clear increase. From the first and second panels, we can see the clear increase of the energetic particles following the compression region. All these observations are typical signatures of the CIR [summarized in *Crooker and Gosling,* 2007; *Kunow and Lee,* 2007; *Mason and Steiger,* 2007]. The second CIR shows the similar observations. These two CIRs are separated by about only 6 days.

The increase of the energetic particles is usually a typical signature of the CIRs [*Kunow and Lee,* 2007]. But not all these increases represent the CIRs. Between the two black lines in the figure, we also see a clear increase of the energetic particles. But we did not find the compression region between the fast and the slow solar wind. So these energetic particles are not caused by a CIR.
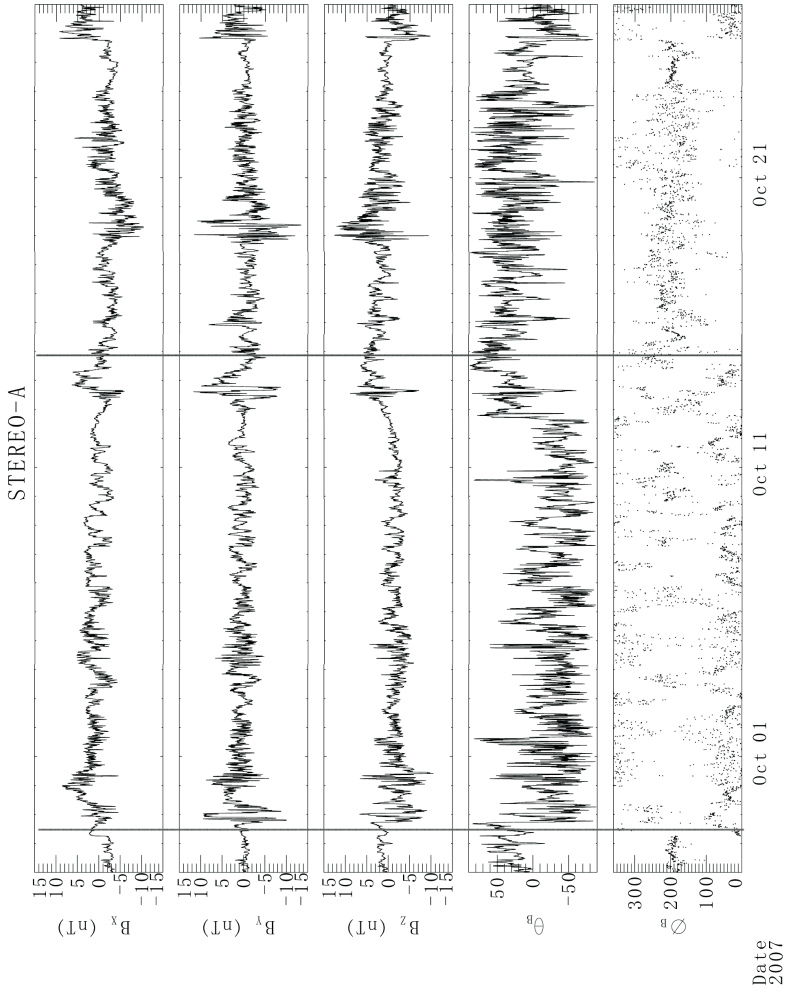
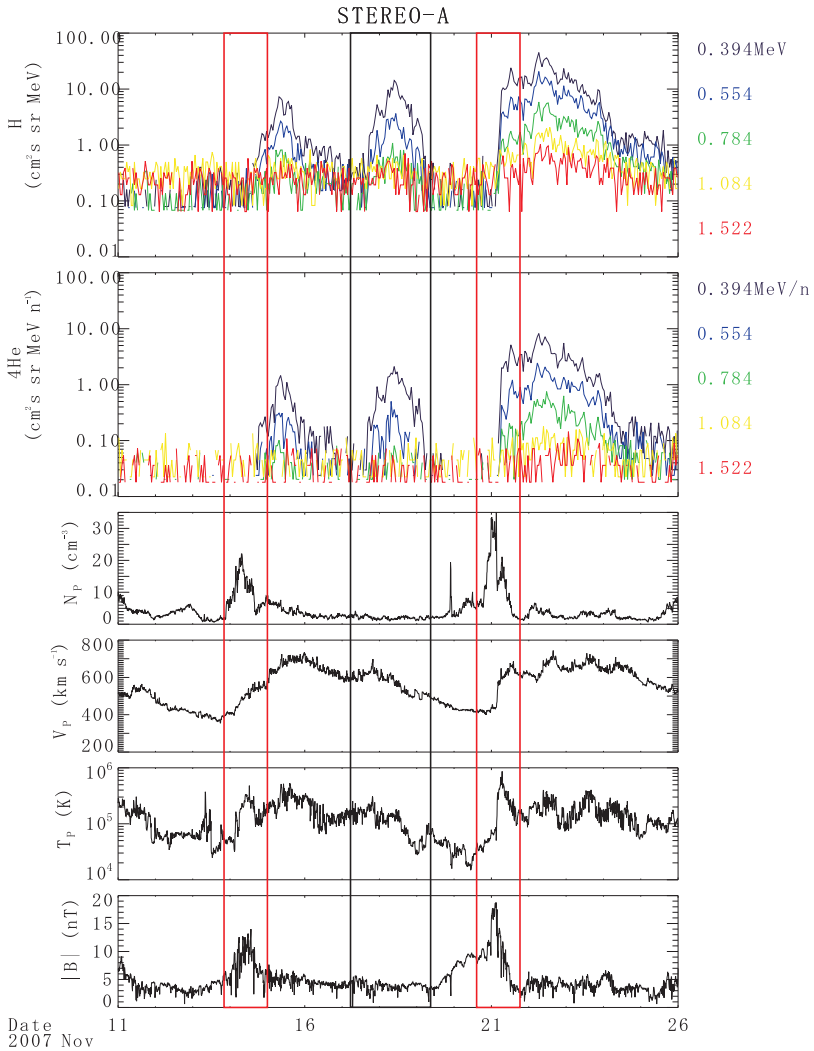Figure 3.4: In situ observations of the HCS in the solar wind.

Figure 3.5: In situ observations of two CIRs in the solar wind.

Figure 3.6 shows an ICME observed by STEREO B at 1 AU. The proton number density, the plasma temperature and solar wind velocity are shown in the top three panels. The bottom three panels show the magnetic field magnitude, the polar angle and the azimuth angle of the magnetic field in GSE. The time period for these observations is from 07:00UT on 23 Oct to 07:00UT on 24 Oct in 2007. The two black lines crossing all the panels mark the boundaries of the ICME. Inside the ICME, we can see the clear enhancement of the magnetic field strength. From the two bottom panels, we can see the rotation of the magnetic field direction through the changes of these two angles. They are typical signatures of the magnetic cloud [summarized in *Zurbuchen and Richardson,* 2007]. The first panel shows a clear depression of the plasma density from 17:00UT to 23:00UT on 23 Oct 2007, which is also a plasma signature to identify the magnetic cloud [*Zurbuchen and Richardson,* 2007]. From the third panel, we see an increase of the solar wind velocity from about 320 km/s before the ICME to 400 km/s in the ICME, which can be used here to identify the boundary between the ICME and the ambient solar wind.

Both the CIR and the ICME will show an increase of the solar wind velocity compared to the preceding ambient solar wind, and show the enhancement of the magnetic field strength inside. The CIR will show the enhancement of the plasma density and the temperature due to the compression between the fast solar wind and the slow solar wind, but the ICME usually, not always, shows the decrease of the plasma density and temperature inside the magnetic cloud. The rotation of the magnetic field direction is a typical magnetic signature of the magnetic cloud, by which one can clearly differ the ICME from the CIR [*Crooker and Gosling,* 2007; *Zurbuchen and Richardson,* 2007].

The time scale of the ICME is usually about several tens hours or several hours at least. This character clearly differs the ICME from the flux rope in the solar wind, whose time scale is usually less than one hour. The coming part of the thesis will show in situ observations of a CIR, an ICME, and a flux rope in the solar wind. The scale of the flux rope is much less than two others'.

3.4 Flux rope

Flux ropes are widely observed in the Earth's magnetosphere [*Russell and Elphic*, 1978], [*Elphic*, 1995], [*Slavin et al.*, 2003], [*Zong et al.*, 2004], the Jovian Magnetosphere [*Walker and Russell*, 1985], the Mercury's magnetosphere [*Russell and Walker*, 1985], and in the solar wind [*Moldwin et al.*, 2000] by in situ observations. Though individual-spacecraft observations suggested the flux rope could be an extended two-dimensional structure, multiple-spacecraft observations are still needed to confirm this. Regular in situ observations in the solar wind by the two STEREO A and B spacecraft now provide an opportunity to study the scale of flux ropes, which may be extended in the solar wind.

The multiple-X-line magnetic reconnection has been proposed to be responsible for the generation of the flux ropes in space [*Slavin et al.*, 2003]. Though the detailed physics of this dynamic process is still not clear, the possible topology of the process has been suggested for more than 20 years [*Lee and Fu*, 1985]. The scenarios of single-X-line and multiple-X-line reconnection are illustrated in Figure 3.7. The panels (1) and (2) display the single-X-line reconnection which occurs between the same colored magnetic field lines at **1, 2, 3** in the figure. So there is only one X line passing through **1-2-3**. Panel
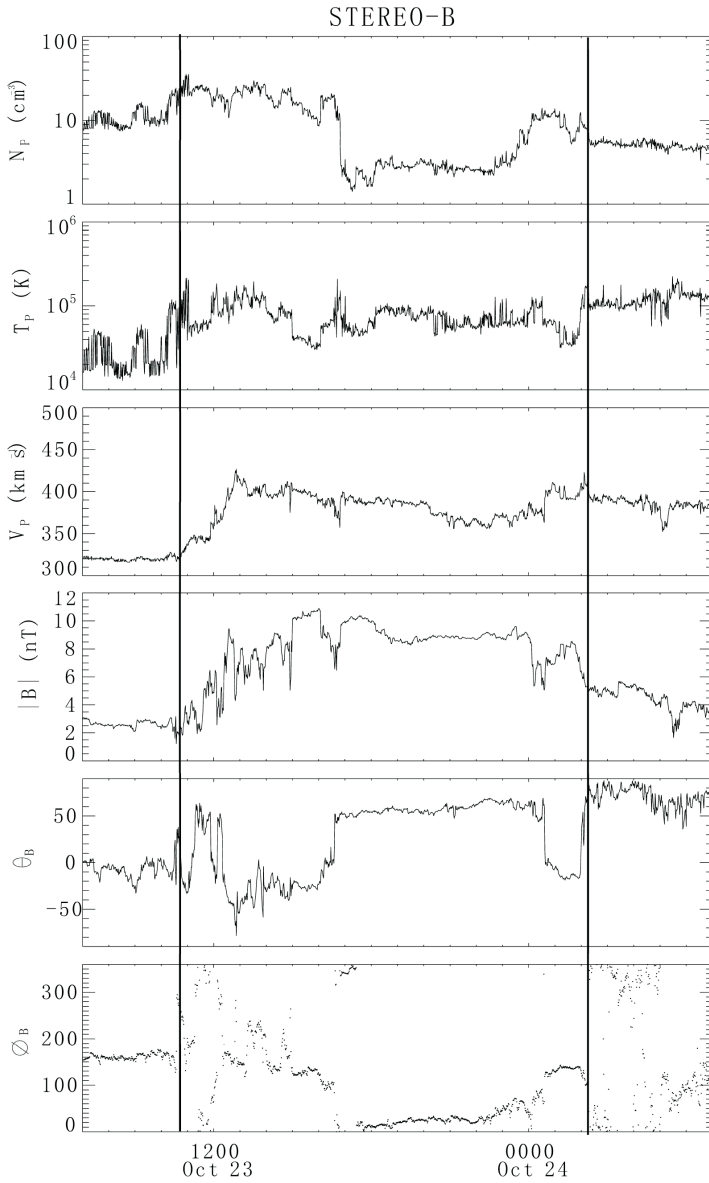
Figure 3.6: In situ observations of an ICME in the solar wind.
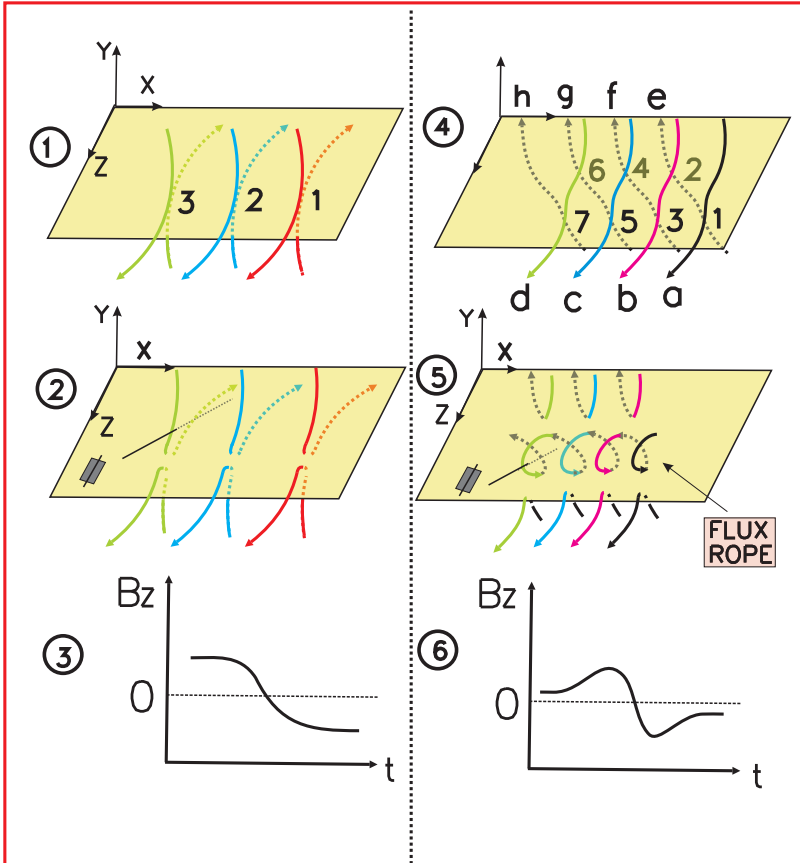
Figure 3.7: Illustration of the topology of the single-X-line magnetic reconnection (the left panel) and the multiple-X-line magnetic reconnection (the right panel).
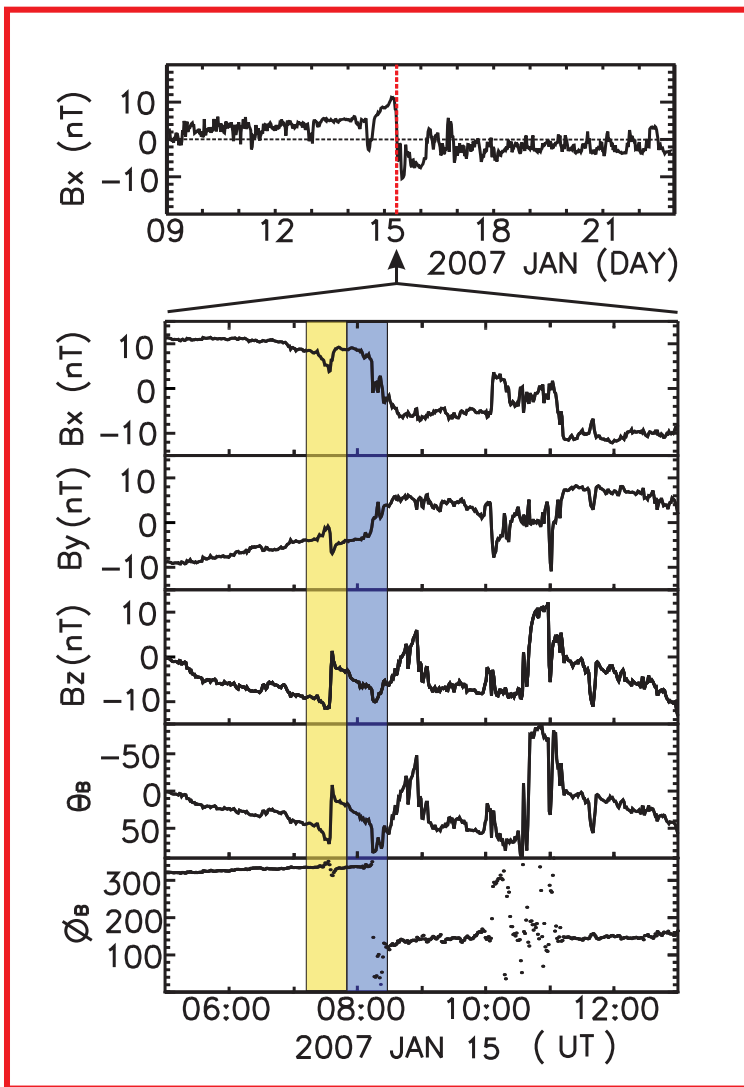
Figure 3.8: The figure shows the magnetic field parameters during the crossing of the flux rope and the HCS in the solar wind by STEREO A. The red dashed line in the top panel shows the reversal of the B_x component, which indicates the HCS. The yellow strip in the bottom panels highlights the flux rope. The blue strip highlights the crossing of the HCS [*Ruan et al*, 2009].

(3) shows the B_Z signature expected for this kind of reconnection. The panels (4) and (5) illustrate multiple-X-line reconnection which occurs between magnetic field lines **a** and **e** at **1**, **e** and **b** at **2**, **b** and **f** at **3**, **f** and **c** at **4**, **c** and **g** at **5**, **g** and **d** at **6**, **d** and **h** at **7**. Consequently, there are at least two X lines for this type of reconnection: one passing through **1-3-5-7**, the other through **2-4-6**. Panel (5) shows the product of multiple-X-line reconnection, called a flux rope. Panel (6) indicates the typical bipolar signature to be measured by a spacecraft crossing this flux rope. The main difference between these two types of reconnection is whether a shear component of magnetic field does exit. From panel (4), we can see there is a X component in such a topology, which is called the shear component in magnetic reconnection. (The coordinate system for this illutration is shown in panel (1).) From panel (1), there is no shear component for this type of reconnection. From these panels, we can see that the single-X-line reconnection cannot generate a flux rope, and that the magnetic field signature indicating the products from these two different reconnection mechanisms will be a little different. Panel (3) is also the signature of crossing a current sheet without magnetic reconnection.

The signature of magnetic reconnection has been found inside the heliospheric current sheet (HCS) [*Gosling et al.*, 2006A, 2006B], which raises the possibility that the flux ropes might be generated by reconnection in the solar wind. These observations seem to imply that the reconnection in the solar wind is in a steady state, with a single X-line on large scale [*Phan et al.*, 2006], [*Gosling et al.*, 2007A, 2007B].

We will describe observations from five spacecraft of a coherent structure in the solar wind. The analysis shows that this magnetic structure is a flux rope. This flux rope is embedded in a Corotating Interaction Region (CIR), which followed a magnetic cloud. The magnetic field data from five spacecraft provides a clear evidence that the flux rope is a quasi two-dimensional structure, elongated in its third nearly constant dimension. The diameter of the flux rope is much smaller than the magnetic cloud, which passes the spacecraft immediately before the flux rope. The possible signatures of the reconnection have also been found inside the flux rope.

3.4.1 Magnetic field and particle observations of a flux rope in the solar wind

We show and discuss the in situ observations from five different spacecraft. The GSE coordinates (in units of R_E) of the spacecraft are (218, -12, 22) for ACE, (249, -55, 18) for WIND, (259, -112, -39) for STEREO A, (103, -6, -17) for STEREO B, and (12, 14, -4) for CLUSTER 4 (C4) on 15 January 2007. They were all in the solar wind upstream of the Earth bowshock.

We present the magnetic field observations from STEREO A first [*Luhmann et al.*, 2008]. The top panel of Figure 3.8 shows the observation of the B_X component of the magnetic field in the GSE coordinate system by STEREO A from 09 January to 23 January in 2007. STEREO A caught the heliospheric current sheet (HCS) with the reversal of B_X on 15 January 2007. The other panels show observations from 05:00 UT to 13:00 UT on this day. The blue highlighted region shows the crossing of the HCS around 08:20 UT. From the B_X component and the angle Φ_B, we can see that the magnetic field changed its direction from towards the Sun to away from the Sun during the crossing. Before this, the B_Y component around 07:35 UT exhibited the bipolar signature indicating a special

magnetic structure, which we will identify as a flux rope. The yellow highlighted region shows the crossing of this flux rope. From the bottom panel, we can see that the angle Φ_B changed from $\sim 350°$ to $\sim 120°$ during the crossing of HCS. However during the crossing of the flux rope, the Φ_B shows only a little variation. These observations indicate that the flux rope is not embedded in the HCS, but detached from the current sheet.

Figure 3.9 is the artist plotting, which intends to explain the relative position between the HCS and the flux rope. The spacecraft touched the flux rope first and the HCS later. The strahl beam electrons are also shown in the figure, which will be discussed below.

The orientation of the flux rope was determined by a local Minimum Variance Analysis (MVA) from individual spacecraft observations and a timing analysis based on the joint observations of all five spacecraft, because by MVA alone one cannot determine the flux rope orientation [*Xiao et al.*, 2004]. (We did not apply a current MVA (CMVA), based on CLUSTER four-point data, to analyze the flux rope orientation, because the distances between the four CLUSTER spacecraft were too small compared to the flux rope size.) The magnetic field vector inferred from the five spacecraft is decomposed into the three directions, $\mathbf{L}_{FR}$ (0.17, -0.34, 0.92), $\mathbf{M}_{FR}$ (0.76, - 0.54, -0.34), and $\mathbf{N}_{FR}$ (0.61, 0.76, 0.16) based on the MVA of the ACE observations, and shown in Figure 3.10. For the MVA of the flux rope, we found that the eigenvalues obey $\lambda_L/\lambda_M \approx 10 \gg 1$ and $\lambda_M/\lambda_N \approx 10 \gg 1$ for all five spacecraft. This means that the MVA gives the maximum ($\mathbf{L}_{FR}$), intermediate ($\mathbf{M}_{FR}$) and minimum ($\mathbf{N}_{FR}$) variance directions of the magnetic field with high accuracy [*Sonnerup and Scheible*, 1998]. For all spacecraft the corresponding **LMN** coordinate axes are almost parallel. The $\mathbf{M}_{FR}$ direction, which we will identify as the flux rope orientation, is in GSE (0.76, -0.54, -0.34) for ACE, (0.73, -0.58, -0.35) for WIND, (0.88, -0.25, -0.39) for STEREO A and (0.74, -0.53, -0.41) for STEREO B, and finally (0.85, -0.43, -0.29) for CLUSTER (see the table below). (There is a little difference in the flux rope orientation from the STEREO A observation.)

Table 3.1: Flux rope orientation from five spacecraft.

spacecraft	$\mathbf{M}_{FR}$
ACE	(0.76, -0.54, -0.34)
WIND	(0.73, -0.58, -0.35)
STEREO A	(0.88, -0.25, -0.39)
STEREO B	(0.74, -0.53, -0.41)
CLUSTER	(0.85, -0.43, -0.29)

In Figure 3.10, the similarity of the magnetic field component variations observed by the five spacecraft with a time delay suggests an extended, quasi two-dimensional structure. The bipolar signatures of the magnetic field variations in $\mathbf{L}_{FR}$ direction are typical for a helical flux rope. (There is a small residual variation of B_N across the rope in the diagram of STEREO A and B, and CLUSTER. This is due to a decomposition of the magnetic field in the MVA system of the spacecraft ACE, which is slightly rotated with respect to the corresponding system of the other spacecraft.) The flux rope touched ACE, WIND, STEREO A, STEREO B and CLUSTER, consecutively. This timing of the multiple-spacecraft observations confirmed that the $\mathbf{M}_{FR}$ direction derived from the MVA defines the flux-rope orientation. If we had selected the $\mathbf{L}_{FR}$ or $\mathbf{N}_{FR}$ direction as principal orientation, this would not be consistent with the timing of these observations and the
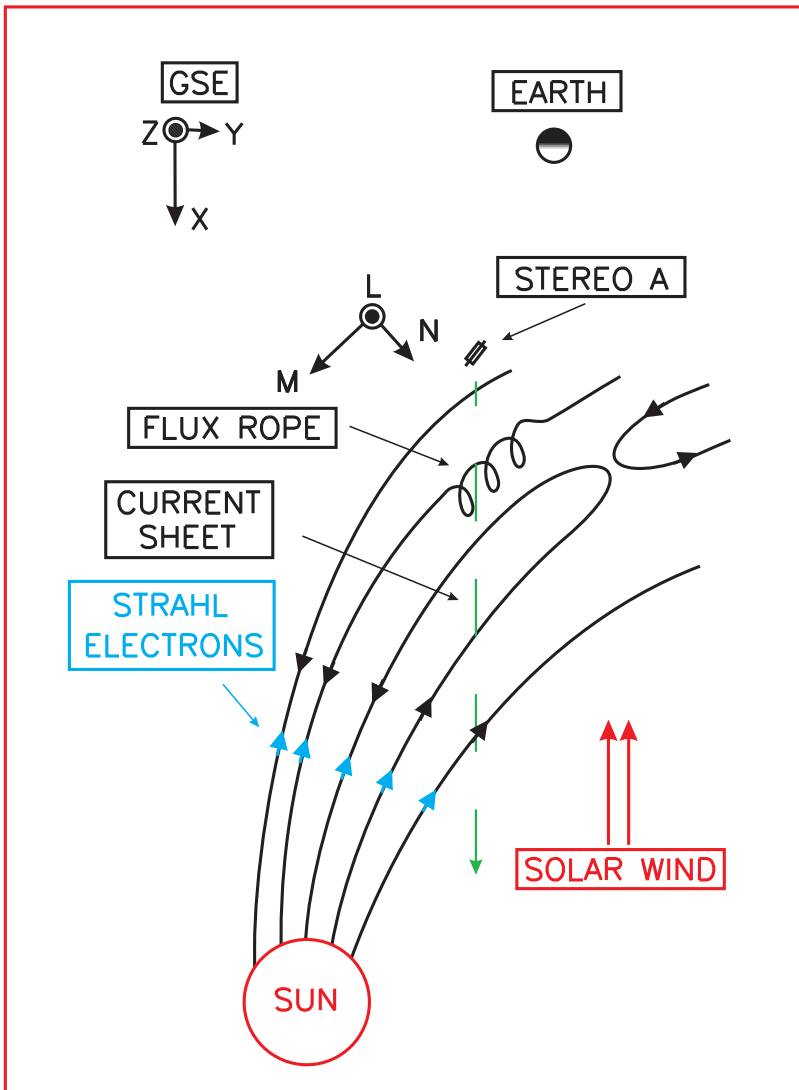
Figure 3.9: Sketch of the HCS and the flux rope in the solar wind.

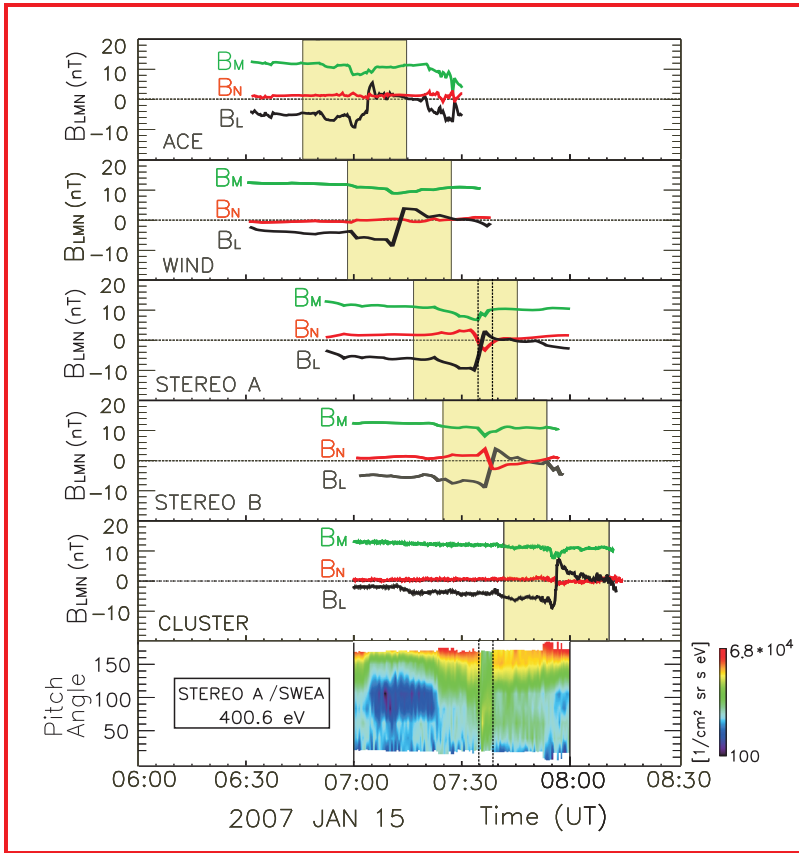Figure 3.10: The magnetic field signatures of the same flux rope observed by five space-craft consecutively. The top panels show the three magnetic field components measured by the five spacecraft in the **LMN** coordinate system of the ACE spacecraft. The bottom panel displays the pitch angle distribution (PAD) of electrons at 400.6 eV in the spacecraft frame from STEREO A [*Ruan et al*, 2009].

magnetic field signature inside the flux rope. With this main orientation of the flux rope, we obtain a length of the flux rope of 180 R_E, based on the distance between STEREO A and B.

The bottom panel of Figure 3.10 displays the pitch angle distribution (PAD) of electrons at 400.6 eV from STEREO A. The dashed black lines in the third and sixth panels are based only on the electron data, and mark the inferred boundaries of the flux rope core. Outside of the flux rope core, we can see strahl electrons antiparallel to the magnetic field, which indicate that one end of these field lines is still connected to the Sun. In the core, there is a clear drop of the strahl electrons.

Figure 3.11 shows an artist's concept of the flux rope as it is crossed consecutively by the five spacecraft. ACE and WIND are above the GSE X-Y plane (the yellow plane in the figure), but STEREO A and B are below the X-Y plane. Figure 3.12 shows the projection of the flux rope in the ecliptic plane. It can be seen from this figure that the flux rope will touch ACE, WIND, STEREO A, STEREO B and CLUSTER consecutively. The distances between the spacecraft are drawn to scale in these two figures.

Figure 3.13 displays the detailed observations from CLUSTER (C4). The sequence of panels from top to bottom in this figure shows several relevant plasma parameters: Panels **a** and **b** show the magnitude of the magnetic field and three components of the magnetic field in **LMN** coordinate system, versus time from 07:00 UT to 09:00 UT. Panels **c**, **d**, and **e** exhibit three components of the solar wind velocity in GSE. The velocity component in **L** direction in the solar wind frame is plotted in panel **f**. Panels **g, h, i, k, m, n** give the magnetic field, the flow velocity components in the solar wind frame, the proton density and the temperature versus time from 07:53 UT to 07:58 UT, respectively. The magnitude of the outflow velocity in the solar wind frame and the local Alfvén velocity versus time from 07:55 UT to 07:56 UT is plotted in panel **o**. Panel **p** shows the total pressure, including magnetic pressure and thermal pressure. (Since here the flux rope is a two-dimensional structure, we use B_M^2 instead of $|B|^2$ to calculate the magnetic gradient pressure [*Low*, 1990]. The particle thermal pressure includes the ion and electron pressure.) Here the magnetic field is decomposed into its three components with respect to the unit vectors in GSE, **L** (0.10, -0.41, 0.90), **M** (0.85, - 0.43, -0.29), and **N** (0.51, 0.80, 0.31), referring to the **LMN** directions derived from a MVA using the CLUSTER observation. The solar wind background velocity is 90 km/s in **L** direction, -240 km/s in **M** direction, -200 km/s in **N** direction, derived from the quiet time period with the smooth magnetic field and velocity variation before the flux rope.

The flux rope is embedded in a plasma flow pointing in the negative **L** direction (shown in the panel **f** of Figure 3.12)). At the rope core marked by the B_L reversal versus time from 07:55 to 07:56, the spacecraft instruments measured a hot flow accompanied with an increase in density and temperature. The magnitude of the flow velocity in the solar wind frame is close to the local Alfvén velocity (panel **o** of Figure 3.13). Since both magnetic field and particle data are consistent with the signatures of magnetic reconnection in the solar wind [*Gosling et al.*, 2005], these observations suggest magnetic reconnection might be responsible for the flux rope.

From panel **p** of Figure 3.13, we see that the total pressure is around 0.065 nPa before and after the flux rope core, but increased more than 20% to 0.08 nPa in the core. Based on the solar wind velocity from CLUSTER, the estimation of the flux rope diameter is $\sim$40 R_E or 2.5×10^5 km. The diameter of the flux rope core is $\sim$10 times smaller.
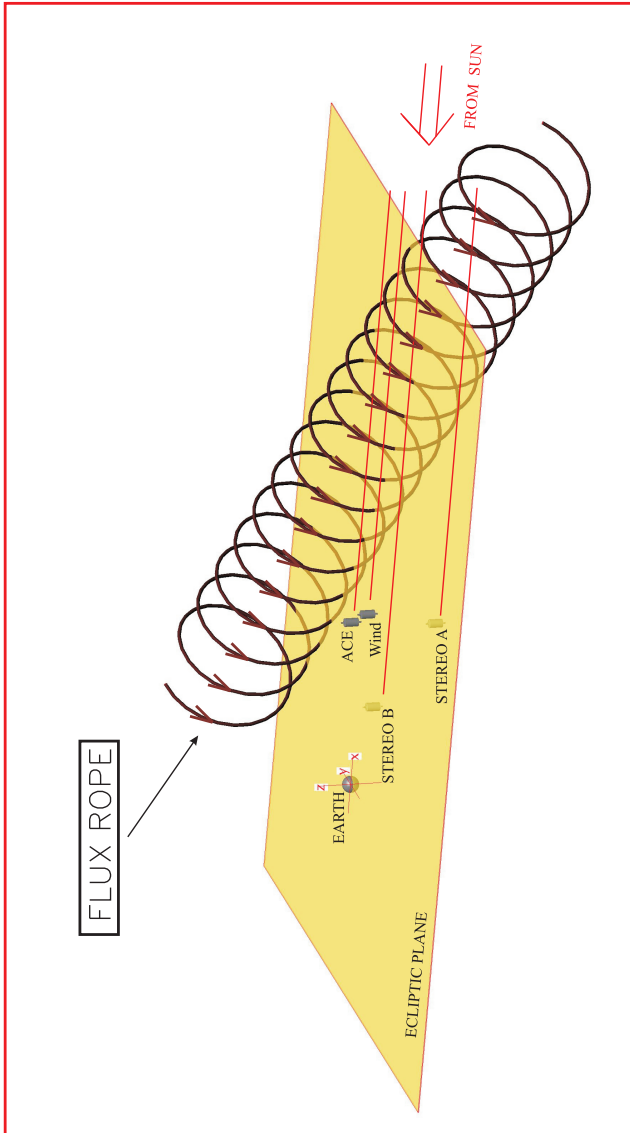
Figure 3.11: Sketch of the flux rope being crossed by the five spacecraft. ACE and WIND are above the ecliptic plane (the yellow plane), but STEREO A and B are located below. CLUSTER 4 (C4) is not drawn, because it is too close to the Earth [*Ruan et al*, 2009].
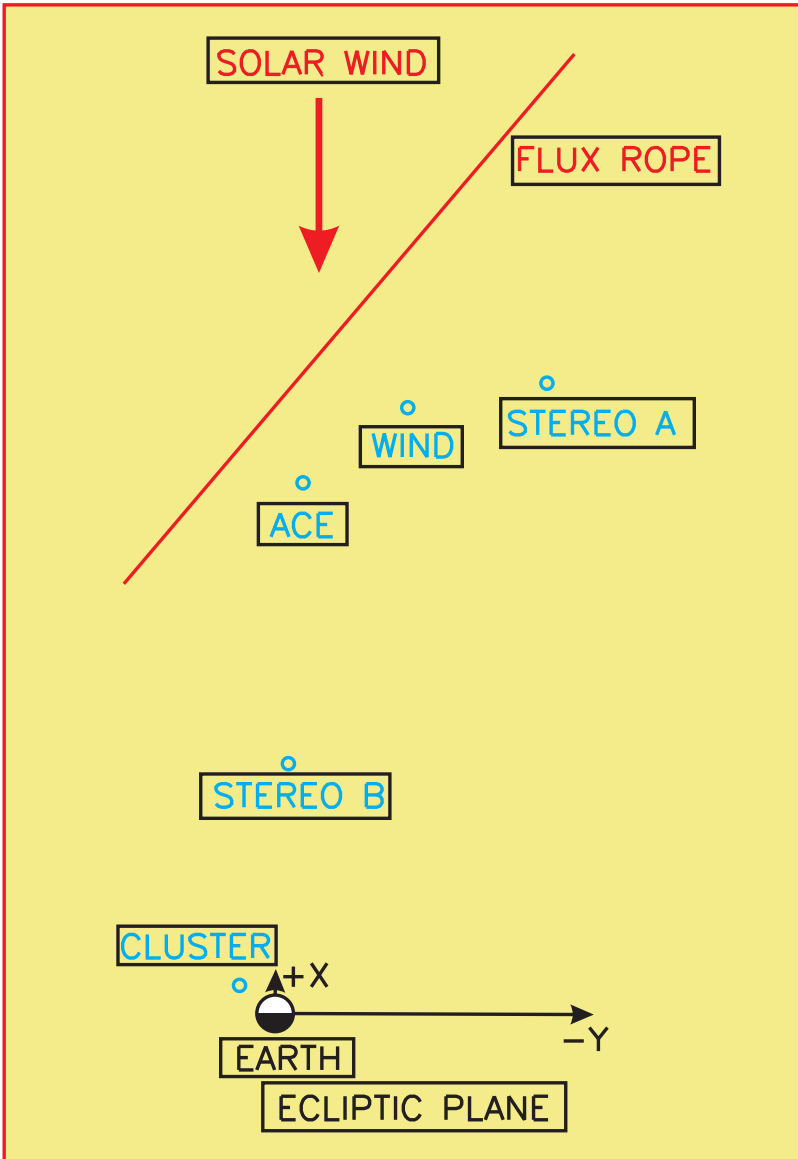
Figure 3.12: Projection of the flux rope in the ecliptic plane. The distances between all the spacecraft and the Earth are drawn to scale.
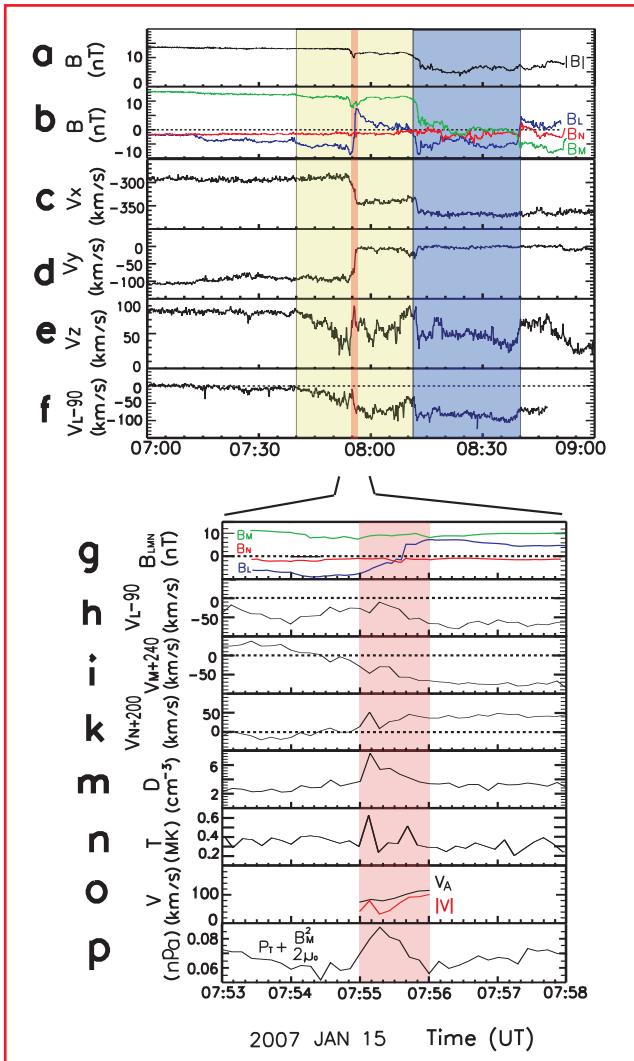
Figure 3.13: The figure displays detailed field and plasma observations from CLUSTER 4 (C4). The yellow highlighted region is the flux rope, and the red highlighted region signals the flux rope core that reveals itself by the B_L reversal [*Ruan et al*, 2009].

We also applied the MVA to the HCS, and found the normal direction of the current sheet plane is (0.44, 0.81, 0.38) in GSE from CLUSTER. This normal direction is roughly parallel to the **N** direction of the flux rope, and roughly perpendicular to the **M** direction, which is the flux rope orientation. (Other spacecraft give similar results.) In other words, the flux rope orientation is roughly parallel to the HCS plane.

Figure 3.14 is a schematic picture of the flux rope crossed by CLUSTER (C4), and is intended to show that the flux rope might be generated by magnetic reconnection. In this figure, solid lines are above the **LN** plane, dotted lines are below. The horizontal green line indicates the CLUSTER trajectory through the flux rope. The red line indicates the hot flow coming from the reconnection site, while the two blue lines are the cooled down flows.

Figure 3.15 shows the global environment of this flux rope from ACE observations. From the top to the bottom, the parameters in these six panels are the magnitude of the solar wind velocity, the proton temperature, the proton number density, the magnitude of the magnetic field, the polar angle Θ_B and the azimuth angle Φ_B of the magnetic field in GSE coordinates. The time period for these observations is two and a half days from 00:00UT 14 on January 2007 to 12:00UT on 16 January 2007. The spacecraft caught signatures of a magnetic cloud, which is shown in the red highlighted region in the figure. Inside the magnetic cloud, there is an enhancement of the magnetic field magnitude, and the angle Θ_B rotates from $\sim 80°$ to $\sim 0°$, and the angle Φ_B changes from $\sim 150°$ to $\sim 330°$. Following the magnetic cloud, a Corotating Interaction Region (CIR) is observed and indicated by the blue highlighted region in the figure. The solar wind velocity is ~ 370 km/s before the CIR and reaches ~ 600 km/s after the CIR. The plasma temperature and density increased in the CIR. The HCS, indicated by the reversal of the angle Φ_B, is embedded in the CIR. The red arrow and the red solid line through all the panels mark the flux rope, which is observed immediately before the HCS. Since this figure shows observations of more than two days, we cannot see the detailed signature of the flux rope, whose time period is only about half an hour. Though it is very difficult to determine the exact boundary between the magnetic cloud and the CIR, the flux rope appears to be embedded in the CIR.

3.4.2 Discussion of the magnetic field and particle signatures, and the generation mechanisms of the flux rope

The five separated spacecraft observed a similar bipolar signature of the magnetic field, indicating a special magnetic structure in the solar wind. To the best of our knowledge, there are several possible interpretations for the bipolar signature. One is a random fluctuation of the magnetic field. Since five spacecraft caught a similar bipolar signature, and the three directions $\mathbf{L}_{FR}$, $\mathbf{M}_{FR}$, and $\mathbf{N}_{FR}$ derived by a local MVA from individual spacecraft observation did not change in space and time, a random fluctuation of the magnetic field is very unlikely to be the reason for this observation. Another interpretation of the bipolar signature could be the crossing of a local current sheet or rotational discontinuity [*Lepping and Wu*, 2005]. Panel **e** of Figure 3.13 shows that there is an enhancement by more than 20% of the total pressure in the core of this magnetic structure. This excess pressure should be balanced by the inward curvature force of the magnetic field. The observed pressure enhancement is not expected at the crossing of a solar wind current sheet
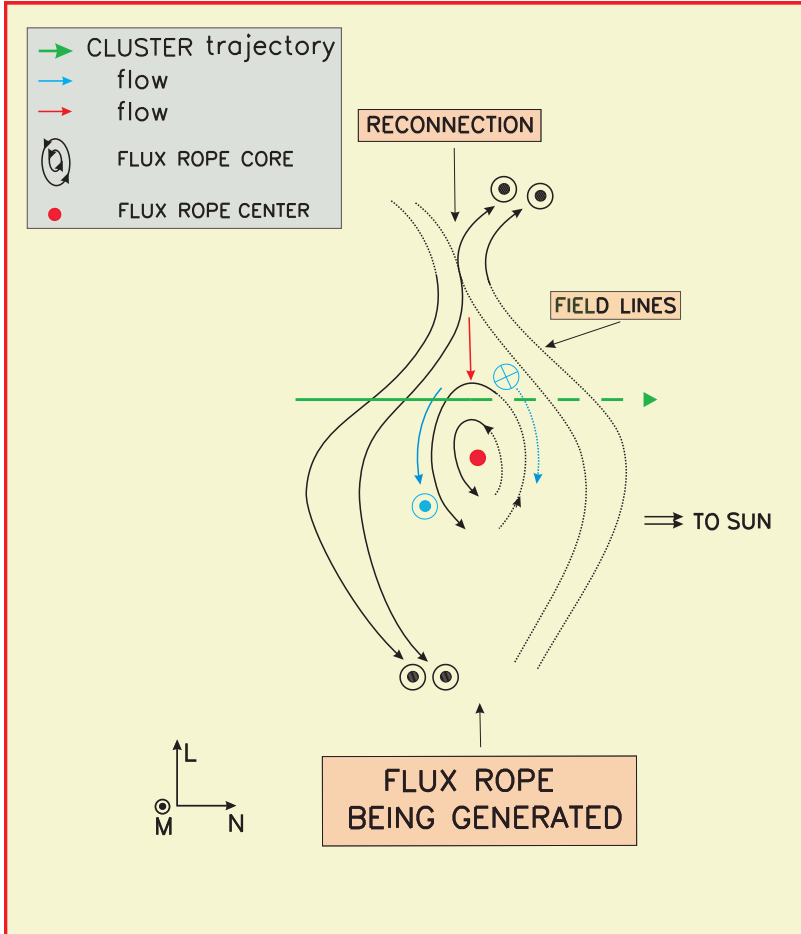
Figure 3.14: Artist plotting of magnetic reconnection generating the flux rope.
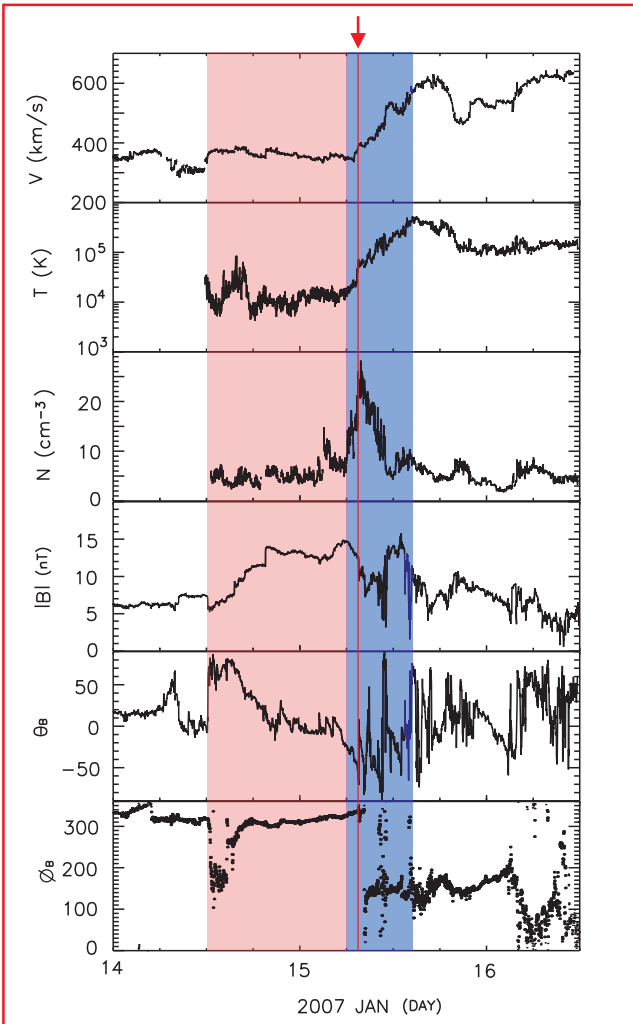
Figure 3.15: Global environment of the flux rope in the solar wind. The red highlighted region indicates the magnetic cloud observed before the flux rope. The blue highlighted region shows the CIR. The red arrow and the red line running through all the panels mark the flux rope [*Ruan et al*, 2009].

or rotational discontinuity, because the magnetic field of the current sheet or rotational discontinuity is not supposed to provide a significant curvature force. The remaining third interpretation of the bipolar signature is the crossing of a flux rope, which could well provide the necessary inward curvature force [*Tu et al.*, 1997]. Since the observed magnetic-field signature and the pressure enhancement are consistent with the crossing of a flux rope, we conclude that this interpretation is the most likely one. The electron signature from STEREO, which will be discussed below, gives further evidence confirming the flux rope. As the orientation of the flux rope did not change in space and time within the range of our observation, this evidence leads us to conclude that the flux rope is a coherent structure [*Hughes and Sibeck*, 1987; *Moldwin and Hughes*, 1991].

Strahl electron observations helped us in specifying the magnetic field topology. There are several possibilities for the loss of the strahl electrons in the solar wind. The first one is the magnetic isolation of the structure core from the surrounding environment. If the flux rope is generated by multiple-X-line reconnection locally in the solar wind, the rope core could be disconnected from the Sun and isolated from the ambient solar wind. The second possibility is the local scattering due to Coulomb collisions. Since the ratio of the mean free path to the structure size is around 10^4, the local scattering due to Coulomb collisions within the structure core cannot be responsible for the electron signature of this event. Another possibility is the scattering due to wave particle interaction. In this case, the wave should be trapped inside the structure core and highly guided along the magnetic field, because there is no loss of strahl electrons outside of the core. This means again that the structure core should be magnetically isolated from the surrounding environment. From the possibilities listed above, we reach the conclusion that the structure core is magnetically isolated from the surrounding environment. The abrupt disappearance of the strahl electrons rules out the possibility of a local current sheet and rotational discontinuity.

Slavin et al. [2003] has studied flux ropes in the Earth magnetotail. They compared the observations with the result of a force-free model, and the comparison shows these flux ropes are in the force-free state in the magnetotail. Due to the limitation of the maximum scale of the Earth magnetotail, both length and the diameter of the flux ropes in the magnetotail are much smaller than the flux rope observed in the solar wind. However, magnetic field signature inside these two types of flux ropes can be still compared. In the work of *Slavin et al.* [2003], the B_z component (corresponding to our B_L component) shows a bipolar signature in Figure 2a and Figure 2b of their paper. Panel **b** of our Figure 3.13 also shows that the B_L component also reveals a clear bipolar signature. In *Slavin et al.* [2003], the B_x component (corresponding to our B_N component) shows an increase in the rope center (Figure 2b of their paper) or remains small and almost constant (Figure 3 of their paper). The B_N component of our observations also remains small and almost constant. The main difference between our observations and their work is in the B_M component. Panels **a** and **b** of Figure 3.13 show that the B_M component decreases a little in the rope core, but the B_y component (corresponding to our B_M component) of *Slavin et al.* [2003] always increases in the rope core (Figure 3 of their paper). A possible reason might be that the flux rope has not been compressed enough to generate the core field. However, though the B_M component decreases a little in the rope core, the total pressure increases by more than 20% in the rope core (Panel **e** of Figure 3.13). The decrease of the magnetic pressure is totally compensated by an increased thermal pressure in the core.

This enhancement of the total pressure should be balanced by the inward curvature force of the magnetic field in the flux rope.

Another notion is that the increase of the B_M component and the magnitude of magnetic field might not be general. The existence of the decreasing field strength at the flux rope core could be suggestive of an O-type neutral configuration opposed to one that has a pre-existing guide field [*Karimabadi et al.,* 1999].

Models suggest that the flux rope should extend in space (see Figure 12a in *Slavin et al.* [2003]). Based on the data from five spacecraft, our observations demonstrate that the flux rope is a quasi two-dimensional magnetic structure, extending over at least 180 R_E in space. The variation of the flux rope orientation in space is another important issue. With the observations from ACE and CLUSTER, *Eastwood et al.* [2008] found that the orientation of a flux rope changes in space, which may be caused by the nearby bow shock. For our event, all the data are taken in the solar wind. According to the MVA for this flux rope, we did not find a systematic bending of the flux rope axis (M_{FR} direction) along the 180-R_E extension in space. This means that the flux rope orientation can stay constant in the solar wind, a conclusion that cannot be obtained with single-spacecraft observations.

Two possible mechanisms have been proposed to explain the presence of a flux rope in the solar wind. One is that local magnetic reconnection in the solar wind can generate these small-scale flux ropes [*Moldwin et al.,* 2000]. The other one is that the flux ropes are convected from the Sun and related to coronal mass ejections (CMEs), which are similar to magnetic clouds [*Feng et al.,* 2007]. From Figure 3.15 we can see that this flux rope and the magnetic cloud are two types of structures with different scales. The diameter of the flux rope is around 40 R_E. If we map this structure to the solar corona, the size of this flux rope will become ~1000 km, which is twenty times smaller than a typical supergranule. It seems to us very unlikely that such a small-scale structure was generated in the solar corona. If the flux rope was really generated in the corona, it might be not easy for this flux rope to survive from the corona to 1 AU in the CIR, which is a highly compressive and dynamic region. Though we cannot totally eliminate the possibility that this small-scale flux rope originated in the solar corona, we suggest it is more likely that the flux rope was generated locally by magnetic reconnection in the solar wind.

The particle data from the CLUSTER 4 (C4) gives possible evidence that this flux rope might be generated by local magnetic reconnection. (Plasma density, temperature, and velocity data only from C4 are available for this event.) Since the identification of magnetic reconnection in the solar wind is far from being trivial, [*Gosling et al.,* 2005] and [*Phan et al.,* 2006] identified magnetic reconnection in the solar wind by the following signatures in the exhaust region: the decrease of the magnitude of the magnetic field, the reversal of the magnetic field direction, the outflow velocity close to the local Alfvén velocity, the increase of the plasma density, and the increase of the plasma temperature. All these five signatures can also be found in this event. Panels **a** and **b** show that the magnitude of the magnetic field decreases in the flux rope core marked by the reversal of the B_L component. Panel **o** shows that the outflow velocity in the flux rope core is close to the local Alfvén velocity. From panels **m** and **n**, we can find an increase of plasma density and temperature in the rope core. We do not dare to say these observations are unambiguous evidence for magnetic reconnection, however, all the CLUSTER data are consistent with the signatures of reconnection in the solar wind. We also should keep

in mind that some reconnection events in the solar wind show only accelerated flows in the exhaust region, but do not exhibit the decrease of the magnetic field strength or the increase of the plasma density and temperature [*Gosling et al.*, 2005]. If this flux rope is really due to the local reconnection in the solar wind, we suggest that the HCS might be an appropriate environment for the reconnection. *Gosling et al.* [2006A, 2006B] have found that the magnetic reconnection in the HCS can generate closed field lines on the sunward side of the reconnection site and disconnected field lines on the anti-sunward side of the reconnection site. The topology of the multiple-X-line magnetic reconnection generating the flux rope has been shown in Figure 3.7.

To sum up, an extended flux rope in the solar wind was observed and studied on the basis of observations from five spacecraft. The analysis shows this flux rope is a quasi two-dimensional magnetic structure, and the orientation of its invariant axis does not change in space and time. These results can be obtained only with multiple-spacecraft observations. The size of the flux rope is about 90 times smaller than that of the magnetic cloud, which passed the spacecraft immediately before the rope. This indicates that the flux rope and the magnetic cloud are two types of structures with different scales, and their sources may be also different.

4 Conclusions

In this thesis, we applied the magnetohydrostatic (MHS) model of *Neukirch,* [1995] (N95) for the modeling of the solar corona during the solar minimum. Not only the magnetic field obtained by extrapolation but also the plasma in the corona was constructed from this model.

There are two boundary conditions for this model. The inner boundary condition is the observed photospheric magnetogram, which provides the line-of-sight component of the magnetic field at the solar surface. By fitting the model results to these observations, we can determine the uncertain coefficients in the model. The outer boundary is given by an artificial source surface to comply with the deformation of streamers in coronagraph observations. The magnetic field is set to be purely radial when crossing this source surface. In the model, the electric current density can be decomposed into two components: the first component is parallel to the magnetic field lines, and the second component flows in spherical shells. The first component of the current density does not generate a Lorentz force, but the second component generates finite Lorentz forces, which are balanced by the pressure gradient and the gravity force.

We compared the magnetic field distribution of the MHS model with potential and linear force-free field models for the same boundary conditions. The comparison reveals that the field lines in the polar cap are similar, because the magnetic field in the polar cap at solar activity minimum should be close to potential. However, in the low-latitude part in the corona, different models generate different results of the magnetic field distribution. The current sheets on the source surface from different models are all very smooth and located close to the equatorial plane for the solar minimum. But the thickness of the sheet differs between the different models. The current sheet from the MHS model is thinner than from the other two models. This should be due to the second component of the current density, which flows in spherical shells. This component changes the magnetic field distribution on the source surface, makes it different from the one in the linear force-free model, and reduces the scale of the current sheet. We found that field-aligned current density can also reduce the scale of the current sheet on the source surface.

The perturbation of the plasma density can be calculated from the magnetic field distribution in the MHS model. The perturbation of the plasma density can be positive or negative, but the perturbation of the plasma pressure is always negative due to the way N95 model is constructed. We put a background plasma in the corona to compensate the perturbation part, and the actual plasma density and pressure in the model is the sum of the perturbation and background parts. The plasma density on the source surface is higher in the equatorial plane than in the polar region, which is a reasonable result in accord with the real situation.

The insufficiencies of this MHS model can not be totally ignored. We also applied

the model to the observations during the solar activity maximum. The result is not as successful as in the solar minimum. The inner boundary condition of the model is the synoptic photospheric magnetogram. This means that we assume that there are no intense changes in the photospheric field during one rotation of the sun. But active regions may evolve significantly over one solar rotation. Another reason is that the solar corona shows a lot more small-scale structures during solar maximum, which are difficult to model with a global linear solution.

Because the strongest density perturbation appears in the active regions in the low corona, we have to apply a very high background density to compensate for the perturbation in the low corona ($r < 1.2R_\odot$). Though it does not mean the magnetic field distribution in the low corona is wrong, it will give us an unreasonably high density distribution in the low corona.

To summarize, though there are some insufficiencies in this MHS model, the distribution of not only the magnetic field but also the plasma in the solar corona can be constructed from this MHS model in a self-consistent way. In the future, we might improve the MHS model result by the relaxation method, as discussed in *Wiegelmann et al,* 2007b. This relaxation method has been applied to analyze a test case from N95, and gives reasonable results of the magnetic field and plasma. The application of this method to the corona with the real observational data as input is demanded in the future. The current sheet on the source surface will be brought into the heliospheric space by the solar wind and forms the heliospheric current sheet (HCS), which can be analyzed by means of in situ observations. By varying the free parameters in the MHS model, the shape and the location of the current sheet on the source surface could be changed. By comparing the model results for the current sheet on the source surface in the solar corona with the in situ observations of the HCS in the solar wind, the extension of the HCS from the corona to the solar wind might be well studied.

In the thesis, we also studied an extended magnetic flux rope in the solar wind with multiple spacecraft observations. Compared with the available studies on flux ropes in the magnetosphere, more observations of flux ropes in the solar wind are still needed to clarify their basic characteristics, such as their lengths, diameters, and possible generation mechanisms. Multiple spacecraft observations are in particular demanded to study the scale of the flux ropes in the solar wind. We presented observations of a flux rope made on 15 January 2007 in the solar wind from five spacecraft: ACE, WIND, STEREO A, STEREO B, and CLUSTER. A typical signature of the flux rope, the bipolar variation of the magnetic field, was observed from all these spacecraft. These observations suggest that the flux rope is a two-dimensional magnetic structure and enable us to determine the extension of the flux rope, which is 180 R_E between STEREO A and STEREO B.

The method of minimum variance analysis (MVA) has been widely used to analyze magnetic structures in space. It appears that the MVA mostly can give a good result in determining the normal direction of a current sheet plane. However, in determining the flux rope orientation, the results from MVA could be very misleading in many cases [*Xiao et al,* 2004]. Usually, results obtained only from the MVA cannot provide the exact orientation of a flux rope. In our event, besides the analysis with the MVA, we also presented a timing analysis based on the joint observations by all five spacecraft. With these two types of methods, the flux rope orientation was unambiguously determined.

From the observations of STEREO A, we found a sharp drop out of the strahl electrons

in the flux rope core. There are several possibilities for such loss of the strahl electrons in the solar wind. The first possible reason is local scattering due to Coulomb collisions. Since the ratio of the mean free path to the structure size is very large, the local scattering due to Coulomb collisions within the structure core cannot be responsible for the electron signature of this event. The second possibility is the magnetic isolation of the structure core from the surrounding environment. The third possibility is the scattering due to wave particle interaction. In this case, the wave should be trapped inside the structure core and highly guided along the magnetic field, because there is no loss of strahl electrons outside of the core. This means again that the structure core should be magnetically isolated from the surrounding environment. From the analysis of the possibilities listed above, we reach the conclusion that the flux rope core is isolated from the ambient solar wind. If the flux rope is generated by multiple-X-line reconnection locally in the solar wind, the rope core could be disconnected from the Sun and isolated from the ambient solar wind [*Moldwin and Hughes*, 1991].

The flux rope is embedded in a Corotating Interaction Region (CIR), which followed a magnetic cloud. The diameter of the flux rope is about 90 times smaller than that of the magnetic cloud, which indicates the flux rope and magnetic cloud are two different types of magnetic structures and their sources might be also different. The possible reconnection signatures inside the flux rope suggest that the flux rope could have been generated locally by magnetic reconnection in the solar wind instead of being convected from the solar corona.

In the future, a statistical study on the particle signatures inside the flux ropes may reveal more intrinsic characteristics of the flux ropes, and the differences between small-scale flux ropes and magnetic clouds in the solar wind.

A Mathematical details of the linear force-free model

Here we derive Eq. 2.5. We put the derivatives of $\mathbf{r}$ first. They will be used for the latter derivations.

$$\nabla \mathbf{r} = \bar{\bar{\mathbf{1}}}, \tag{A.1}$$

$$\nabla \cdot \mathbf{r} = 3, \tag{A.2}$$

$$\nabla \times \mathbf{r} = 0. \tag{A.3}$$

Now we go to

$$
\begin{aligned}
\mathbf{P}(\psi) &= \nabla \times \mathbf{T}(\tau) \\
&= \nabla \times \nabla \times (\mathbf{r}\tau) \\
&= \nabla[\nabla \cdot (\mathbf{r}\tau)] - \Delta(\mathbf{r}\tau) \\
&= \nabla[\nabla \cdot (\mathbf{r}\tau)] - \nabla \cdot \nabla(\mathbf{r}\tau) \\
&= \nabla[\nabla \cdot (\mathbf{r}\tau)] - \nabla \cdot [(\nabla\mathbf{r})\tau] - \nabla \cdot [(\nabla\tau)\mathbf{r}] \\
&= \nabla[\nabla \cdot (\mathbf{r}\tau)] - \nabla\tau - \nabla\tau \cdot (\nabla\mathbf{r}) - \mathbf{r}\Delta\tau \\
&= \nabla[\nabla \cdot (\mathbf{r}\tau)] - 2\nabla\tau - \mathbf{r}\Delta\tau \\
&= \nabla[\nabla \cdot (\mathbf{r}\tau) - 2\tau] - \mathbf{r}\Delta\tau \\
&= \nabla[\mathbf{r} \cdot (\nabla\tau) + (\nabla \cdot \mathbf{r})\tau - 2\tau] - \mathbf{r}\Delta\tau \\
&= \nabla[\mathbf{r} \cdot (\nabla\tau) + \tau] - \mathbf{r}\Delta\tau \\
&= \nabla[r\frac{\partial}{\partial r}\tau + \tau] - \mathbf{r}\Delta\tau \\
&= \nabla[\frac{\partial}{\partial r}(r\tau)] - \mathbf{r}\Delta\tau. \tag{A.4}
\end{aligned}
$$

B Mathematical details of the Magnetohydrostatic(MHS) model

In this part of the thesis, we present mathematical details of the MHS model. These details are lengthy but necessary for the readers to understand the model.

First we put here partial derivatives of the unit vectors in the spherical coordinate system, which will be used in the latter derivations without additional explanations.

$$\frac{\partial \mathbf{e_r}}{\partial r} = 0,$$

$$\frac{\partial \mathbf{e_r}}{\partial \theta} = \mathbf{e}_\theta,$$

$$\frac{\partial \mathbf{e_r}}{\partial \phi} = \mathbf{e}_\phi \sin\theta,$$

$$\frac{\partial \mathbf{e}_\theta}{\partial r} = 0,$$

$$\frac{\partial \mathbf{e}_\theta}{\partial \theta} = -\mathbf{e_r},$$

$$\frac{\partial \mathbf{e}_\theta}{\partial \phi} = \mathbf{e}_\phi \cos\theta,$$

$$\frac{\partial \mathbf{e}_\phi}{\partial r} = 0,$$

$$\frac{\partial \mathbf{e}_\phi}{\partial \theta} = 0,$$

$$\frac{\partial \mathbf{e}_\phi}{\partial \phi} = -\mathbf{e_r} \sin\theta - \mathbf{e}_\theta \cos\theta.$$

Next we write the explicit expression of the operator $\mathbf{L}$ in the spherical coordinate system,

$$
\begin{aligned}
\mathbf{L} &= \frac{1}{i}(\mathbf{r} \times \nabla) \\
&= \frac{1}{i}\left(\mathbf{r} \times \mathbf{e_r}\frac{\partial}{\partial r} + \mathbf{r} \times \mathbf{e}_\theta \frac{1}{r}\frac{\partial}{\partial \theta} + \mathbf{r} \times \mathbf{e}_\phi \frac{1}{r\sin\theta}\frac{\partial}{\partial \phi}\right) \\
&= \frac{1}{i}\left(\mathbf{e}_\phi \frac{\partial}{\partial \theta} - \frac{\mathbf{e}_\theta}{\sin\theta}\frac{\partial}{\partial \phi}\right).
\end{aligned}
\tag{B.1}
$$

We write the explicit expression of $\mathbf{L}^2$ as:

$$\mathbf{L}^2 = \mathbf{L} \cdot \mathbf{L}$$

$$
\begin{aligned}
&= -(\mathbf{r} \times \nabla) \cdot (\mathbf{r} \times \nabla) \\
&= -\left(\mathbf{e}_\phi \frac{\partial}{\partial \theta} - \frac{\mathbf{e}_\theta}{\sin\theta} \frac{\partial}{\partial\phi}\right) \cdot \left(\mathbf{e}_\phi \frac{\partial}{\partial\theta} - \frac{\mathbf{e}_\theta}{\sin\theta} \frac{\partial}{\partial\phi}\right) \\
&= -\left(\frac{\partial^2}{\partial\theta^2} + \frac{\cos\theta}{\sin\theta}\frac{\partial}{\partial\theta} + \frac{1}{\sin^2\theta}\frac{\partial^2}{\partial\phi^2}\right).
\end{aligned}
\tag{B.2}
$$

The partial derivatives of the unit vectors have been used for the last step.

==

We derive Eq. 2.39 from Eqs. 2.36 and 2.38. We have

$$
\nabla \times \mathbf{B} = \mu_0 \mathbf{j}, \tag{B.3}
$$
$$
\mu_0 \mathbf{j} = \alpha\mathbf{B} + \varepsilon(r)[\nabla(\mathbf{r} \cdot \mathbf{B})] \times \mathbf{r}. \tag{B.4}
$$

Inserting Eq. B.4 into B.3, taking the curl of Eq. B.3 and dotting it with $\mathbf{r}$, we get

$$
\mathbf{r} \cdot \nabla \times (\nabla \times \mathbf{B}) = -\mathbf{r} \cdot \Delta\mathbf{B} = -\Delta(\mathbf{r} \cdot \mathbf{B}), \tag{B.5}
$$
$$
\mathbf{r} \cdot \nabla \times (\alpha\mathbf{B}) = \alpha\mathbf{r} \cdot \nabla \times \mathbf{B} = \alpha\mathbf{r} \cdot [\alpha\mathbf{B} + \varepsilon(r)\nabla(\mathbf{r} \cdot \mathbf{B}) \times \mathbf{r}] = \alpha^2 \mathbf{r} \cdot \mathbf{B}. \tag{B.6}
$$

The condition that the vector $\varepsilon(r)\nabla(\mathbf{r} \cdot \mathbf{B}) \times \mathbf{r}$ is perpendicular to $\mathbf{r}$ has been used for Eq. B.6.

$$
\begin{aligned}
\mathbf{r} \cdot \nabla \times [\varepsilon(r)\nabla(\mathbf{r} \cdot \mathbf{B}) \times \mathbf{r}] &= \mathbf{r} \cdot [\nabla\varepsilon(r) \times (\nabla(\mathbf{r} \cdot \mathbf{B}) \times \mathbf{r}) + \varepsilon(r)\nabla \times (\nabla(\mathbf{r} \cdot \mathbf{B}) \times \mathbf{r})] \\
&= \varepsilon(r)\mathbf{r} \cdot \nabla \times [\nabla(\mathbf{r} \cdot \mathbf{B}) \times \mathbf{r}] \\
&= -\varepsilon(r)\mathbf{r} \cdot \nabla \times [\mathbf{r} \times \nabla(\mathbf{r} \cdot \mathbf{B})] \\
&= \varepsilon(r)\mathbf{r} \times \nabla \cdot [\mathbf{r} \times \nabla(\mathbf{r} \cdot \mathbf{B})] \\
&= \varepsilon(r)\mathbf{L}^2(\mathbf{r} \cdot \mathbf{B}).
\end{aligned}
\tag{B.7}
$$

Now we reach

$$
\Delta(\mathbf{r} \cdot \mathbf{B}) + \varepsilon(r)\mathbf{L}^2(\mathbf{r} \cdot \mathbf{B}) + \alpha^2\mathbf{r} \cdot \mathbf{B}. \tag{B.8}
$$

==

Next we derive Eq. 2.41.

$$
\begin{aligned}
\mathbf{L} \cdot \mathbf{B} &= \frac{1}{i}\mathbf{r} \times \nabla \cdot \mathbf{B} \\
&= \frac{1}{i}\mathbf{r} \cdot (\nabla \times \mathbf{B}) \\
&= \frac{1}{i}\mathbf{r} \cdot (\alpha\mathbf{B}) \\
&= \frac{\alpha}{i}\mathbf{r} \cdot \mathbf{B}.
\end{aligned}
\tag{B.9}
$$

The condition that the second component of the current density is perpendicular to $\mathbf{r}$ has been used.

==

Next we derive Eq. 2.43. We have

$$\mathbf{r} \cdot \mathbf{B} = \sum_{l=1}^{\infty} \sum_{m=-l}^{l} l(l+1) \left(\sum_{j=1}^{2} A_{lm}^{(j)} u_l^{(j)}(r) \right) Y_l^m(\theta, \phi). \tag{B.10}$$

For the simplicity, we ignore all the footnotes, headnotes and the sum signs, so we write this equation as

$$\mathbf{r} \cdot \mathbf{B} = AUY. \tag{B.11}$$

We should keep in mind that A is only a coefficient, U is only the function of r, and Y is only the function of θ and ϕ. We will insert this expression to Eq. B.8.

From Eq. B.2, we can write straightforward that

$$\Delta = \frac{1}{r} \frac{\partial^2}{\partial r^2}(r) - \frac{\mathbf{L}^2}{r^2}. \tag{B.12}$$

So

$$
\begin{aligned}
\Delta(\mathbf{r} \cdot \mathbf{B}) &= \Delta[AUY] \\
&= \frac{1}{r} \frac{\partial^2}{\partial r^2}(rAUY) - \frac{\mathbf{L}^2}{r^2}(AUY) \\
&= \frac{1}{r} \frac{\partial^2}{\partial r^2}(rAUY) - \frac{l(l+1)}{r^2}(AUY),
\end{aligned} \tag{B.13}
$$

$$\varepsilon(r)\mathbf{L}^2(AUY) = \varepsilon(r)l(l+1)AUY. \tag{B.14}$$

The property that $\mathbf{L}^2 Y = l(l+1)Y$ has been used, which can be found in chapter 16 of [*Jackson,* 1975].

So Eq. B.8 will reach

$$\frac{\partial^2}{\partial r^2}(rAUY) - \frac{l(l+1)}{r}AUY + \varepsilon(r)rl(l+1)AUY + \alpha^2 rAUY = 0. \tag{B.15}$$

Since $g(r) = rU$ as defined and if we drop out AY for all the terms, we reach

$$\frac{\partial^2}{\partial r^2}[g(r)] - \frac{l(l+1)}{r^2}g(r) + \varepsilon(r)l(l+1)g(r) + \alpha^2 g(r) = 0. \tag{B.16}$$

This is Eq. 2.43.

===

If we can notice $\mathbf{L}u(r) = 0$ and $\mathbf{L} \cdot \nabla Y = (-i)\mathbf{r} \times \nabla \cdot (\nabla Y) = (-i)\mathbf{r} \cdot \nabla \times (\nabla Y) = 0$, Eq. 2.45 will be satisfied by inserting Eq. 2.46 into it. The left question is how to specify $w_{lm}(r)$. This question can be solved with the help of $\nabla \cdot \mathbf{B} = 0$. From Eqs. 2.42 and 2.46, we can write

$$\mathbf{B} = \frac{l(l+1)}{r}AUY\mathbf{e_r} + v\mathbf{L}Y + w\nabla Y. \tag{B.17}$$

Since

$$
\begin{aligned}
\mathbf{L}Y & = \frac{1}{i}\left(\mathbf{e}_\phi\frac{\partial}{\partial\theta} - \frac{\mathbf{e}_\theta}{\sin\theta}\frac{\partial}{\partial\theta}\right)Y \\
& = \frac{1}{i}\left(\mathbf{e}_\phi\frac{\partial}{\partial\theta}Y - \frac{\mathbf{e}_\theta}{\sin\theta}\frac{\partial}{\partial\theta}Y\right),
\end{aligned}
\tag{B.18}
$$

$$
\nabla Y = \frac{1}{r}\frac{\partial Y}{\partial\theta}\mathbf{e}_\theta + \frac{1}{r\sin\theta}\frac{\partial Y}{\partial\phi}\mathbf{e}_\phi,
\tag{B.19}
$$

Eq. B.17 reaches

$$
\mathbf{B} = \frac{l(l+1)}{r}AUY\mathbf{e_r} + \left(\frac{w}{r}\frac{\partial Y}{\partial\theta} - \frac{v}{i\sin\theta}\frac{\partial Y}{\partial\phi}\right)\mathbf{e}_\theta + \left(\frac{w}{r\sin\theta}\frac{\partial Y}{\partial\phi} + \frac{v}{i}\frac{\partial Y}{\partial\theta}\right)\mathbf{e}_\phi.
\tag{B.20}
$$

So $\nabla\cdot\mathbf{B} = 0$ gives

$$
\frac{1}{r^2}\frac{\partial[rl(l+1)AUY]}{\partial r} + \frac{1}{r\sin\theta}\frac{\partial[\frac{\sin\theta w}{r}\frac{\partial Y}{\partial\theta} - \frac{v}{i}\frac{\partial Y}{\partial\phi}]}{\partial\theta} + \frac{1}{r\sin\theta}\frac{\partial[\frac{w}{r\sin\theta}\frac{\partial Y}{\partial\phi} + \frac{v}{i}\frac{\partial Y}{\partial\theta}]}{\partial\phi} = 0.
\tag{B.21}
$$

By finishing all these differentiations and with the help of $\mathbf{L}^2 Y = l(l+1)Y$, we can reach

$$
\frac{\partial[rl(l+1)AUY]}{\partial r} - l(l+1)Yw = 0.
\tag{B.22}
$$

So we obtain

$$
w = \frac{\partial(rAU)}{\partial r}.
\tag{B.23}
$$

This is Eq. 2.48.

We derive Eq. 2.61 now.

$$
\frac{dp_0}{d\Phi} = \frac{dp_0}{dr}\Big/\frac{d\Phi}{dr} = \frac{dp_0}{dr}\frac{r^2}{GM},
\tag{B.24}
$$

$$
\begin{aligned}
\frac{d[\frac{F^2}{2k(\Phi)}]}{d\Phi} & = -\frac{F^2}{2k^2(\Phi)}\frac{dk(\Phi)}{d\Phi} \\
& = \frac{1}{2}\left(\frac{GM}{r^3}\right)^2(\mathbf{r}\cdot\mathbf{B})^2\frac{dk(\Phi)}{dr}\frac{r^2}{GM} \\
& = -\frac{(\mathbf{r}\cdot\mathbf{B})^2}{2}\left(\frac{d\varepsilon(r)}{dr} + \varepsilon(r)\frac{6}{r}\right)\frac{r^2}{GM}.
\end{aligned}
\tag{B.25}
$$

The condition $k(\Phi) = \varepsilon(r)\left(\frac{GM}{r^3}\right)^{-2}$ has been used in the last step of the derivation.

$$
\begin{aligned}
\mathbf{B}\cdot\nabla F & = \mathbf{B}\cdot[\frac{\varepsilon(r)r(\mathbf{r}\cdot\mathbf{B})}{|\nabla\Phi|}] \\
& = \frac{\varepsilon(r)r}{|\nabla\Phi|}\mathbf{B}\cdot\nabla(\mathbf{r}\cdot\mathbf{B}) + \mathbf{B}\cdot\nabla[\frac{\varepsilon(r)r}{|\nabla\Phi|}](\mathbf{r}\cdot\mathbf{B}) \\
& = \frac{r^2}{GM}r\varepsilon(r)\mathbf{B}\cdot\nabla(\mathbf{r}\cdot\mathbf{B}) + \frac{3r\varepsilon(r)}{GM}(\mathbf{r}\cdot\mathbf{B})(\mathbf{r}\cdot\mathbf{B}) \\
& + \frac{r^2}{GM}\frac{d\varepsilon(r)}{dr}(\mathbf{r}\cdot\mathbf{B})(\mathbf{r}\cdot\mathbf{B}).
\end{aligned}
\tag{B.26}
$$

The condition $|\nabla\Phi| = GM/r^2$ has been used.

By combining Eqs. B.24, B.25, B.26 2.58 and 2.60, Eq. 2.61 can be reached.

C   Mathematical details of the Minimum Variance Analysis (MVA)

We write the explicit expression of σ^2 first.

$$
\begin{aligned}
\sigma^2 &= \frac{1}{M}\sum_{m=1}^{M} |\,(\mathbf{B}^{(m)} - \langle\mathbf{B}\rangle)\cdot\hat{n}\,|^2 \\
&= \frac{1}{M}\sum_{m=1}^{M} |\,[(B_1^{(m)}, B_2^{(m)}, B_3^{(m)}) - (\langle B_1\rangle, \langle B_2\rangle, \langle B_3\rangle)]\cdot(n_X, n_Y, n_Z)\,|^2 \\
&= \frac{1}{M}\sum_{m=1}^{M}\left(B_1^{(m)}n_X + B_2^{(m)}n_Y + B_3^{(m)}n_Z - \langle B_1\rangle n_X - \langle B_2\rangle n_Y - \langle B_3\rangle n_Z\right)^2 \qquad \text{(C.1)} \\
&= \frac{1}{M}\sum_{m=1}^{M}
\end{aligned}
$$

$$
\begin{aligned}
&[B_1^{(m)}B_1^{(m)}n_Xn_X + B_1^{(m)}B_2^{(m)}n_Xn_Y + B_1^{(m)}B_3^{(m)}n_Xn_Z \\
&-B_1^{(m)}\langle B_1\rangle n_Xn_X - B_1^{(m)}\langle B_2\rangle n_Xn_Y - B_1^{(m)}\langle B_3\rangle n_Xn_Z \\
&+B_1^{(m)}B_2^{(m)}n_Xn_Y + B_2^{(m)}B_2^{(m)}n_Yn_Y + B_2^{(m)}B_3^{(m)}n_Yn_Z \\
&-B_2^{(m)}\langle B_1\rangle n_Xn_Y - B_2^{(m)}\langle B_2\rangle n_Yn_Y - B_2^{(m)}\langle B_3\rangle n_Yn_Z \\
&+B_1^{(m)}B_3^{(m)}n_Xn_Z + B_2^{(m)}B_3^{(m)}n_Yn_Z + B_3^{(m)}B_3^{(m)}n_Zn_Z \\
&-B_3^{(m)}\langle B_1\rangle n_Xn_Z - B_3^{(m)}\langle B_2\rangle n_Yn_Z - B_3^{(m)}\langle B_3\rangle n_Zn_Z \\
&-B_1^{(m)}\langle B_1\rangle n_Xn_X - B_2^{(m)}\langle B_1\rangle n_Xn_Y + B_3^{(m)}\langle B_1\rangle n_Xn_Z \\
&+\langle B_1\rangle\langle B_1\rangle n_Xn_X + \langle B_1\rangle\langle B_2\rangle n_Xn_Y + \langle B_1\rangle\langle B_3\rangle n_Xn_Z \\
&-B_1^{(m)}\langle B_2\rangle n_Xn_Y - B_2^{(m)}\langle B_2\rangle n_Yn_Y + B_3^{(m)}\langle B_2\rangle n_Yn_Z \\
&+\langle B_1\rangle\langle B_2\rangle n_Xn_Y + \langle B_2\rangle\langle B_2\rangle n_Yn_Y + \langle B_2\rangle\langle B_3\rangle n_Yn_Z \\
&-B_1^{(m)}\langle B_3\rangle n_Xn_Z - B_2^{(m)}\langle B_3\rangle n_Yn_Z + B_3^{(m)}\langle B_3\rangle n_Zn_Z \\
&+\langle B_1\rangle\langle B_3\rangle n_Xn_Z + \langle B_2\rangle\langle B_3\rangle n_Yn_Z + \langle B_3\rangle\langle B_3\rangle n_Zn_Z] \\
={}&\langle B_1B_1\rangle n_Xn_X + \langle B_1B_2\rangle n_Xn_Y + \langle B_1B_3\rangle n_Xn_Z \\
&-\langle B_1\rangle\langle B_1\rangle n_Xn_X - \langle B_1\rangle\langle B_2\rangle n_Xn_Y - \langle B_1\rangle\langle B_3\rangle n_Xn_Z \\
&\langle B_1B_1\rangle n_Xn_X + \langle B_2B_2\rangle n_Yn_Y + \langle B_2B_3\rangle n_Yn_Z \\
&-\langle B_1\rangle\langle B_2\rangle n_Xn_Y - \langle B_2\rangle\langle B_2\rangle n_Yn_Y - \langle B_2\rangle\langle B_3\rangle n_Yn_Z \\
&\langle B_1B_3\rangle n_Xn_Z + \langle B_2B_3\rangle n_Yn_Z + \langle B_3B_3\rangle n_Zn_Z
\end{aligned}
$$

$$-\langle B_1\rangle\langle B_3\rangle n_X n_Z - \langle B_2\rangle\langle B_3\rangle n_Y n_Z - \langle B_3\rangle\langle B_3\rangle n_Z n_Z$$
$$-\langle B_1\rangle\langle B_1\rangle n_X n_X - \langle B_1\rangle\langle B_2\rangle n_X n_Y - \langle B_1\rangle\langle B_3\rangle n_X n_Z$$
$$+\langle B_1\rangle\langle B_1\rangle n_X n_X + \langle B_1\rangle\langle B_2\rangle n_X n_Y + \langle B_1\rangle\langle B_3\rangle n_X n_Z$$
$$-\langle B_1\rangle\langle B_2\rangle n_X n_Y - \langle B_2\rangle\langle B_2\rangle n_Y n_Y - \langle B_2\rangle\langle B_3\rangle n_Y n_Z$$
$$+\langle B_1\rangle\langle B_2\rangle n_X n_Y + \langle B_2\rangle\langle B_2\rangle n_Y n_Y + \langle B_2\rangle\langle B_3\rangle n_Y n_Z$$
$$-\langle B_1\rangle\langle B_3\rangle n_X n_Z - \langle B_2\rangle\langle B_3\rangle n_Y n_Z - \langle B_3\rangle\langle B_3\rangle n_Z n_Z$$
$$+\langle B_1\rangle\langle B_3\rangle n_X n_Z + \langle B_2\rangle\langle B_3\rangle n_Y n_Z + \langle B_3\rangle\langle B_3\rangle n_Z n_Z. \tag{C.2}$$

If we expand Eq. 3.12 in a explicit expression, it is same as above.

As to the calculation of $\partial\sigma^2/\partial n_X$, $\partial\sigma^2/\partial n_Y$ and $\partial\sigma^2/\partial n_Z$, all of them can be calculated based on Eq. B.1.

We also have

$$\frac{\partial(\lambda n_X^2)}{\partial n_X} = 2\lambda n_X, \tag{C.3}$$

$$\frac{\partial(\lambda n_Y^2)}{\partial n_Y} = 2\lambda n_Y, \tag{C.4}$$

$$\frac{\partial(\lambda n_Z^2)}{\partial n_Z} = 2\lambda n_Z. \tag{C.5}$$

With all of these differentiations mentioned above, Eqs. 3.7, 3.8 and 3.9 will result in Eq. 3.10.

Bibliography

Aly, J. J, 1989, On the reconstruction of the nonlinear force-free coronal magnetic field from boundary data, Solar Physics, 120, 19.

Aly, J. J. and Amari, T., 1997, Current sheets in two-dimensional potential magnetic fields. III. Formation in complex topology configurations and application to coronal heating, Astronomy and Astrophysics, 319, 699

Amari, T., Aly, J. J., Luciani, J. F., Boulmezaoud, T. Z., Mikic, Z., 1997, Reconstructing the Solar Coronal Magnetic Field as a Force-Free Magnetic Field, 174, 129.

Amari, T., Boulmezaoud, T. Z., Aly, J. J., 2006, Well posed reconstruction of the solar coronal magnetic field, Astronomy and Astrophysics, 446, 691.

Antiochos, S. K., DeVore, C. R., Klimchuk, J. A., 1999, A Model for Solar Coronal Mass Ejections, Astrophysical Journal, 510, 485.

Aschwanden, 2005, Physics of the solar corona–An introduction with problems and solutions, Praxis Publishing, Chichester, UK

Aschwanden, M. J., 2005, 2D feature recognition and 3D reconstruction in solar EUV images, Astrophysical Journal, 228, 339.

Aschwanden, M. J., Nightingale, R. W., Alexander, D., 2000, Evidence for Nonuniform Heating of Coronal Loops Inferred from Multithread Modeling of TRACE Data, Astrophysical Journal, 541, 1059.

Aulanier, G., Demoulin, P., 1998, 3-D magnetic configurations supporting prominences. I. The natural presence of lateral feet, Astronomy and Astrophysics, 329, 1125.

Aulanier, G. et al., 2000, 3-D Magnetic Configurations for Filaments and Flares: The Role of "Magnetic Dips" and "Bald Patches" Advances in Space Research, 26, 485.

Behannon, K. W., Neubauer, F. M., Barnstorf, H., 1981, Fine-scale characteristics of interplanetary sector boundaries, Journal of Geophysical Research, 86, 3273-3287.

Berger, M. A., 1991, Generation of coronal magnetic fields by random surface motions. I-Mean square twist and current density, Astronomy and Astrophysics, 252, 369

Berger, M. A., 1993, Energy-crossing number relations for braided magnetic fields, Physical Review Letters, 70, 705

Bird, M. K., Edenhofer, P., 1990, Remote sensing observations of the solar corona, Physics of the inner heliosphere, 13

Bogdan, T. J., Low, B. C., 1986, The three-dimensional structure of magnetostatic atmospheres. II - Modeling the large-scale corona, Astrophysical Journal, 306, 271

Carcedo, L., Brown, D. S., Hood, A. W., Neukirch, T., Wiegelmann, T. , 2003, A Quantitative Method to Optimise Magnetic Field Line Fitting of Observed Coronal Loops, Solar Physics, 218, 29.

Chiu, Y. T., Hilton, H. H. , 1977, Exact Green's function method of solar force-free magnetic-field computations with constant alpha. I - Theory and basic test cases, Astrophysical Journal, 212, 873.

Cowley, S. W. H. ,1984, in Magnetic Reconnection in Space and Laboratory Plasma, Geophysics Monograph, 30, 375-378, (ed. Hones, E. W.), American Geophysical Union, Washington DC.

Crooker, N. U. et al., 2003, Suprathermal electron isotropy in high-beta solar wind and its role in heat flux dropouts, Geophysical Research Letters, 30, NO. 12, 1619.

Crooker, N. U. and Pagel, C., 2008, Residual strahls in solar wind electron dropouts: Signatures of magnetic connection to the Sun, disconnection, or interchange reconnection?, Journal of Geophysical Research, 113, A02106.

Cuperman, S., Detman, T. R., Bruma, C., Dryer, M. , 1992, Towards a consistent treatment of thermally conductive magnetohydrodynamic flows in helmet-streamer coronal structures, Astronomy and Astrophysics, 265, 785.

De Moortel, I., Hood, A. W., Ireland, J., Arber, T. D., 1999, Phase mixing of Alfvén waves in a stratified and open atmosphere, Astronomy and Astrophysics, 346, 641

De Moortel, I., Hood, A. W., Arber, T. D., 2000, Phase mixing of Alfvén waves in a stratified and radially diverging, open atmosphere, Astronomy and Astrophysics, 354, 334

Eastwood, J. P. et al., 2005, Observations of multiple X-line structure in the Earth's magnetotail current sheet: A Cluster case study, Geophysical Research Letters, 32, L11105.

Eastwood, J. P. et al., 2008, Evidence for collisionless magnetic reconnection at Mars, Geophysical Research Letters, 35, L02106.

von Edlén, B., Die deutung der emissionsliniem im spektrum der sonnenkorona, Z. Astrophysik, 22, 30

Elphic, R. C., 1995, Observations of flux transfer events: A review, in Physics of the Magnetopause, Geophysics Monograph., 90, 225-233, American Geophysical Union, Washington DC.

Feng, L., Wiegelmann, T., Inhester, B., Solanki, S., Gan, W. Q., Ruan, P., 2007, Magnetic Stereoscopy of Coronal Loops in NOAA 8891, Solar Physics, 241, 235.

Feng, H. Q., Wu, D. J., Chao, J. K., 2007, Size and energy distributions of interplanetary magnetic flux ropes, Journal of Geophysical Research, 112, A02102.

Fontenla, J. M., Avrett, E. H., Loeser, R., 2002, Energy balance in the solar transition region. I-Hydrostatic thermal models with ambipolar diffusion, Astrophysical Journal, 355, 700

Gabriel, A. H., 1976, A magnetic model of the solar transition region, Royal Society, Philosophical Transactions, Series A, 281, 339-352

Galsgaard, K. Nordlund, Å., 1997, Heating and activity of the solar corona. 3. Dynamics of a low beta plasma with three-dimensional null points, Journal of Geophysical Research, 102, 231

Galsgaard, K. Nordlund, Å., 1996, Heating and activity of the solar corona 1. Boundary shearing of an initially homogeneous magnetic field, Journal of Geophysical Research, 101, 13445

Gary, G. A., 2001, Plasma Beta above a Solar Active Region: Rethinking the Paradigm, Solar Physics, 203, 71

Gibson, S. E., Bagenal, F., 1995, Large-scale magnetic field and density distribution in the solar minimum corona, Journal of Geophysical Research, 100, 19,865.

Gibson, S. E., Bagenal, F., Low, B. C., 1996, Current sheets in the solar minimum corona, Journal of Geophysical Research, 101, 4813.

Goossens, M., Hollweg, J. V., Sakurai, T., 1992, Resonant behaviour of MHD waves on magnetic flux tubes. III - Effect of equilibrium flow, Solar Physics, 138, 233

Goossens, M., Ruderman, M. S., Hollweg, J. V., 1995, Dissipative MHD solutions for resonant Alfven waves in 1-dimensional magnetic flux tubes, Solar Physics, 157, 75

Gosling, J. T, 1995, A new class of forward-reverse shock pairs in the solar wind, Geophysical Research Letters, 21, 2271

Gosling, J. T., Skoug, R. M., McComas, D. J., Smith, C. W, 2005A, Direct evidence for magnetic reconnection in the solar wind near 1 AU, Journal of Geophysical Research, 110, A01107.

Gosling, J. T., McComas, D. J., Skoug, R. M., Smith, C. W., 2005B, Magentic disconnection from the Sun: Observations of a reconnection exhaust in the solar wind at the heliospheric current sheet, Geophysical Research Letters, 32, L05105.

Gosling, J. T., McComas, D. J., Skoug, R. M., Smith, C. W., 2006, Magnetic reconnection at the heliospheric current sheet and the formation of closed magnetic field lines in the solar wind, Geophysical Research Letters, 33, L17102.

Gosling, J. T., Eriksson, S., Phan, T. D., Larson, D. E., Skoug, R. M., McComas, D. J., 2007A, Direct evidence for prolonged magnetic reconnection at a continuous x-line within the heliospheric current sheet, Geophysical Research Letters, 34, L06102.

Gosling, J. T. et al. 2007B, Five spacecraft observations of oppositely directed exhaust jets from a magnetic reconnection X-line extending $> 4.26 \times 10^6$ km in the solar wind at 1 AU, Geophysical Research Letters, 34, L20108.

Heyvaerts, J.; Priest, E. R., 1983, Coronal heating by phase-mixed shear Alfven waves, Astronomy and Astrophysics, 117, 220

Heyvaerts, J., Priest, E. R., 1992, A self-consistent turbulent model for solar coronal heating, Astrophysical Journal, 390, 297

Hoeksema, J. Todd, 1991, Large-scale solar and heliospheric magnetic fields, Solar Physics , 11, 15.

Hollweg, J. V., 1985, Energy and momentum transport by waves in the solar atmosphere, Advances in space plasma physics, 77

Hollweg, J. V., 1991, Alfvénically-Driven Slow Shocks in the Solar Chromosphere and Corona, Bulletin of the American Astronomical Society, 23, 1037

Hughes, W. J. and Sibeck, D. G., 1987, On the three dimensional structure of plasmoids, Geophysical Research Letters, 14, 636-639.

Inhester, B., Wiegelmann, T., 2006, Nonlinear Force-Free Magnetic Field Extrapolations: Comparison of the Grad Rubin and Wheatland Sturrock Roumeliotis Algorithm, Solar Physics , 235, 201.

Ionson, J. A., 1978, Resonant absorption of Alfvénic surface waves and the heating of solar coronal loops, Astrophysical Journal, 226, 650

Kano, Ryouhei, Tsuneta, Saku, 1995, Scaling Law of Solar Coronal Loops Obtained with YOHKOH, Astrophysical Journal, 454, 934.

Krivova, N. A., Solanki, S. K., 2004, Effect of spatial resolution on estimating the Sun's magnetic flux, Astronomy and Astrophysics, 417, 1125.

Kuperus, M., Ionson, J. A., Spicer, D. S., 1981, On the theory of coronal heating mechanisms, Annual Review of Astronomy and Astrophysics, 19, 7

Lagg, A., 2005, in Chromospheric and Corona Magnetic Fields, ESA,SP-596.

Low, B. C., 1990, Equilibrium and dynamics of coronal magnetic fields, Annu. Rew. Astron. Astrophys. 28, 491-524.

Low, B. C., 1993A, Three-dimensional structures of magnetostatic atmospheres. V - Coupled electric current systems, Astrophysical Journal, 408, 689

Low, B. C., 1993B, Three-dimensional structures of magnetostatic atmospheres. VI - Examples of coupled electric current systems, Astrophysical Journal, 408, 693

Low, B. C., 1992, Three-dimensional structures of magnetostatic atmospheres. IV - Magnetic structures over a solar active region, Astrophysical Journal, 399, 300

Low, B. C., 1991, Three-dimensional structures of magnetostatic atmospheres. III - A general formulation, Astrophysical Journal, 370, 427

Low, B. C., 1985,Three-dimensional structures of magnetostatic atmospheres. I - Theory, Astrophysical Journal, 293, 31

Luhmann et al., 2008, STEREO IMPACT investigation goals, measurements, and data products overview, Space Science Review 136, 117-184.

Marsch, E., Wiegelmann, T., Xia, L. D., 2004, Coronal plasma flows and magnetic fields in solar active regions. Combined observations from SOHO and NSO/Kitt Peak, Astronomy and Astrophysics, 428, 629.

Metcalf, T. R. et al., 2008,Nonlinear Force-Free Modeling of Coronal Magnetic Fields. II. Modeling a Filament Arcade and Simulated Chromospheric and Photospheric Vector Fields Solar Physics, 247, 269.

Meyer-Vernet, N., 2007, Basics of the solar wind, Atmospheric and space series

Milano, L. J., Gomez, D. O., Martens, P. C. H., 1997, Solar Coronal Heating: AC versus DC, Astrophysical Journal, 490, 442

Milano, L. J., Dmitruk, P., Mandrini, C. H., Gómez, D. O., Démoulin, P., 1997, Quasi-Separatrix Layers in a Reduced Magnetohydrodynamic Model of a Coronal Loop, Astrophysical Journal, 521, 889

Moldwin, M. B. and Hughes, W. J., 1991, Plasmoids as flux ropes, Journal of Geophysical Research, 96, 14,051.

Moldwin, M. B., Ford, S., Lepping, R., Slavin, J., Szabo, A., 2000, Small-scale magnetic flux ropes in the solar wind, Geophysical Research Letters, 27, 57-60.

Neukirch, T., 1995, On self-consistent three-dimensional analytic solutions of the magnetohydrostatic equations, Astronomy and Astrophysics, 301, 628.

Neukirch, T., 1997, Nonlinear self-consistent three-dimensional arcade-like solutions of the magnetohydrostatic equations, Astronomy and Astrophysics, 325, 847.

Neukirch, T. and Rastätter, L., 1999, A new method for calculating a special class of self-consistent three-dimensional magnetohydrostatic equilibria, Astronomy and Astrophysics, 348, 1000.

Paker, E. N., 1983, Magnetic Neutral Sheets in Evolving Fields - Part Two - Formation of the Solar Corona, Astrophysical Journal, 264, 642

Paker, E. N., 1988, Nanoflares and the solar X-ray corona, Astrophysical Journal, 330, 474

Petrie, G. J. D., Neukirch, T., 2000, The Green's function method for a special class of linear three-dimensional magnetohydrostatic equilibria, Astronomy and Astrophysics, 356, 735.

Phan, T. D. et al., 2006, A magnetic reconnection X-line extending more than 390 Earth radii in the solar wind, Nature 439, 175-178

Pneuman, G. W., Kopp, Roger A., 1971, Gas-Magnetic Field Interactions in the Solar Corona, Solar Physics, 18, 258.

Pizzo, V., 1978, A three-dimensional model of corotating streams in the solar wind. I - Theoretical foundations, Journal of Geophysical Research, 83, 5563

Riley, Pete et al., 2006, A Comparison between Global Solar Magnetohydrodynamic and Potential Field Source Surface Model Results, Astrophysical Journal, 653, 1510.

Rosner, R., Tucker, W. H., Vaiana, G. S., 1978, Dynamics of the quiescent solar corona, Astrophysical Journal, 220, 643.

Ruan, P., Wiegelmann, T., Inhester, B., Neukirch, T., Solanki, S. K., Feng, L., 2008, A first step in reconstructing the solar corona self-consistently with a magnetohydrostatic model during solar activity minimum, Astronomy and Astrophysics, 481, 827

Ruan, P. et al., 2009, Multiple-spacecraft Study of an Extended Magnetic Structure in the Solar Wind, Journal of Geophysical Research, accepted.

Rudenko, G. V., 2001, Extrapolation of the solar magnetic field within the potential-field approximation from full-disk magnetograms, Solar Physics, 198, 5.

Ruderman, M. S., Goossens, M., Ballester, J. L., Oliver, R., 1997, Resonant Alfven waves in coronal arcades driven by footpoint motions, Astronomy and Astrophysics, 328, 361

Russell, C. T. et al., 2006, The solar wind interaction with Venus through the eyes of the Pioneer Venus Orbiter, Planetary and Space Science 54, 1482-1495.

Russell C. T. and Walker, R. J. (1985), Flux transfer event at Mercury, Journal of Geophysical Research, 90, 11,067-11,074.

Sakurai, Takashi, 1989, Computational modeling of magnetic fields in solar active regions, Space Science Reviews, 51, 11.

Schmidt, H. U., 1964, in the physics of solar flares, 107

Schrijver, C. J.; Sandman, A. W.; Aschwanden, M. J.; DeRosa, M. L., 2004, The Coronal Heating Mechanism as Identified by Full-Sun Visualizations, Astrophysical Journal, 615, 512

Schrijver, C. J., 2001, The coronae of the sun and solar-type stars, the 11th cool stars, stellar systems and the sun, ASP conference series, 223, 131

Schrijver, Carolus J., DeRosa, Marc L., Title, Alan M., Metcalf, Thomas R., 2005, The Nonpotentiality of Active-Region Coronae and the Dynamics of the Photospheric Magnetic Field, Astrophysical Journal, 628, 501.

Schrijver, Carolus J., et al., 2006, Nonlinear Force-Free Modeling of Coronal Magnetic Fields Part I: A Quantitative Comparison of Methods, Solar Physics, 235, 161.

Schwenn, R., 1997, First View of the Extended Green-Line Emission Corona At Solar Activity Minimum Using the Lasco-C1 Coronagraph on SOHO, Solar Physics, 175, 667.

Schwenn, R., 1996, Mass ejections from the Sun and their interplanetary counterparts, AIP Conf. Proc., 382, 426

Seehafer, N., 1978, Determination of constant alpha force-free solar magnetic fields from magnetograph data, Solar Physics, 58, 215.

Serio, S., Peres, G., Vaiana, G. S., Golub, L., Rosner, R., 1981, Closed coronal structures. II - Generalized hydrostatic model, Astrophysical Journal, 243, 288.

Schodhan, S., 2000, Plasma properties of driver gas following interplanetary shocks observed by ISEE-3, Solar Wind Five, NASA conference Proceedings 2280, 711

Slavin, J. A. et al., 2003, Geotail observations of magnetic flux ropes in the plasma sheet, Journal of Geophysical Research, 108, 1015.

Sonnerup, B. U. O and Scheible, M., 1998, Minimum and maximum variance analysis, Analysis methods for multi-spacecraft data, 185-205, ISSI/ESA, G. Paschmann and P. W. Daly (Eds.), Switzerland.

Solanki, S. K., Lagg, A., Woch, J., Krupp, N., Collados, M., 2003, Three-dimensional magnetic field topology in a region of solar coronal heating, Nature, 425, 692.

Sturrock, P. A., Uchida, Y., 1981, Coronal heating by stochastic magnetic pumping, Astrophysical Journal, 246, 331

Tu, C.-Y., Marsch, E., Ivory, K., Schwenn, R., 1997, Pressure enhancement associated with meridinal flow in high-speed solar wind: possible evidence for an interplanetary magnetic flux rope, Ann. Geophysicae 108, 137-142.

Van Ballegooijen, A. A., 1986, Cascade of magnetic energy as a mechanism of coronal heating, Astrophysical Journal, 311, 1001

Vignes, D., Acuña, M. H., Connerney, J. E. P., Crider, D. H., Réme, H., Mazelle, C., 2004, Magnetic flux ropes in the Martian atmosphere: global characteristics, Space Science Review, 111, 223-231.

Walker, R. J. and Russell, C. T., 1985, Flux transfer event at the Jovian magnetopause, Journal of Geophysical Research, 90, 7397-7404.

Wheatland, M. S., Sturrock, P. A., Roumeliotis, G., 2000, An Optimization Approach to Reconstructing Force-free Fields, Astrophysical Journal, 540, 1150.

White, S. M., 2002, New radio instrumentation for the study of sunspots and starspots, Astronomische Nachrichten, 323, 265.

Wiegelmann, T., Schindler, K., Neukirch, T., 1998, Helmet Streamers with Triple Structures: Weakly Two-Dimensional Stationary States, Solar Physics, 180, 439.

Wiegelmann, T., Schindler, K., Neukirch, T., 2000, Helmet Streamers with Triple Structures: Simulations of resistive dynamics, Solar Physics, 191, 391.

Wiegelmann, T., Neukirch, T., 2002, Including stereoscopic information in the reconstruction of coronal magnetic fields, Solar Physics, 208, 233.

Wiegelmann, T., Neukirch, T., 2003, Magnetic modeling and tomography: First steps towards a consistent reconstruction of the solar corona, Solar Physics, 214, 287.

Wiegelmann, T., 2004, Optimization code with weighting function for the reconstruction of coronal magnetic fields, Solar Physics, 219, 87.

Wiegelmann, T., Inhester, B., Lagg, A., Solanki, S. K., 2005a, How To Use Magnetic Field Information For Coronal Loop Identification, Solar Physics, 228, 67.

Wiegelmann, T., Lagg, A., Solanki, S. K., Inhester, B., Woch, J., 2005b, Comparing magnetic field extrapolations with measurements of magnetic loops, Astronomy and Astrophysics, 433, 701.

Wiegelmann, T., Inhester, B., 2006, Magnetic Stereoscopy, Soar Physics, 236, 25.

Wiegelmann, T. , 2007, Computing Nonlinear Force-Free Coronal Magnetic Fields in Spherical Geometry, Solar Physics, 240, 227.

Wiegelmann, T., Neukirch, T, Ruan, P., Inhester, B., 2007, Optimization approach for the computation of magnetohydrostatic coronal equilibria in spherical geometry, Astronomy & Astrophysics, 475, 701.

Wiegelmann, T. , 2008, Nonlinear force-free modeling of the solar coronal magnetic field, Journal of Geophysical Research, 113, A03S02.

Woo, R., Habbal, S. R., 2000, Connecting the Sun and the solar wind: Source regions of the fast wind observed in interplanetary space, Journal of Geophysical Research, 105, 12667

Wu, S. T., Guo, W. P., Wang, J. F., 1995, Dynamical evolution of a coronal streamer-bubble system. 1: A self-consistent planar magnetohydrodynamic simulation, Solar Physics, 157, 325.

Wu, S. T. et al., 1997, MHD Interpretation of LASCO Observations of a Coronal Mass Ejection as a Disconnected Magnetic Structure, Solar Physics, 175, 719.

Xiao, C. J., Pu, Z. Y., Ma, Z. W., Fu, S. Y., Huang, Z. Y., Zong, Q. G., 2004, Inferring of flux rope orientation with the minimum variance analysis technique, Journal of Geophysical Research, 109, A11, A11218.

Zhao, X. P., Hoeksema, J. T., Scherrer, P. H., 2000, Modeling the 1994 April 14 Polar Crown SXR Arcade Using Three-Dimensional Magnetohydrostatic Equilibrium Solutions, Astrophysical Journal, 538, 932.

Zhao, X. P., Hoeksema, J. T., Scherrer, P. H., 1993, Unique determination of model coronal magnetic fields using photospheric observations, Solar Physics, 143, 41.

Zhao, X. P., Hoeksema, J. T., Scherrer, P. H., 1994, A coronal magnetic field model with horizontal volume and sheet currents, Solar Physics, 151, 91.

Zurbuchen, T. H., Richardson, I. G., 2006, In-situ solar wind and magnetic field signatures of interplanetary coronal mass ejections, Space Sciences Series of ISSI, Corona Mass Ejections, 31

Zwickl, R. D., 1983, Plasma properties of driver gas following interplanetary shocks observed by ISEE-3, Solar Wind Five, NASA Conference Proceedings 2280, 711

Publications

1. **P. Ruan**, T. Wiegelmann, B. Inhester, T. Neukirch, S. K. Solanki, and L. Feng, 2008, A first step in reconstructing the solar corona self-consistently with a magnetohydrostatic model during solar activity minimum, Astronomy and Astrophysics, 481, 827

——

2. **P. Ruan**, A. Korth, E. Marsch, B. Inhester, S. K. Solanki, T. Wiegelmann, Q.-G. Zong, R. Bucik, K-H. Fornacon, (accepted) Multiple-spacecraft Study of an Extended Magnetic Structure in the Solar Wind, Journal of Geophysical Research.

——

3. T. Wiegelmann , T. Neukirch, **P. Ruan**, B. Inhester, (2007) Optimization approach for the computation of magnetohydrostatic coronal equilibria in spherical geometry, DOI: 10.1051/0004-6361:20078244, 475, 701-706, Astronomy and Astrophysics.

——

4. L. Feng, T. Wiegelmann , B. Inhester, S.K. Solanki, W.Q. Gan, **P. Ruan**, (2007) Magnetic Stereoscopy of Coronal loops in NOAA 8891, Vol. 241, 235-249, Solar Physics.

Acknowledgements

After three years in Lindau I finally find a chance to express my thanks to many people, who give me a lot of help.

Dear Bernd and Thomas, I thank you for your continued support. I really learnt a lot from our group meetings. Without the help from you, my research will not succeed definitely.

I like to thank Prof. Sami K. Solanki and Prof. Eckart Marsch for the instructive suggestions on my work.

I very much thank Prof. Stefan Dreizler for accepting me as his student at the University of Göttingen.

I must thank Dr. Dieter Schmitt for a lot of help to my three years' life here.

I thank a lot of friends here for the supporting and sharing. They are Xianyi Li, Jingnan Guo, Li Feng, Zhi Xu, Lotfi Yelles Chaouche, Philippe Kobel, Chun Ming Mark Cheung, Yuichi Ito and his wife, Takeshi Kuroda, Julia Thalmann, Nilda Oklay, Jean-Baptiste Vincent, Raphael Attie, Radoslav Bucik, ...

I thank my parents.

Lebenslauf

Name:	Peng Ruan
Geburtsdatum:	16.10.1980
Geburtsort:	Anqing, Anhui, China
Staatsangehörigkeit:	Chinesisch
Studium:	09/1998 bis 07/2002: China University of Mining and Technology Bachelor in Geophysik
	09/2002 bis 07/2005: Peking University Diplom in Weltraumphysik
Promotion:	01/2006 bis 01/2009: Promotion an der Universität Göttingen Stipendium der International Max Planck Research School on Physical Processes in the Solar System and Beyond